

REPORT DOCUMENTATION PAGE

AFRL-SR-AR-TR-04-

Public reporting burden for this collection of information is estimated to average 1 hour per response, including the time for reviewing instructions, gathering existing data needed, and completing and reviewing this collection of information. Send comments regarding this burden estimate or any other aspect of this burden to Department of Defense, Washington Headquarters Services, Directorate for Information Operations and Reports (0704-0188), 1215 Jefferson Davis Highway, Suite 1204, Arlington, VA 22202-4302. Respondents should be aware that notwithstanding any other provision of law, no person shall be subject to any penalty for failing to comply with a collection of information if it does not have a valid OMB control number. PLEASE DO NOT RETURN YOUR FORM TO THE ABOVE ADDRESS.

0327

| | | | | | |
|---|-------------|-------------------------|-------------------------------|---|---|
| 1. REPORT DATE (DD-MM-YYYY) 04-30-2004 | | 2. REPORT TYPE Final | | 3. DATES COVERED (From - To) 09/01/00-08/31/03 | |
| 4. TITLE AND SUBTITLE Topological Modeling and Stochastic Analysis of Images | | | | 5a. CONTRACT NUMBER | |
| | | | | 5b. GRANT NUMBER F49620-01-1-0204 | |
| | | | | 5c. PROGRAM ELEMENT NUMBER | |
| 6. AUTHOR(S) Hamid Krim | | | | 5d. PROJECT NUMBER | |
| | | | | 5e. TASK NUMBER | |
| | | | | 5f. WORK UNIT NUMBER | |
| 7. PERFORMING ORGANIZATION NAME(S) AND ADDRESS(ES) North Carolina State University, Raleigh, NC 27695 | | | | | |
| 9. SPONSORING / MONITORING AGENCY NAME(S) AND ADDRESS(ES) AFOSR/NM Room 713 4015 Wilson Blvd , Arlington VA 22203-1954 | | | | 10. SPONSOR/MONITOR'S ACRONYM(S) Dr. Jon Sjogren | |
| | | | | 11. SPONSOR/MONITOR'S REPORT NUMBER(S) | |
| 12. DISTRIBUTION / AVAILABILITY STATEMENT Approved for public release, distribution unlimited | | | | | |
| 13. SUPPLEMENTARY NOTES | | | | | |
| 14. ABSTRACT In this report, we include the dissertation thesis the grant has funded together with a list of publications, and invitations the funded research has generated. Concepts in classification and recognition problems. 1. We have explored the potential of combining geometrical as well as topological information in capturing the essence of an object for classification and recognition purposes. The geometrical information within a topologically homogeneous part of an object is captured through a set of level curves, while the topology is extracted from the singular points. 2. Defining probability models on manifolds as would be required by the surface of an object remains a challenging topic. The approach here exploits a triangulated approximation on which a geodesic is defined to capture the nonlinear intrinsic structure of an object surface. 3. Obtaining distribution for objects in turn allows us to compare them by IT measures. associate/describe any approximable surface/object by a distribution which | | | | | |
| 15. SUBJECT TERMS Topology, Probability models, Level curves, geometry | | | | | |
| 16. SECURITY CLASSIFICATION OF: | | | 17. LIMITATION OF ABSTRACT | 18. NUMBER OF PAGES | 19a. NAME OF RESPONSIBLE PERSON |
| a. REPORT | b. ABSTRACT | c. THIS PAGE | | | 19b. TELEPHONE NUMBER (include area code) |

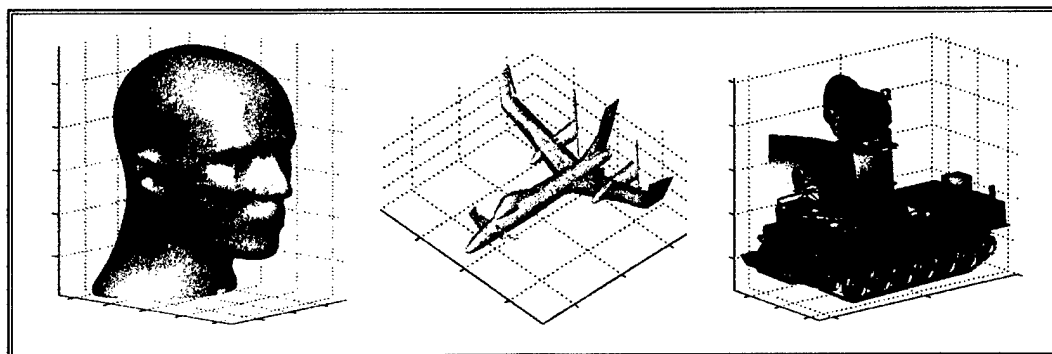
20040706 074

Report to AFOSR
Grant F49620-01-1-0204

Topological Modeling and Stochastic Analysis of Images

*Department of Electrical and Computer Engineering
North Carolina State University, Raleigh, NC 27695*

P.I. : Hamid Krim



Our research effort over the last three years, has primarily focused on exploring of combining topological information with geometrical features to characterize and represent 3-dimensional objects for classification/recognition and efficient storage in data bases. This is specifically carried out (3-D object or graphs of images) by well designed mappings from manifolds onto R and referred to as *height functions*. While the topology may indeed be parsimoniously and well reflected by these mappings, much of the local geometry is missing. These height function mappings are indeed commonly defined as equivalence relations which result in a quotient space of level sets of the surface, and which are eventually graphically represented by the so-called Reeb Graphs. These, as described in more detail later, are indeed but a set of nodes and edges which bifurcate whenever a change of topology takes place. A natural follow up investigation is in attempting, perhaps at a slight additional cost, to further refine such a representation by trying to add on geometrical (more local) information as often required by problems in classification and recognition. Towards that end, and as later described, we introduce a generalized notion of a *height function*, together with a *shading function* as well as a *support function*, respectively reflecting topology, shape and continuity of the surface under analysis. In the process, we propose to modify the existing Reeb graph to a pseudo-weighted graph, as a novel compact representation well adapted to classification and recognition problems. The funding has helped our group in completing a productive and successful three years in publications as well as productive on the publication front [5, 12, 8, 11, 17, 18, 19, 20, 9, 10, 13, 14, 15, 16, 21, 22, 4, 2, 1, 1, 6, 7]. Our work has been recognized at a national and international level and has resulted in several invitations to INRIA (Sophia-Antipolis France), Liapunov Institute (Moscow State University), and a 3-Dimensional Imaging and Computer Vision workshop at University of Padova (Padova, Italy), the Institute of Pure and Applied Mathematics at UCLA. In addition, it has helped us in securing funds from NATO to initiate collaborations between researchers at Moscow State University (Dr. Minlos) and Institute for Information and Transmission Problems in Moscow, and INRIA at Sophia-Antipolis (France). In addition, a significant byproduct of this work has greatly contributed to a concerted effort to fight crime, in a project of Picture ID compression performed as a community outreach effort for the North Carolina Criminal Justice Information Network (NCCJIN). The reduction of a picture ID, thanks to the hierarchical image representation inspired by our graph representations, to about a 800 byte representation would indeed allow NCCJIN to safeguard their multimillion dollar investment in their low capacity radio network and manage to rapidly access data bases across the state and the nation. Test are still under way to transition this work and potentially serve as an example for the police forces across the nation or even the world. This work has been featured in several newspapers and magazines including the Design Engineer, Prism magazine etc.

We include a Ph.D. dissertation as a detailed appendix to much of the work funded by this grant.

References

- [1] Sajjad H. Baloch and Hamid Krim, SEMIPARAMETRIC SKEW-SYMMETRIC MODELING OF PLANAR SHAPES, ICASSP'04, Canada, 2004, .
- [2] Sajjad H. Baloch, Hamid Krim and Marc G. Genton, Semiparametric skew symmetric distributions in shape representation", Skew-Elliptical Distributions and their Applications: A Journey Beyond Normality, M. G. Genton Editor, Chapman & Hall/CRC. In press, 2004.
- [3] Sajjad H. Baloch and Hamid Krim, Classification and Sampling of Shapes through Semiparametric Skew-Symmetric Shape Model, EUSIPCO'04, Austria, 2004, Accepted.
- [4] Sajjad H. Baloch and Hamid Krim, Flexible Skew Symmetrical Shape Model: Learning, Classification and Sampling, IEEE Trans. on Pattern Analysis and Machine Intelligence, Submitted, 2004.
- [5] Yun He, A. Ben Hamza, Hamid Krim "A generalized divergence measure for robust image registration", IEEE Transactions on Signal Processing, vol. 51, no. 5, pp. 1211-1220, May 2003.
- [6] O.V. Poliannikov and H. Krim On Sampling Closed Planar Curves and Surfaces, Journal on Sampling in Signal and Image Processing, 2003.
- [7] Stochastic Differential Equations and Geometric Flows, IEEE Trans. on Image Processing, Dec. 2002.
- [8] A. Ben Hamza, Hamid Krim, G.B. Unal "Unifying probabilistic and variational estimation", IEEE Signal Processing Magazine, pp. 37-47, September 2002.
- [9] A. Ben Hamza, Hamid Krim "Image denoising: a nonLinear robust statistical approach", IEEE Transactions on Signal Processing, vol. 49, no. 12, pp. 3045-3054, December 2001.
- [10] A. Ben Hamza, Hamid Krim "A variational approach to maximum a posteriori estimation for image denoising", Lecture Notes in Computer Science, vol. 2134, pp. 19-34, 2001.
- [11] A. Ben Hamza, Hamid Krim "A topological variational model for image singularities", Proc. IEEE International Conference on Image Processing, Rochester, New York, September 2002.
- [12] B. R. Lee, A. Ben Hamza, Hamid Krim "An active contour model for image segmentation: a variational perspective", Proc. IEEE International Conference on Acoustics Speech and Signal Processing, Orlando, May 2002.

- [13] A. Ben Hamza, Yun He, Hamid Krim "An information divergence measure for ISAR image registration", Proc. IEEE Workshop on Statistical Signal Processing, Singapore, August 2001.
- [14] A. Ben Hamza, Hamid Krim "Nonlinear image filtering: trade-off between optimality and practicality", Proc. IEEE International Conference on Image Processing, Greece, October 2001.
- [15] A. Ben Hamza, Hamid Krim "Nonlinear image filtering in a mixture of Gaussian and heavy-tailed noise", Proc. IEEE Workshop on Statistical Signal Processing, Singapore, 2001.
- [16] A. Ben Hamza, Hamid Krim "Towards a unified view of estimation: variational vs. statistical", Proc. IEEE International Conference on Image Processing, Greece, October 2001. A. Ben Hamza, Yun He, Hamid Krim, Alan Willsky "A multiscale approach to pixel-level image fusion", Journal of Integrated Computer-Aided Engineering, to appear 2004.
- [17] A. Ben Hamza, Hamid Krim "A topological skeleton of illuminated manifolds", Proc. IEEE International Conference on Image Processing, Barcelona, Spain 2003.
- [18] A. Ben Hamza, Hamid Krim "Robust environmental image denoising", ISI International Conference on Environmental Statistics and Health, Santiago de Compostela, Spain, 2003.
- [19] A. Ben Hamza, Hamid Krim "Robust influence functionals for image filtering", Proc. IEEE International Conference on Image Processing, Barcelona, Spain 2003.
- [20] A. Ben Hamza, Hamid Krim "Jensen-Renyi divergence: theoretical and computational perspectives", Proc. IEEE International Symposium on Information Theory, Japan, 2003.
- [21] A. Ben Hamza, Hamid Krim, Josiane Zerubia "A nonlinear entropic variational model for image filtering", EURASIP Journal on Applied Signal Processing, submitted 2003.
- [22] A. Ben Hamza, Yun He, Hamid Krim, Alan Willsky "A multiscale approach to pixel-level image fusion", Journal of Integrated Computer-Aided Engineering, to appear 2004.

**TITLE: Topological Modeling and Stochastic
Analysis of Images**

NAME: H. Krim

Final Report to AFOSR: F49620-01-1-0204

Table of Contents

| | |
|---|-------------|
| List of Tables | viii |
| List of Figures | ix |
| 1 Introduction | 1 |
| 1.1 Framework and motivation | 2 |
| 1.1.1 Image denoising | 2 |
| 1.1.2 Object recognition | 3 |
| 1.1.3 Joint exploitation of geometry and topology | 6 |
| 1.2 Contributions | 8 |
| 1.3 Thesis overview | 9 |
| 1.4 Publications | 11 |
| 2 Background | 13 |
| 2.1 Continuous representation of images | 13 |
| 2.1.1 Differentiability of images | 13 |
| 2.2 Three-dimensional surfaces | 14 |
| 2.2.1 Image graph | 15 |
| 2.2.2 Triangle mesh | 19 |
| 2.2.3 Scalar volume and isosurface | 19 |
| 3 Robust Variational Image Denoising | 23 |
| 3.1 Introduction | 23 |
| 3.2 Problem statement | 24 |
| 3.3 MAP estimation: model-based approach | 25 |
| 3.4 A variational approach to MAP estimation | 26 |
| 3.4.1 Properties of the optimization problem | 29 |
| 3.4.2 Numerical solution: gradient descent flows | 30 |
| 3.4.3 Illustrative cases | 32 |
| 3.5 Robust variational approach | 35 |

| | | |
|----------|--|-----------|
| 3.5.1 | Robustness for unknown statistics | 35 |
| 3.5.2 | Perona-Malik equation: an estimation-theoretic perspective | 38 |
| 3.6 | Information based functionals | 39 |
| 3.6.1 | Information theoretic approach | 39 |
| 3.6.2 | Entropic gradient descent flow | 40 |
| 3.6.3 | Improved entropic gradient descent flow | 42 |
| 3.7 | Experimental results | 44 |
| 3.8 | Discussions and conclusions | 47 |
| 4 | Topological Variational Model for Image Singularities | 48 |
| 4.1 | Introduction | 48 |
| 4.2 | Problem formulation | 50 |
| 4.2.1 | Geometric analysis of images | 50 |
| 4.2.2 | Image singularities | 51 |
| 4.2.3 | Image singularities: a geometric approach | 51 |
| 4.3 | Topological analysis of images | 53 |
| 4.3.1 | Image singularities: a topological perspective | 54 |
| 4.3.2 | Almost all images are Morse functions | 56 |
| 4.3.3 | Topological equivalence of images | 58 |
| 4.4 | Image singularity-based flow | 58 |
| 4.5 | Numerical simulations | 58 |
| 4.6 | Conclusions | 60 |
| 5 | Topological Modeling of Illuminated Surfaces | 61 |
| 5.1 | Introduction | 61 |
| 5.2 | Reeb graph representation | 62 |
| 5.2.1 | Morse theory and singularities | 62 |
| 5.2.2 | Height function | 63 |
| 5.2.3 | Reeb graph | 63 |
| 5.3 | Shading problem and height function | 65 |
| 5.3.1 | Shading function | 65 |
| 5.3.2 | Height function in the direction of light | 68 |
| 5.3.3 | Singularities of the shading function | 69 |
| 5.4 | Experimental results | 71 |
| 5.5 | Conclusions | 71 |
| 6 | Geodesic Matching of 3D Objects | 74 |
| 6.1 | Introduction | 74 |
| 6.2 | Problem formulation | 76 |
| 6.2.1 | Global shape measure | 77 |
| 6.2.2 | Construction of a measure space | 79 |
| 6.3 | Related work | 79 |
| 6.3.1 | Reeb graph | 79 |

| | | |
|----------|---|------------|
| 6.3.2 | Shape distribution | 81 |
| 6.4 | Proposed methodology | 82 |
| 6.4.1 | Global geodesic shape function | 82 |
| 6.4.2 | Global geodesic shape distribution | 85 |
| 6.4.3 | Properties of geodesic shape signature | 86 |
| 6.5 | Probabilistic dissimilarity | 88 |
| 6.6 | Information-geometric approach to geodesic shape distributions | 91 |
| 6.6.1 | Statistical manifolds | 91 |
| 6.6.2 | Geodesic shape manifold | 92 |
| 6.7 | Experimental results | 93 |
| 6.8 | Conclusions | 99 |
| 7 | Distance Function-based Object Recognition | 100 |
| 7.1 | Introduction | 100 |
| 7.2 | Topology identification | 101 |
| 7.2.1 | Singular points | 103 |
| 7.2.2 | Morse function | 103 |
| 7.2.3 | Sard's theorem | 105 |
| 7.2.4 | Height function | 105 |
| 7.2.5 | Generalized height function | 107 |
| 7.2.6 | Height function and immersion | 109 |
| 7.3 | Topology coding | 109 |
| 7.3.1 | Reeb graph | 109 |
| 7.4 | Level sets around Morse points | 111 |
| 7.4.1 | Handle decompositions | 113 |
| 7.5 | Distance function | 114 |
| 7.6 | Connection between height function and distance function | 117 |
| 8 | Conclusions and Future Research | 120 |
| 8.1 | Contributions of the thesis | 120 |
| 8.1.1 | Robust and efficient variational filters for image denoising | 120 |
| 8.1.2 | A topological variational model for image singularities | 121 |
| 8.1.3 | Topological modeling of illuminated surfaces using Reeb graph | 121 |
| 8.1.4 | Geodesic object representation and recognition | 121 |
| 8.1.5 | Distance function-based object recognition | 122 |
| 8.2 | Future research directions | 122 |
| 8.2.1 | Attributed Reeb graph matching, indexing, and retrieval | 122 |
| 8.2.2 | Entropic minimum spanning Reeb trees for terrain image analysis | 123 |
| 8.2.3 | Divergence measures and information geometry | 123 |
| | List of References | 124 |
| A | Appendix A | 131 |

| | |
|---------------------|------------|
| B Appendix B | 132 |
| C Appendix C | 134 |

List of Tables

| | | |
|-----|---|----|
| 3.1 | MSE's computations for Gaussian noise. | 47 |
| 3.2 | MSE's computations for Laplacian noise | 47 |
| 4.1 | Local shape of a surface. | 53 |
| 6.1 | Jensen-Shannon dissimilarity results for the third set of experiments. | 97 |
| 6.2 | Jensen-Shannon dissimilarity results for the fourth set of experiments. | 98 |

List of Figures

| | | |
|------|---|----|
| 1.1 | Noisy MR image. | 3 |
| 1.2 | Motivation of 3D matching. | 4 |
| 1.3 | Examples of 3D models. | 5 |
| 1.4 | 3D object matching diagram. | 6 |
| 1.5 | Topological equivalence of coffee cup and doughnut. | 7 |
| 2.1 | Image differential operators. | 15 |
| 2.2 | A facial image and its graph. | 16 |
| 2.3 | Image denoising as surface evolution. | 17 |
| 2.4 | Parametric representation of a surface. | 18 |
| 2.5 | Illustration of the Gauss map. | 18 |
| 2.6 | Triangle meshes. | 20 |
| 2.7 | Barycentric triangulation. | 21 |
| 2.8 | Volumetric surface. | 22 |
| 3.1 | Block diagram of image denoising process. | 25 |
| 3.2 | Total variation. | 28 |
| 3.3 | Anisotropic Lagrangians. | 33 |
| 3.4 | Image evolution under flows. | 34 |
| 3.5 | Huber function. | 36 |
| 3.6 | Huber influence function and its smooth version. | 38 |
| 3.7 | Log-Cauchy filtering: (a) contaminated image, (b) filtered image. | 39 |
| 3.8 | Visual comparison of some variational integrands | 42 |
| 3.9 | Improved entropic Lagrangian. | 43 |
| 3.10 | Filtering results for Gaussian noise. | 45 |
| 3.11 | Filtering results for Laplacian noise. | 46 |
| 4.1 | Nondegenerate singular points. | 55 |
| 4.2 | Degenerate singularity: cusp point/curve | 56 |
| 4.3 | A 3-D object and the critical points of its height function. | 57 |

| | | |
|------|--|-----|
| 4.4 | Evolution of image singularities. | 59 |
| 4.5 | Number of degenerate singularities vs. iteration number. | 60 |
| 5.1 | A 3-D object and the critical points of its height function. | 64 |
| 5.2 | Reeb graph representation of a torus. | 65 |
| 5.3 | (a) Self-shadow and cast shadow, (b) illumination of a Lambertian surface. | 66 |
| 5.4 | (a) Shading image, (b) gradient vector field, (c) shading normal field | 67 |
| 5.5 | Reeb graph of the heart model. | 72 |
| 5.6 | Reeb graph of the hand model. | 72 |
| 6.1 | Distance between two arbitrary centroids of a 3D camel. | 77 |
| 6.2 | Block-diagram of the proposed methodology. | 78 |
| 6.3 | Reeb graph representation | 80 |
| 6.4 | Reeb graph of the hand model. | 81 |
| 6.5 | D2 shape distribution of an ellipsoid. | 82 |
| 6.6 | Euclidean vs. geodesic distance on a nonlinear manifold. | 84 |
| 6.7 | Effect of the bandwidth parameter h | 86 |
| 6.8 | Geodesic shape distribution algorithm. | 87 |
| 6.9 | (a) 3D tank model, and its (b) geodesic shape distribution. | 87 |
| 6.10 | Robustness and invariance. | 88 |
| 6.11 | Robustness and invariance (cont.). | 89 |
| 6.12 | (a) 3D plot and (b) contour plot of the Jensen-Shannon divergence. | 90 |
| 6.13 | Illustration of geodesic shape statistical manifold. | 93 |
| 6.14 | First set of experiments: 3D airplanes. | 94 |
| 6.15 | Second set of experiments: 3D tanks. | 95 |
| 6.16 | Third set of experiments: 3D models and their geodesic shape distributions. | 97 |
| 6.17 | Fourth set of experiments: 3D models and their geodesic shape distributions. | 98 |
| 7.1 | Definition of a 2-manifold. | 102 |
| 7.2 | Critical points. | 104 |
| 7.3 | A 3-D object and the critical points of its height function. | 106 |
| 7.4 | Illustration of the height function. | 108 |
| 7.5 | Surface immersed in water. | 110 |
| 7.6 | Reeb graph representation | 111 |
| 7.7 | Illustration of M_a and L_a | 112 |
| 7.8 | Evolution of M_a as a changes. | 113 |
| 7.9 | handle decomposition. | 114 |
| 7.10 | Illustration of the distance function. | 116 |
| 7.11 | Embedding of a 3D airplane into a sphere. | 117 |
| 7.12 | Distance function defined on a torus. | 118 |
| 7.13 | Distance function defined on a torus (cont.). | 118 |
| 7.14 | Distance function defined on a dimple. | 119 |
| 7.15 | Isocontours of 3D real data. | 119 |

Introduction

With the increasing use of scanners to create images, there is a rising need for robust image denoising to remove inevitable noise in the measurements. Even with high-fidelity scanners, the acquired images are invariably noisy, and therefore require filtering. For instance, images extracted from volume data, that is obtained by MRI or CT devices, often contain amounts of noise that must be removed before further processing. Removing noise while preserving the details is, however, no trivial matter since sharp features are often blurred and therefore efficient image denoising techniques are needed. In this thesis, we propose robust variational models for image denoising by solving partial differential equations. The core idea behind our proposed approaches is to use geometric insight in helping construct regularizing functionals and avoiding a subjective choice of a prior in maximum a posteriori estimation. Using tools from robust statistics and information theory, we show that we can extend this strategy and develop two gradient descent flows for image denoising with a demonstrated performance.

The major part of this thesis is devoted to a joint exploitation of geometry and topology of objects for as parsimonious as possible representation of objects and its subsequent application in object classification and recognition. The key idea consists of capturing geometry along all topologically homogeneous parts of an object by way of level curves superimposed on a Reeb graph usually extracted by way of the object critical points. A Reeb graph is a topological representation of the connectivity of a surface between critical points which represent the nodes of the graph, and the edges of the graph represent the connected components of the surface. Specifically, given a function defined on a surface or 2-manifold, a Reeb graph may be used to track its connected

components as the pre-image of the function. For the example of using a height function, the Reeb graph would contain nodes for each of the contours for each level set generated by the height function. The resulting skeletal representation, however, is not rotationally invariant due to the rotational non-invariance of the height function. We propose a new methodology called *geodesic shape distribution* that lifts this limitation and which we apply to three-dimensional object matching. The central idea is to encode a 3D shape into a 1D geodesic shape distribution. Object matching is then achieved by calculating an information-theoretic measure of dissimilarity between resulting probability distributions. That is, the dissimilarity computations are carried out in a low-dimensional space of geodesic shape distributions.

1.1 Framework and motivation

1.1.1 Image denoising

Image denoising refers to the process of recovering an image contaminated by noise. The challenge of the problem of interest lies in faithfully recovering the original image from the observed image, and furthering the estimation by making use of any prior knowledge/assumptions about the noise process. The problem of image denoising has been addressed using a number of different techniques including wavelets [49], order statistics based filters [17], PDE-based algorithms [30,76], and variational approaches [26,27,6]. In particular, a large number of PDE-based methods have particularly been proposed to tackle the problem of image denoising [4,23,25] with a good preservation of edges. Much of the appeal of PDE-based methods lies in the availability of a vast arsenal of mathematical tools which at the very least act as a key guide in achieving numerical accuracy as well as stability. Partial differential equations or gradient descent flows are generally a result of variational problems using the Euler-Lagrange principle [36].

Most medical imaging methods, for instance, produce full three-dimensional volumes. Traditionally, the medical scans are viewed as a series of superposed two-dimensional slices of the full 3D volume, and are also perturbed by noise in the course of acquisition, transmission or processing. Figure 1.1 illustrates a 2D noisy slice of a 3D MR head.

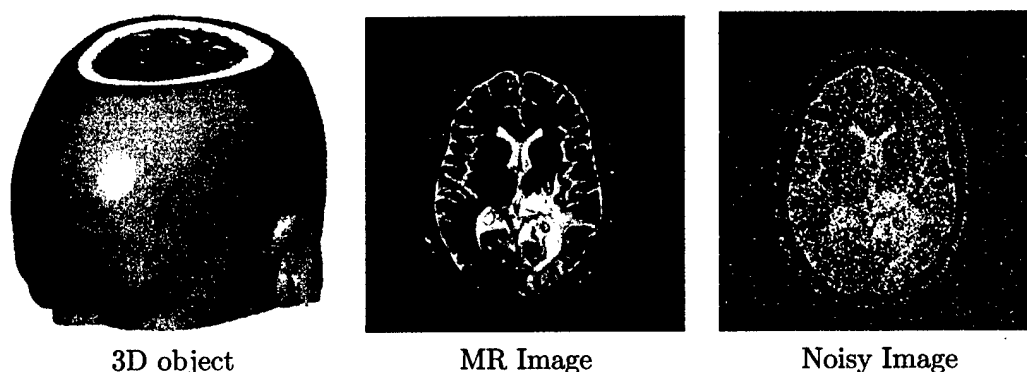


Figure 1.1: Noisy MR image.

1.1.2 Object recognition

Three-dimensional objects consist of geometric and topological data, and their compact representation is an important step towards a variety of computer vision applications including indexing, retrieval, and matching in a database of 3D models. The latter will be the focus of Chapter 6, and the motivation behind considering 3D objects is illustrated in Figure 1.2.

3D models do not depend on the configuration of cameras, light sources, or surrounding objects. As a result, they do not contain reflections, shadows, occlusions, projections, or partial objects, which in turn greatly simplifies finding matches between objects of the same type. For example, it is plausible to expect that the 3D model of a Boeing747 contains exactly four engines. In contrast, any 2D image of this Boeing747 may contain fewer than four engines (if some of the engines are occluded), or it may contain “extra engines” appearing as the result of shadows.

In other respects, representing and processing 3D models is more complicated than for sampled multimedia data. The main difficulty is that 3D surfaces rarely have simple parameterizations. Since 3D surfaces can have arbitrary topologies, many useful methods for analyzing other media (e.g., Fourier analysis) have no obvious analogs for 3D surface models. Moreover, the dimensionality is higher, and this makes searches for pose registration, feature correspondences, and model parameters more difficult.

In order to perform 3D matching and to carry out the experiments, first we need a database of

- 2D provides the grayscale/color information in the plane: lost of depth information
- e.g.: 2D images of F-16s and MiG-23s look very similar, but in 3D are different
- 3D is much more effective for recognition and display
- 3D applications: industry, medicine, search, video games and cinema

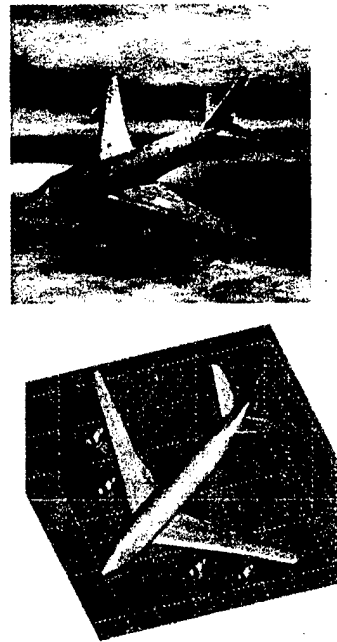


Figure 1.2: Motivation of 3D matching.

3D models, and a small subset of our large database is depicted in Figure 1.3. We collected several hundred models which consist of military objects, human body parts, animals and other objects.

There are two major techniques for 3D object recognition: feature-based and global methods as depicted in Figure 1.4. Most three-dimensional shape matching techniques proposed in the literature of computer graphics, computer vision and computer-aided design are based on geometric representations which represent the features of an object in such a way that the shape dissimilarity problem reduces to the problem of comparing two such object representations. Feature-based methods require that features be extracted and described before two objects can be compared.

An alternative to feature-based representations is global methods. The idea here is to represent an object by a global measure or shape distribution defined on the surface of the object. The shape matching problem is then performed by computing a dissimilarity measure between the shape distributions of two arbitrary objects.

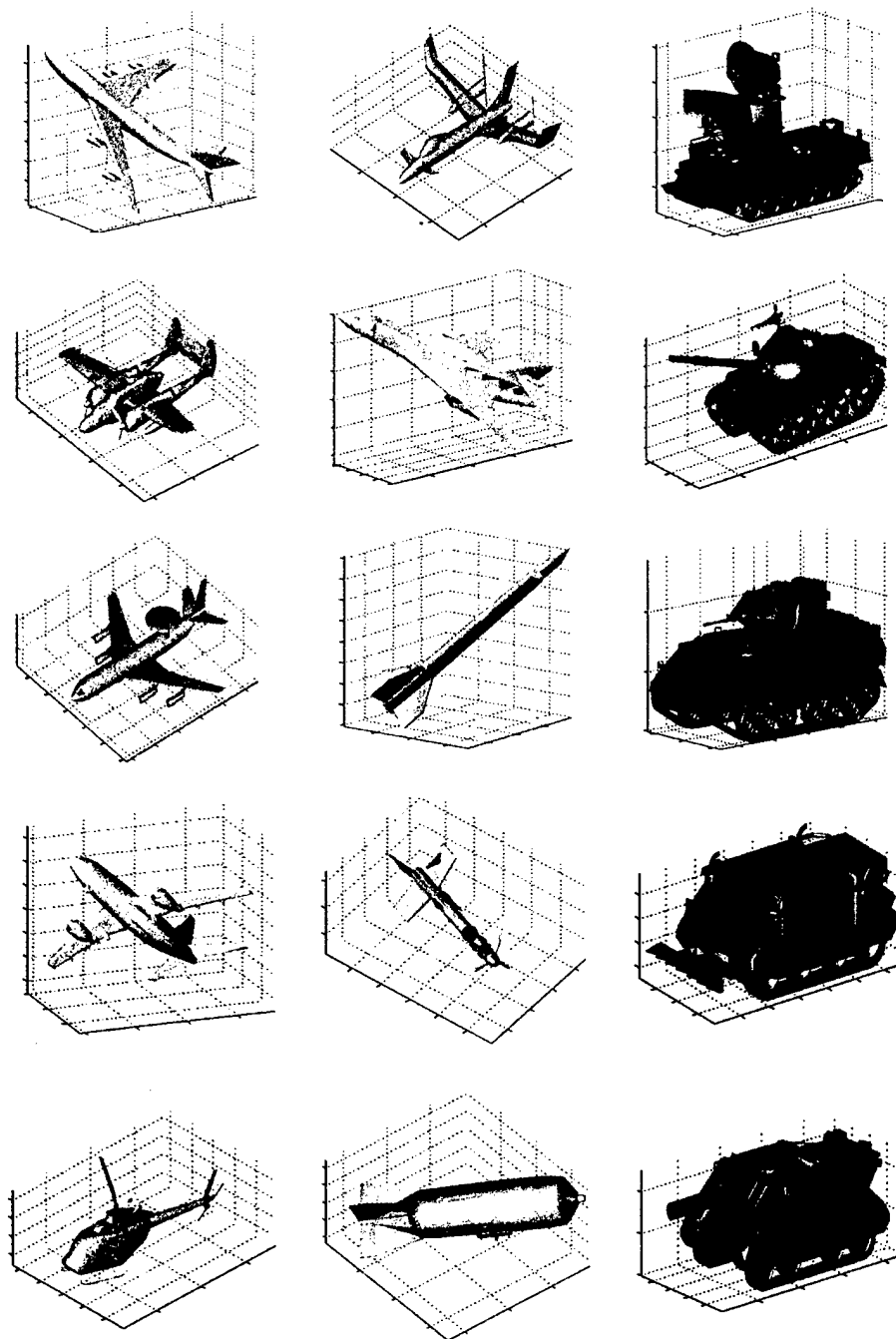


Figure 1.3: Examples of 3D models.

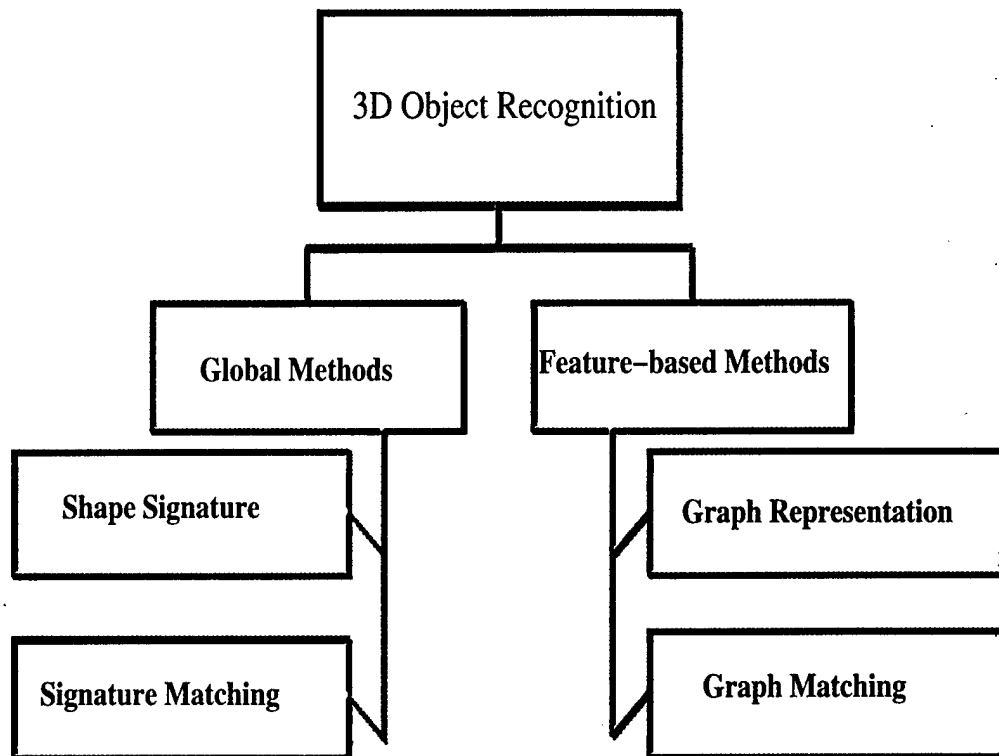


Figure 1.4: 3D object matching diagram.

1.1.3 Joint exploitation of geometry and topology

Although topology is the study of the “shape” of curves and surfaces, topology typically is not concerned with the embedding of that curve or surface. For example, topology is concerned with the fact that if you remove a point from a circle, it becomes a line segment. This is true whether the circle is an ellipse or whether the circle has knots in it. In computer graphics, one cares about the embedding and geometry of a surface. If one were asked to create a digital representation of a coffee cup, no one would be happy if you returned a model that looked like a doughnut. Even though you have returned an object with the correct topological shape, the geometrical shape is incorrect. For computer graphics, we typically are not concerned with purely topological aspects of a surface. Thus, the algorithms we introduce, are founded on computational topology, but consider

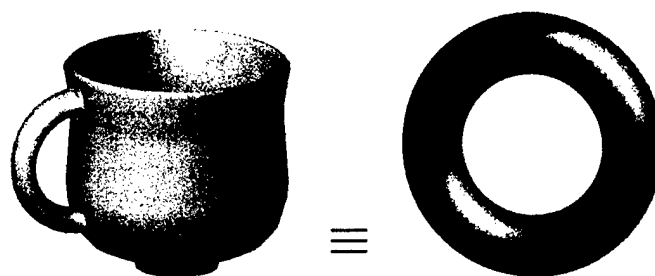


Figure 1.5: Topological equivalence of coffee cup and doughnut.

geometric aspects of the surface, for example, the geodesic distance is a global geometric measure. This interplay of geometry and topology is inherent in the discrete nature of the surfaces used in the field of computer graphics where great care is taken with the geometry of a surface, as the geometry plays such an important role in determining the appearance of a surface. Although a coffee cup is topologically equivalent to a doughnut, geometrically the shapes differ as shown in Figure 1.5. And the difference in their appearance matters greatly when the goal is to accurately represent the appearance of real world objects. Thus, a great deal of work in computer graphics has focused on geometric aspects of a surface, including geometry acquisition, geometry simplification, geometry smoothing and geometry compression. However, there is a direct relationship between the topology and the geometry of a surface that cannot be ignored. Alternatively, many mathematicians and computational topologists are concerned with studying purely topological properties of a surface. This thesis takes a combined approach and identifies and localizes topological features within a surface by mixing topological and geometrical approaches.

The connection between geometry and topology is given by a topological invariant called *genus*. The genus of a surface counts how many “handles” or “holes” the surface has, and two surfaces having the same genus are called *topologically equivalent*. Genus is a global invariant for the surface and its scalar value provides one measure of the complexity of the surface (e.g., a genus zero shape is much less complex than a surface with higher genus). For example, the coffee cup and doughnut shown in Figure 1.5 have the same genus equal to one.

1.2 Contributions

The contributions of this thesis are as follows:

- ☛ **Robust and efficient variational filters for image denoising:** Using the theoretical fundamentals of robust statistics, a variational filter referred to as a Huber gradient descent flow is proposed. It is a result of optimizing a Huber functional subject to some noise constraints, and it takes a hybrid form of a total variation diffusion for large gradient magnitudes and of a linear diffusion for small gradient magnitudes. Using the gained insight, and as a further extension, we propose an information-theoretic gradient descent flow which is a result of minimizing a functional that is a hybrid between a negentropy variational integral and a total variation. Illustrating experimental results demonstrate a much improved performance of the approach in the presence of Gaussian and heavy tailed noise.
- ☛ **A Topological Variational Model for Image Singularities:** Image singularities are prominent landmarks and their detection, recognition, and classification is a crucial step in image processing and computer vision. Such singularities carry important information for further operations, such as image registration, shape analysis, motion estimation, and object recognition. In this thesis, we propose a topological gradient descent flow for image singularities. The approach is expressed in the higher order variational framework as a minimizer of a variational integral involving the gradient and the Hessian matrix of the height function defined on a manifold. We demonstrate through numerical simulations the power of the proposed technique in preserving image singularities.
- ☛ **Topological modeling of illuminated surfaces using Reeb graph:** We introduce a reliable and efficient feature based object representation for topological modeling of three dimensional illuminated surfaces. The proposed approach encodes an object into the Reeb graph concept from computational topology. This skeletal structure is based on a generalized height function in the light direction defined on an illuminated surface. In this thesis, the topological properties of the proposed representation are analyzed in the Morse theoretic

framework, and its close relationship to the shading problem is also highlighted. Some numerical simulations with synthetic and real 3D data are provided to demonstrate the potential of object singularities in topological modeling.

☛ **Geodesic Object Representation and Recognition:** We propose a shape signature that captures the intrinsic geometric structure of 3D objects. The primary motivation of the proposed approach is to encode a 3D shape into a one-dimensional geodesic distribution function. This compact and computationally simple representation is based on a global geodesic distance defined on an object surface, and takes the form of a kernel density estimate. To gain further insight into the geodesic shape distribution and its practicality in 3D computer imagery, some numerical experiments are provided to demonstrate the potential and the much improved performance of the proposed methodology in 3D object matching. This is carried out using an information-theoretic measure of dissimilarity between probabilistic shape distributions.

☛ **Distance Function-based Object Recognition:** We introduce a topological approach to object recognition using a distance function. Similarly to the height function strategy which consists of reconstructing surface from its cross-sections, the key idea behind using a distance function is that a surface may be reconstructed from its intersections with concentric spheres centered at the centroid of the underlying surface. As the distance function traverses the surface and the number of intersecting contours changes for various distances (i.e. radii of concentric spheres) from the barycenter point, the topology of the surface varies as well.

1.3 Thesis overview

The organization of this thesis is as follows:

- ☐ The **Background** Chapter contains a brief review of essential concepts and definitions which we will refer to throughout the thesis, and presents a short summary of material relevant to variational methods, geometric modeling and computational topology.

- In Chapter 3, we present a variational approach to maximum *a posteriori* estimation MAP estimation. The key idea behind this approach is to use geometric insight in helping construct regularizing functionals and avoiding a subjective choice of a prior in MAP estimation. Using tools from robust statistics and information theory, we show that we can extend this strategy and develop two gradient descent flows for image denoising with a demonstrated performance.
- In Chapter 4, we propose a geometric/topological variational model to preserve degenerate image singularities. Such singularities carry important information for a variety of image processing and computer vision operations, such as image registration, shape analysis, object recognition, etc. The approach is expressed in the higher order variational framework, and it is based on a variational integral involving the gradient and the Hessian matrix of the height function defined on a manifold.
- Chapter 5 is devoted to a formulation of object singularities in a Morse theoretic setting. Then, we analyze the Reeb graph representation in the shading problem framework, and we derive some relevant theoretical properties of the height function in the light direction of an illuminated 3D object. In addition, we prove that such a height function is closely related to the generalized bas-relief transformation.
- In Chapter 6, we propose a new approach for object matching based on a global geodesic measure. The key idea behind our methodology is to represent an object by a probabilistic shape descriptor called *geodesic shape distribution* that measures the global geodesic distance between two arbitrary points on the surface of an object. In contrast to the Euclidean distance which is more suitable for linear spaces, the geodesic distance has the advantage of its ability to capture the (nonlinear) intrinsic geometric structure of the data. The geodesic shape distribution may be used to facilitate representation, indexing, retrieval, and object matching in a database of 3D models. More importantly, the geodesic shape distribution provides a new way to look at the object matching problem by understanding the intrinsic geometry of the shape. The matching task therefore becomes a one-dimensional comparison problem between probability distributions which is clearly much simpler than comparing 3D structures. Object

matching can then be carried out by dissimilarity measure calculations between geodesic shape distributions, and is in addition computationally efficient and inexpensive.

- Chapter 7 is devoted to the distance function-based approach to topological modeling using Morse theory. Despite the theoretical nature of the results presented in this Chapter, the key idea is to identify and encode regions of topological interest of 3D object in the Morse-theoretic framework. The main motivation behind using the distance function is its rotation invariance which makes it more adapted to object recognition than the Morse height function. We prove that a surface may be reconstructed from its intersections with concentric spheres centered at the barycenter of the underlying surface. The topological changes in the surface occur as we increase the value of the sphere radius. At singular points, the level curves of the distance function may split or merge which indicate topological changes. We also show that when a surface is embedded in a sphere, the height function and the distance function are equivalent in a Morse-theoretic setting, that is both functions have the same singularities.
- In the **Conclusions** Chapter, we summarize the contributions of this thesis, and we propose several future research directions that are directly or indirectly related to the work performed in this thesis.

1.4 Publications

- ✉ A. Ben Hamza, Hamid Krim, and Gozde Unal, "Unifying probabilistic and variational estimation," *IEEE Signal Processing Magazine*, vol. 19, no. 5, pp. 37-47, September 2002.
- ✉ Yun He, A. Ben Hamza, and Hamid Krim, "A generalized divergence measure for robust image registration," *IEEE Transactions on Signal Processing*, vol. 51, no. 5, pp. 1211-1220, May 2003.
- ✉ A. Ben Hamza, Hamid Krim, and Josiane Zerubia, "A nonlinear entropic variational model for image filtering," *EURASIP Journal on Applied Signal Processing*, under review 2003.

- ✎ A. Ben Hamza and Hamid Krim, "A Variational approach to maximum a posteriori estimation for image denoising," *Lecture Notes in Computer Science*, vol. 2134, pp. 19-34, 2001.
- ✎ A. Ben Hamza and Hamid Krim, "Geodesic object representation and recognition," *Lecture Notes in Computer Science*, to appear 2003.
- ✎ A. Ben Hamza and Hamid Krim, "Image registration and segmentation by maximizing Jensen-Renyi divergence," *Lecture Notes in Computer Science*, vol. 2683, pp. 147-163, 2003.
- ✎ A. Ben Hamza and Hamid Krim, "Robust environmental image denoising," *ISI International Conference on Environmental Statistics and Health*, 2003.
- ✎ A. Ben Hamza and Hamid Krim, "Robust influence functionals for image filtering," *Proc. IEEE International Conference on Image Processing*, Barcelona, Spain, 2003.
- ✎ A. Ben Hamza and Hamid Krim, "A topological skeleton of illuminated manifolds," *Proc. IEEE International Conference on Image Processing*, Barcelona, Spain, 2003.
- ✎ A. Ben Hamza and Hamid Krim, "Jensen-Renyi divergence measure: theoretical and computational perspectives," *Proc. IEEE International Symposium on Information Theory*, 2003.
- ✎ A. Ben Hamza and Hamid Krim, "A topological variational model for image singularities," *Proc. IEEE International Conference on Image Processing*, Rochester, NY, 2002.
- ✎ A. Ben Hamza and Hamid Krim, "Towards a unified view of estimation: variational vs. statistical," *Proc. IEEE International Conference on Image Processing*, October 2001.

Background

This thesis addresses the application of computational geometry and topology algorithms to images and three-dimensional surfaces. The following background material is presented to provide context for this work. First, a representation of images in the continuous domain is presented along with some basic differential operators used throughout this work. Then, a discussion of the various surface representations of three-dimensional objects is presented.

2.1 Continuous representation of images

In the variational setting, an image is usually defined in the continuous domain which enjoys a large arsenal of analytical tools, and hence offers a greater flexibility. An image is therefore defined as a real-valued function $u : \Omega \rightarrow \mathbb{R}$, where Ω is a nonempty, bounded, open set in the real plane \mathbb{R}^2 (usually Ω is a rectangle in \mathbb{R}^2).

2.1.1 Differentiability of images

A pixel location in Ω is denoted by $\mathbf{x} = (x, y)$, and the gradient of u is denoted by $\nabla u = (u_x, u_y)^T$, where u_x and u_y are the first-order partial derivatives with respect to x and y respectively. These derivatives are illustrated in Figures 2.1(b) and (c). In image analysis, the image gradient defines the orientation of an edge at a given image point. The gradient orientation or direction $\theta = \arctan(u_y/u_x)$ gives the orientation of the edge as shown in Figure 2.1(d). An edge in an image is a contour across which the image intensity changes abruptly. Image edges are usually considered to be discontinuities

of the image intensity function. The gradient magnitude $\|\nabla u\| = \sqrt{u_x^2 + u_y^2}$ gives the strength of the edge, and it defines an edge image whose pixels are bright only near an edge as depicted in Figure 2.1(e). To detect edges of any orientation, first we compute the gradient of the image, then compute the gradient magnitude at every pixel, and then label as “edge pixels” all pixels whose gradient magnitude is above a pre-determined threshold.

The Hessian matrix $\nabla^2 u$ of an image u is defined as the matrix of second-order partial derivatives

$$\nabla^2 u = \begin{pmatrix} u_{xx} & u_{xy} \\ u_{xy} & u_{yy} \end{pmatrix},$$

and its Laplacian is defined as the divergence of the gradient or the trace of the Hessian matrix

$$\Delta u = \nabla \cdot (\nabla u) = \text{div}(\nabla u) = u_{xx} + u_{yy} = \text{Tr}(\nabla^2 u).$$

Another way to detect edges is to use zero-crossing of the Laplacian which crosses zero in the neighborhood of an edge, and this technique can be used without relying on a threshold. The Laplacian image is depicted in Figure 2.1(f).

The Hessian matrix of an image consists of three terms u_{xx} , u_{yy} and u_{xy} . The Laplacian ignores the third term and returns the average value of the second derivative when taking every orientation into account. While the Laplacian ignores one of them and considers every possible orientation at once, the Hessian takes all three terms into account and is orientation-dependent. The largest eigenvalue of the Hessian determines the orientation along which the second derivative is maximal, while the smallest eigenvalue of the Hessian returns the minimum of the second derivative.

2.2 Three-dimensional surfaces

Surfaces have been studied by mathematicians for centuries. Typically mathematicians conceive of surfaces as continuous, for example a surface may be defined as a continuous function of two variables. Each surface has a variety of attributes. For example, the surfaces typically used in computer graphics are oriented 2-manifolds with or without boundary. A 2-manifold is a surface where the local area around every point on the surface is Euclidean, meaning, around each point

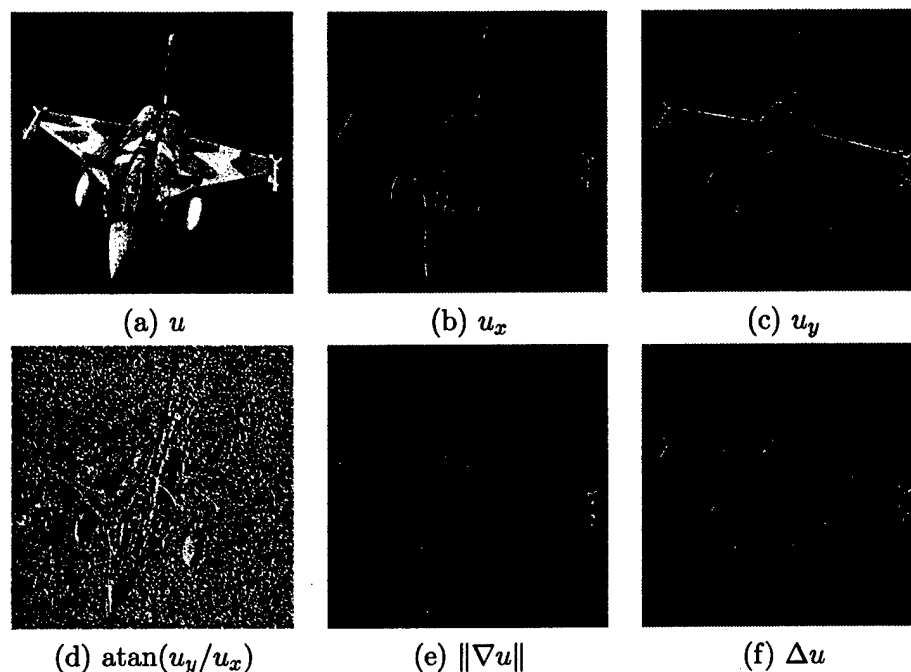


Figure 2.1: Image differential operators.

the surface appears to be nearly flat. The world we live on is an excellent example of a 2-manifold. Manifolds are a preferable surface representation because the surface can be divided into regions called *charts* which allow 2-manifolds embedded in 3D to be flattened into a two dimensional domain (through parametrization). Surfaces used in computer graphics are typically oriented, this refers to the fact that the surface has two sides. For example, a sphere has two sides, while a Mobius strip has only one side. Another attribute of surfaces is whether the surface is closed or with boundary. This refers to the number of open boundary components of a surface. For example, an egg shell is closed but once it has been cracked open, it becomes a surface with boundaries.

2.2.1 Image graph

To apply and benefit from the tools of geometry in image analysis, it is convenient to consider the graph of an image u which is a surface (2-dimensional manifold) $M \subseteq \mathbb{R}^3$ defined as $M = \{(x, y, z) : z = u(x, y)\}$ where $z = u(x, y)$ is the gray level at position (x, y) on the image domain Ω . An image

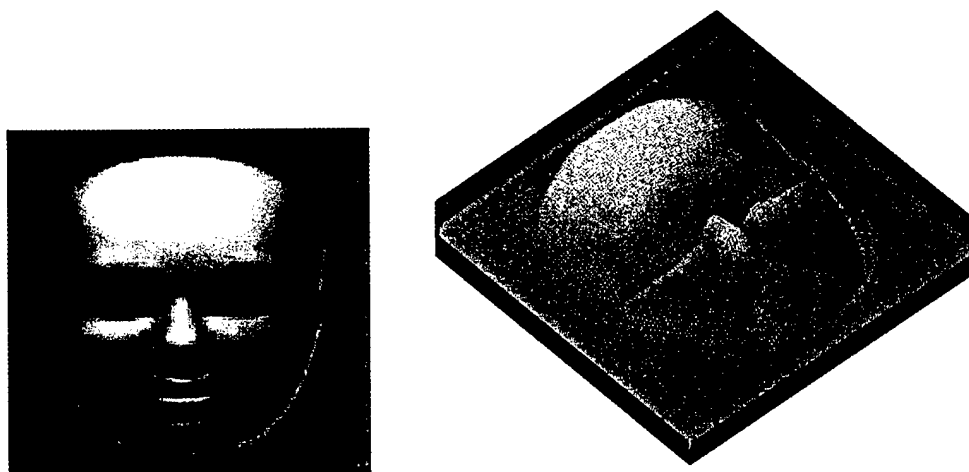


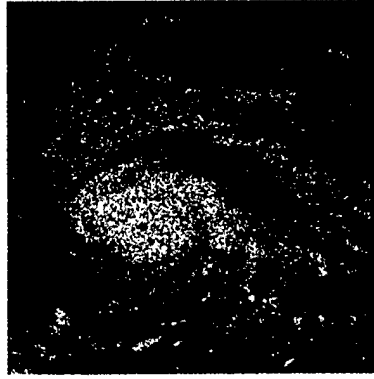
Figure 2.2: A facial image and its graph.

and its surface representation are depicted in Figure 2.2.

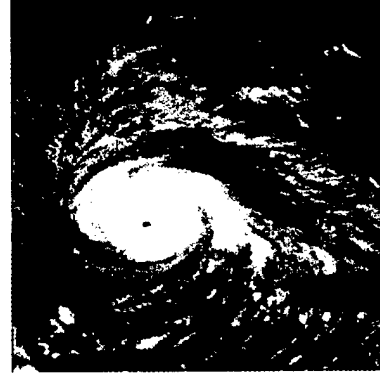
Inspired by this surface representation, the image denoising problem may be viewed as surface smoothing. This may be carried out by minimizing an energy functional with regularization terms that evolve the noisy surface to the optimal solution as depicted in Figure 2.3.

In order to allow partial differentiation and consequently all the features of differential calculus on \mathbb{M} , we need to consider a smooth image u , that is has continuous partial derivatives of all orders, so that the manifold \mathbb{M} is differentiable. Thus the study of this differential manifold involves topology, since differentiability implies continuity. A common way to smooth an image u is to embed it into a family of images known as *scale-space image*. For example, a Gaussian scale-space image which is the result of convolving an image with the bivariate Gaussian density. A parametric representation of \mathbb{M} is the Monge patch defined by $\mathbf{r} : \Omega \rightarrow \mathbb{M}$ such that $\mathbf{r}(x, y) = (x, y, u(x, y))$. Note that the patch \mathbf{r} covers all \mathbb{M} , that is, $\mathbf{r}(\Omega) = \mathbb{M}$, and it is regular, that is, $\mathbf{r}_x \times \mathbf{r}_y \neq 0$ or equivalently, the Jacobian matrix of \mathbf{r} has rank 2. Figure 2.4 illustrates a parametric representation of a surface.

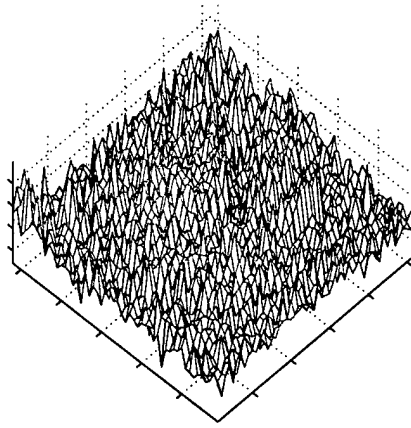
It is worth pointing out that the Monge patch $\mathbf{r} : \Omega \rightarrow \mathbb{M}$ of a smooth image $u : \Omega \rightarrow \mathbb{R}$ is a diffeomorphism because it is a smooth bijection, and its inverse \mathbf{r}^{-1} is the restriction to \mathbb{M} of the



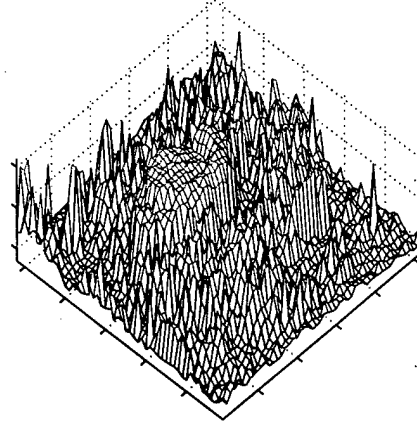
(a) Noisy image



(b) Filtered image



(c) Noisy surface



(d) Filtered surface

Figure 2.3: Image denoising as surface evolution.

smooth projection $\pi : \Omega \times \mathbb{R} \rightarrow \Omega$, that is $\mathbf{r}^{-1} = \pi|_{\mathbf{M}}$.

Let $\mathbf{p} \in \mathbf{M}$, then there exists $(x, y) \in \Omega$ such that $\mathbf{p} = \mathbf{r}(x, y)$. Hence, the unit normal N to \mathbf{M} is given by

$$N(\mathbf{p}) = N(\mathbf{r}(x, y)) = \frac{\mathbf{r}_x \times \mathbf{r}_y}{\|\mathbf{r}_x \times \mathbf{r}_y\|} = \frac{(-u_x, -u_y, 1)}{\sqrt{1 + u_x^2 + u_y^2}}. \quad (1)$$

The unit normal is the most elementary differential characteristics of a surface and determines the tangent plane $T_{\mathbf{p}}\mathbf{M}$ at a surface point $\mathbf{p} = \mathbf{r}(x, y)$. The tangent plane can be defined as the set of vectors that are orthogonal to the surface unit normal. Since \mathbf{r} is regular, it follows that the unit

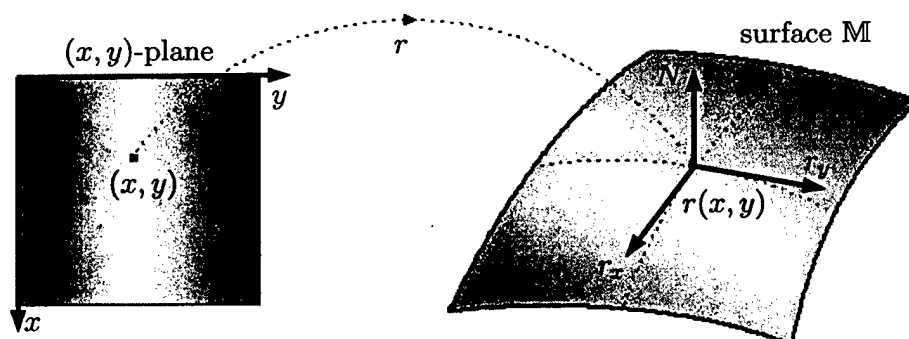


Figure 2.4: Parametric representation of a surface.

normal is well-defined everywhere, and therefore the image graph M is orientable. For notational convenience, the unit normal can be viewed as a mapping $g : \Omega \rightarrow \mathbb{S}^2$, called *Gauss map* of r and is defined as $g(x, y) = N(r(x, y))$, where $\mathbb{S}^2 = \{p \in \mathbb{R}^3 : \|p\| = 1\}$ is the unit sphere. Note that $g(x, y)$ denotes the values of the unit Gauss map at $p = r(x, y)$ as illustrated in Figure 2.5.

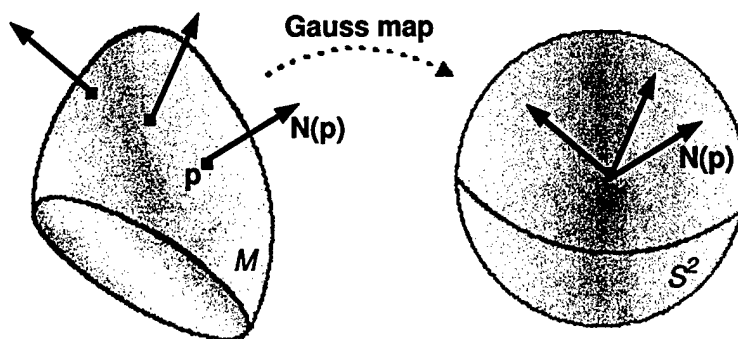


Figure 2.5: Illustration of the Gauss map.

2.2.2 Triangle mesh

In computer graphics, 3D objects are usually represented as a triangle mesh $\mathbb{M} = (\mathcal{V}, \mathcal{T})$, where $\mathcal{V} = \{v_1, \dots, v_m\}$ is the set of vertices, and $\mathcal{T} = \{T_1, \dots, T_n\}$ is the set of triangles. Triangle meshes are used so frequently to represent surfaces in the discrete domain that most computer graphics hardware is optimized to render triangles. Example of triangle meshes are depicted in Figure 2.8. For triangulation, we use the barycentric subdivision illustrated in Figure 2.7. This technique consists in introducing a new vertex at the center of each triangle and a new vertex at the midpoint of each edge and drawing edges from the centroid of the triangle to each of the new midpoint vertices and to the original vertices.

2.2.3 Scalar volume and isosurface

Another common discrete surface representation is an isosurface in a scalar volume as pictured in Figure 2.8. A scalar volume consists of a regularly sampled 3D grid of scalar values. Scalar volumes are typically acquired from real world data from various sources, such as, magnetic resonance imaging (MRI) and computed Tomography (CT) imaging. These popular imaging techniques are used in a variety of medical and scientific applications to view and analyze three dimensional structures.

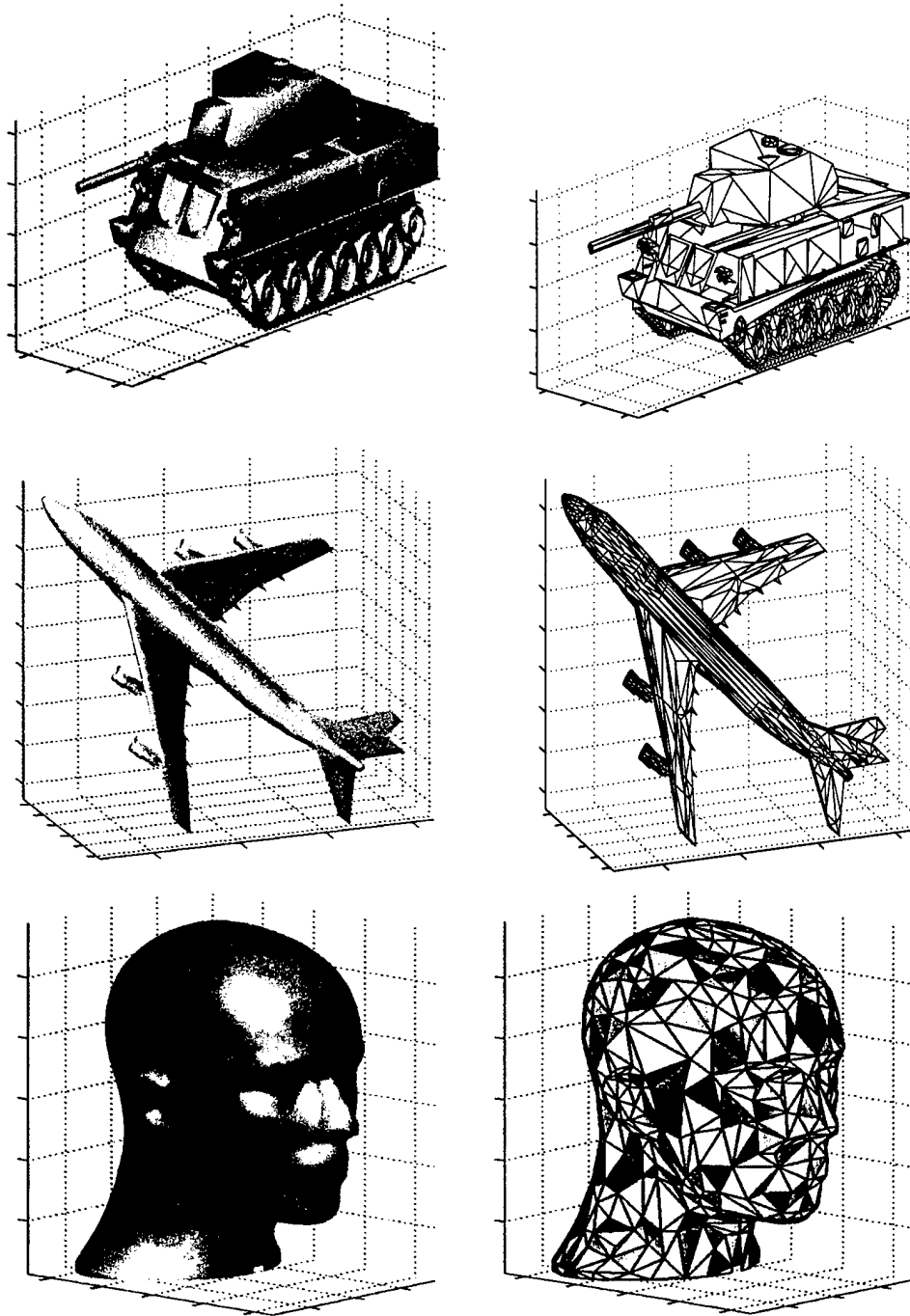


Figure 2.6: Triangle meshes.

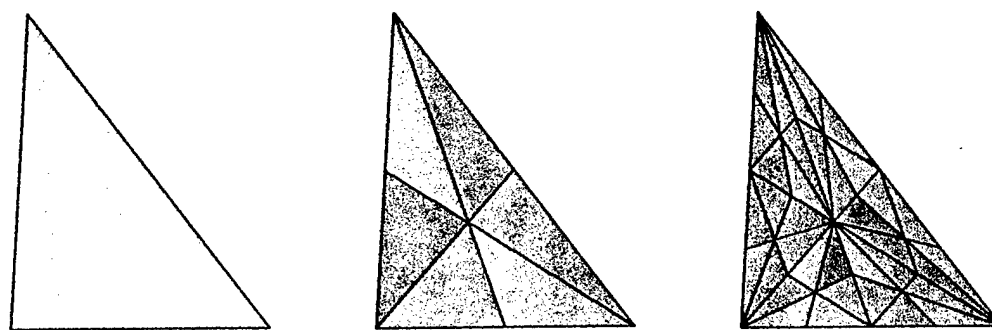
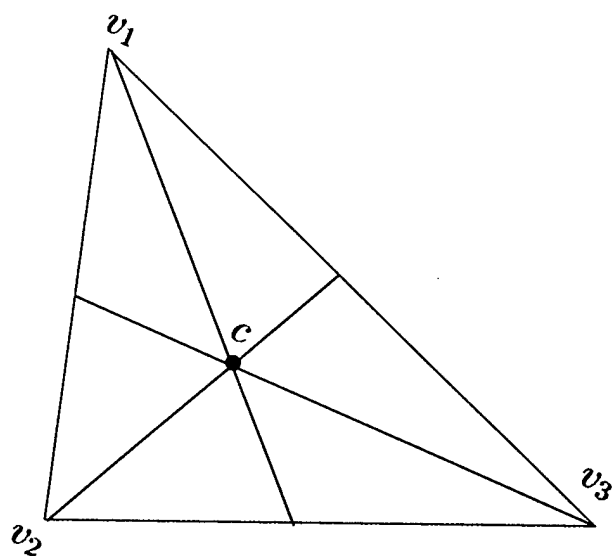


Figure 2.7: Barycentric triangulation.

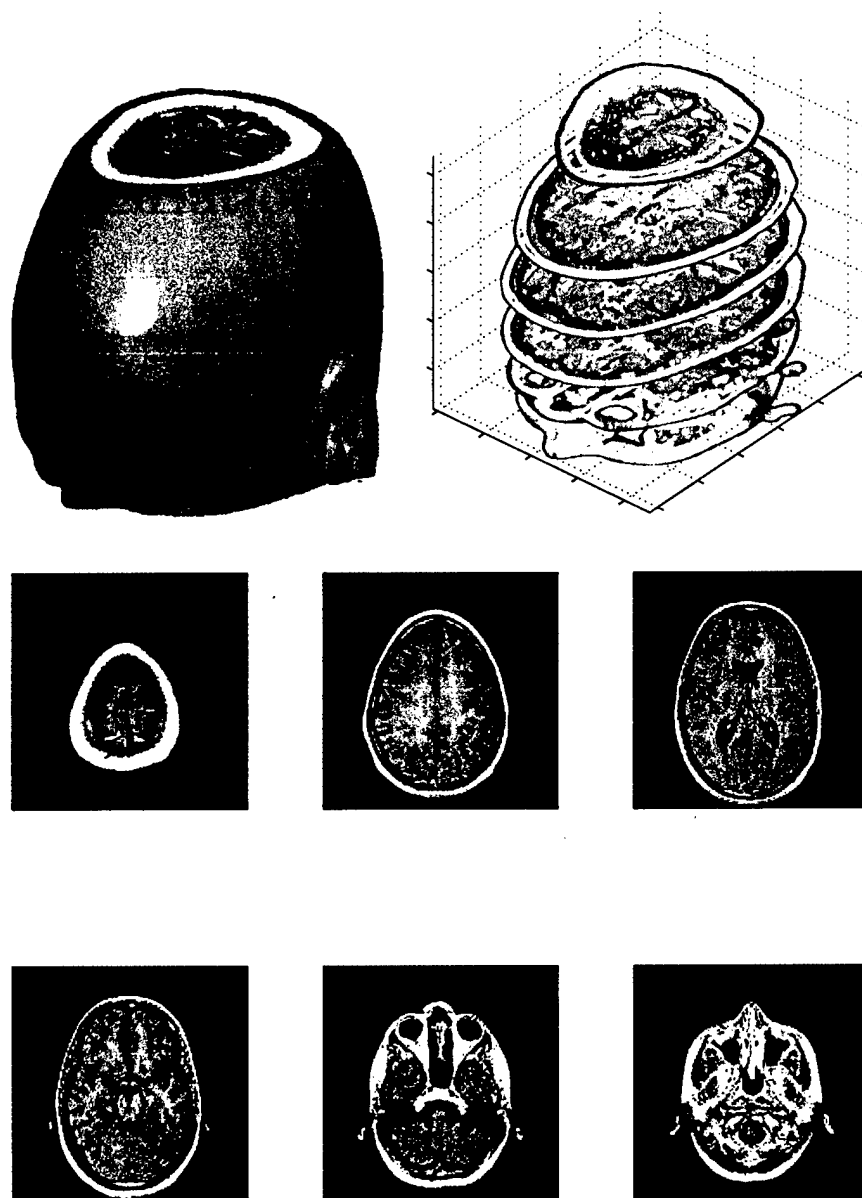


Figure 2.8: Volumetric surface.

Robust Variational Image Denoising

In this chapter, we present a variational approach to MAP estimation [6, 7]. The core idea behind this approach is to use geometric insight in helping construct regularizing functionals and avoiding a subjective choice of a prior in MAP estimation [8]. Using tools from robust statistics and information theory, we show that we can extend this strategy and develop two gradient descent flows for image denoising with a demonstrated performance [8, 9].

3.1 Introduction

In recent years, variational methods and partial differential equations (PDE) based methods [57, 61, 1, 65, 2, 74] have been introduced to explicitly account for intrinsic geometry to address a variety of problems including image segmentation, mathematical morphology, motion estimation, image classification, and image denoising [56, 62, 30, 47, 66, 4]. The latter will be the focus of the present chapter. The problem of signal/image denoising has been addressed using a number of different techniques including wavelets [49], order statistics based filters [17], PDE-based algorithms [30, 76], and variational approaches [26, 27, 6]. In particular, a large number of PDE-based methods have particularly been proposed to tackle the problem of image denoising [4, 23, 25] with a good preservation of edges. Much of the appeal of PDE-based methods lies in the availability of a vast arsenal of mathematical tools which at the very least act as a key guide in achieving numerical accuracy as well as stability. Partial differential equations or gradient descent flows are generally a result of variational problems using the Euler-Lagrange principle [36]. One popular variational

technique used in image denoising is the total variation based approach. It was developed in [65] to overcome the basic limitations of all smooth regularization algorithms, and a variety of numerical methods have also recently been developed for solving total variation minimization problems [43,24].

In the next section, a general formulation of signal/image denoising problem is stated. In Section 3.3, we briefly recall the MAP estimation technique, and in Section 3.4 we formulate the problem of MAP estimation in the calculus of variations setting. Section 3.5 is devoted to a robust variational formulation using concepts borrowed from robust estimation, followed by a probabilistic interpretation of the nonlinear anisotropic diffusion in the the order statistics framework. In Section 3.6, information-theoretic variational flows based on the differential entropy are proposed. In Section 3.7, we provide experimental results to demonstrate a much improved performance of the proposed gradient descent flows in image denoising. Finally, some conclusions and discussions are included in Section 3.8.

3.2 Problem statement

In all real applications, measurements are perturbed by noise. In the course of acquiring, transmitting or processing a digital image for example, the noise-induced degradation may be dependent or independent of data. The noise is usually described by its probabilistic model, e.g., Gaussian noise is characterized by two moments. Application-dependent, a degradation often yields a resulting signal/image observation model, and the most commonly used is the additive one,

$$u_0 = u + \eta, \tag{1}$$

where the observed image u_0 includes the original signal u and the independent and identically distributed (i.i.d) noise process η .

Image denoising refers to the process of recovering an image contaminated by noise (see Figure 3.1). The challenge of the problem of interest lies in faithfully recovering the underlying signal/image u from u_0 , and furthering the estimation by making use of any prior knowledge/assumptions about the noise process η . This goal is graphically and succinctly described in Figure 3.1.

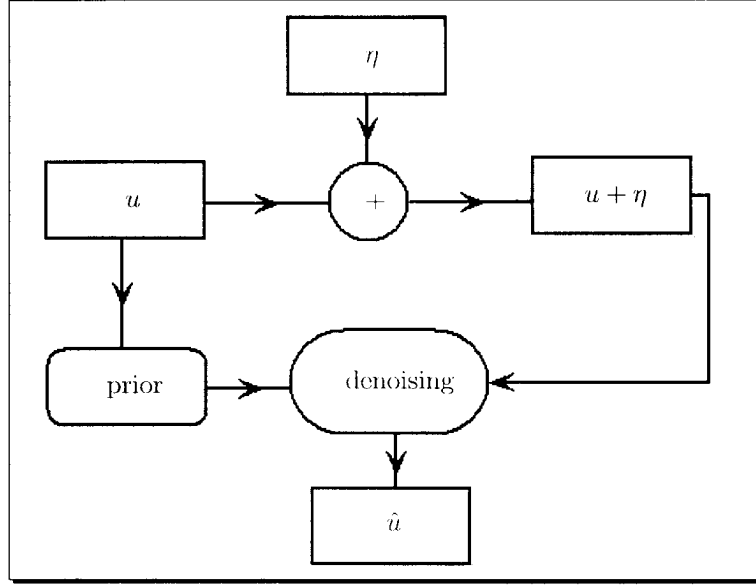


Figure 3.1: Block diagram of image denoising process.

3.3 MAP estimation: model-based approach

In a probabilistic setting, the image denoising problem is usually solved in a discrete domain, and in this case an image is expressed by a random matrix $u = (u_{ij})$ of gray levels. To account for prior probabilistic information we may have for u , a technique of choice is that of a maximum a posteriori estimation. Denoting by $p(u)$ the prior distribution for the unknown image u , the MAP estimator is given by

$$\hat{u} = \arg \max_u \{ \log p(u_0|u) + \log p(u) \}, \quad (2)$$

where $p(u_0|u)$ denotes the conditional probability of u_0 given u .

A general model for the prior distribution $p(u)$ is that of a Markov random field (MRF) which is characterized by its Gibbs distribution given by [33]

$$p(u) = \frac{1}{Z} \exp \left\{ -\frac{\mathcal{F}(u)}{\lambda} \right\},$$

where Z is a partition function and λ is a constant known as the temperature in the terminology

of physical systems. \mathcal{F} is called the *energy function* and has the form $\mathcal{F}(u) = \sum_{c \in \mathcal{C}} V_c(u)$, where \mathcal{C} denotes a set of cliques (i.e. set of connected pixels) for the MRF, and V_c is a potential function defined on a clique. We may define the cliques to be adjacent pairs of horizontal and vertical pixels. Note that for large λ , the prior probability becomes flat, and for small λ , the prior probability exhibits sharp modes.

Markov random fields have been extensively used in computer vision particularly for image restoration, and it has been established that Gibbs distributions and MRF's are equivalent (e.g. see [33]). In other words, if a problem is defined in terms of local potentials then there is a simple way of formulating the problem in terms of MRF's. If the noise process η is i.i.d. Gaussian, then we have

$$p(u_0|u) = K \exp \left(-\frac{|u - u_0|^2}{2\sigma^2} \right),$$

where K is a normalizing positive constant, σ^2 is the noise variance, and $|\cdot|$ stands for the Euclidean norm or for the absolute value in the case of a scalar. Thus, the MAP estimator in (2) yields

$$\hat{u} = \arg \min_u \left\{ \mathcal{F}(u) + \frac{\lambda}{2} |u - u_0|^2 \right\}. \quad (3)$$

Image estimation using MRF priors has proven to be a powerful approach to restoration and reconstruction of high-quality images. Its major drawback, besides its computational load, is the difficulty in systematically selecting a practical and reliable prior distribution. The Gibbs prior parameter λ is also of particular importance since it controls the balance of influence of the Gibbs prior and that of the likelihood. If λ is too small, the prior will tend to have an over-smoothing effect on the solution. Conversely, if it is too large, the MAP estimator may be unstable and it reduces to the maximum likelihood solution as λ goes to infinity. Another difficulty in using a MAP estimator is the non-uniqueness of the solution when the energy function \mathcal{F} is not convex.

3.4 A variational approach to MAP estimation

Unknown prevailing statistics or underlying signal/image/noise models often make a “target” desired performance quantitatively less well defined. Specifically, it may be qualitative in nature (e.g.,

preserve high gradients in a geometric setting, or determine a worst case noise distribution in a statistical estimation setting with a number of interpretations), and may not necessarily be tractably assessed by an objective and optimal performance measure. The formulation of such qualitative goals, is typically carried out by way of adapted functionals which upon being optimized, achieve the stated goal, e.g. a monotonically decreasing functional of gradient modifying a diffusion [61]. This approach is the so-called *variational* approach. It is commonly formulated in a continuous domain which enjoys a large arsenal of analytical tools, and hence offers a greater flexibility. An image is therefore defined as a real-valued function $u : \Omega \rightarrow \mathbb{R}$, and Ω is a nonempty, bounded, open set in \mathbb{R}^2 (usually Ω is a rectangle in \mathbb{R}^2). Throughout, $\mathbf{x} = (x_1, x_2)$ denotes a pixel location in Ω , and $\|\cdot\|$ denotes the L^2 -norm. While the ultimate overall objective in the aforementioned formulation may coincide with that of a probabilistic formulation, namely the recovery of an underlying desired signal u , it is herein often implicit and embedded in an energy functional to be optimized. Generally, the construction of an energy functional is based on some characteristic quantity specified by the task at hand (gradient for segmentation, Laplacian for smoothing, etc.). This energy functional is oftentimes coupled to a regularizing force/energy in order to rule out a great number of solutions and to also avoid any degenerate solution.

When considering the signal model (1), our goal may be succinctly stated as one of estimating the underlying image u based on an observation u_0 and/or any potential knowledge of the noise statistics to further regularize the solution. This yields the following fidelity-constrained optimization problem

$$\begin{aligned} \min_u \quad & \mathcal{F}(u) \\ \text{s.t.} \quad & \|u - u_0\|^2 = \sigma^2 \end{aligned} \tag{4}$$

where \mathcal{F} is a given functional which often defines, as noted above, the particular emphasis on the features of the achievable solution. In other words, we want to find an optimal solution that yields the smallest value of the objective functional among all solutions that satisfy the constraints. Using Lagrange's theorem, the minimizer of (4) is given by

$$\hat{u} = \arg \min_u \left\{ \mathcal{F}(u) + \frac{\lambda}{2} \|u - u_0\|^2 \right\}, \tag{5}$$

where λ is a nonnegative parameter chosen so that the constraint $\|u_0 - u\|^2 = \sigma^2$ is satisfied. In

practice, the parameter λ is often estimated or chosen *a priori*.

Equations (3) and (5) show a close connection between image recovery via MAP estimation and image recovery via optimization of variational integrals. One may in fact reexpress (3) in an integral form similar to that of (5).

A critical issue, however, is the choice of the variational integral \mathcal{F} , which as discussed later, is often driven by geometric arguments. Among the better known functionals (also called *variational integrals*) in image denoising are the Dirichlet and the total variation integrals defined respectively as

$$\mathcal{D}(u) = \frac{1}{2} \int_{\Omega} |\nabla u|^2 dx \quad \text{and} \quad TV(u) = \int_{\Omega} |\nabla u| dx,$$

where ∇u denotes the gradient of the image u . The total variation method basically consists in finding an estimate \hat{u} for the original image u with the smallest total variation among all the images satisfying the noise constraint $\|u - u_0\|^2 = \sigma^2$, where σ is assumed known. Note that the parameter λ controls the trade-off between noise removal and detail preservation.

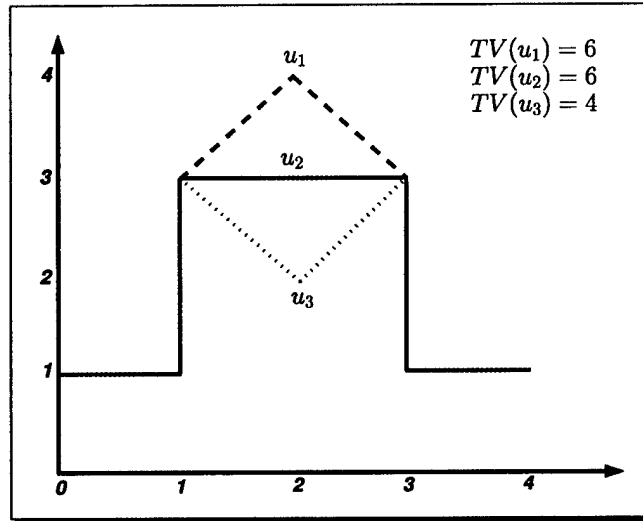


Figure 3.2: Total variation.

The intuition for the use of the total variation integral is that it incorporates the fact that discontinuities are present in the original image u . It measures the jumps of u , even if it is discontinuous as depicted in Figure 3.2 (courtesy of [75]). The total variation method has been used with

success in image denoising, especially for denoising images with piecewise constant features while preserving the location of the edges exactly [23].

The Dirichlet and total variation functionals can be written in a generalized form given by

$$\mathcal{F}(u) = \int_{\Omega} F(|\nabla u|) dx, \quad (6)$$

where $F : \mathbb{R}^+ \rightarrow \mathbb{R}$ is a given smooth function called a *variational integrand* or *Lagrangian* [36].

Using (6), we hence define a functional

$$\begin{aligned} \mathcal{L}(u) &= \mathcal{F}(u) + \frac{\lambda}{2} \|u - u_0\|^2 \\ &= \int_{\Omega} \left(F(|\nabla u|) + \frac{\lambda}{2} |u - u_0|^2 \right) dx, \end{aligned} \quad (7)$$

which by the formulation in (5) becomes

$$\hat{u} = \arg \min_{u \in X} \mathcal{L}(u), \quad (8)$$

where X is an appropriate image space of smooth functions like $C^1(\overline{\Omega})$, or the space $BV(\Omega)$ of image functions with bounded variation, or the Sobolev space $H^1(\Omega) = W^{1,2}(\Omega)$. Note that $BV(\Omega)$ is a Banach space with the norm $\|u\|_{BV} = \|u\|_{L^1(\Omega)} + TV(u)$, while $H^1(\Omega)$ is a Hilbert space with the norm $\|u\|_{H^1(\Omega)}^2 = \|u\|^2 + \|\nabla u\|^2$.

3.4.1 Properties of the optimization problem

A problem is said to be *well-posed* in the sense of Hadamard if (i) a solution of the problem exists, (ii) the solution is unique, (iii) and the solution is stable, i.e. depends continuously on the problem data. It is *ill-posed* when it fails to satisfy at least one of these criteria. To guarantee the well-posedness of our minimization problem (8), the following result provides some conditions.

Proposition 3.1 *Let the image space X be a reflexive Banach space, and let \mathcal{F} be*

(i) weakly lower semicontinuous, i.e. if for any sequence (u^k) in X converging weakly to u , we have $\mathcal{F}(u) \leq \liminf_{k \rightarrow \infty} \mathcal{F}(u^k)$.

(ii) coercive, i.e. $\mathcal{F}(u) \rightarrow \infty$ as $\|u\| \rightarrow \infty$.

Then the functional \mathcal{L} is bounded from below and possesses a minimizer, i.e. there exists $\hat{u} \in X$

such that $\mathcal{L}(\hat{u}) = \inf_X \mathcal{L}$. Moreover, if \mathcal{F} is convex and $\lambda > 0$, then the optimization problem (8) has a unique solution, and therefore it is stable.

Proof: From (i) and (ii) and the weak lower semicontinuity of the L^2 -norm, the functional \mathcal{L} is weak lower semicontinuous, and coercive, i.e. $\mathcal{L}(u) \rightarrow \infty$ as $\|u\| \rightarrow \infty$.

Let u^n be a minimizing sequence of \mathcal{L} , i.e. $\mathcal{L}(u^n) \rightarrow \inf_X \mathcal{L}$. An immediate consequence of the coercivity of \mathcal{L} is that u^n must be bounded. As X is reflexive, thus u^n converges weakly to \hat{u} in X , i.e. $u^n \rightharpoonup \hat{u}$. Thus $\mathcal{L}(\hat{u}) \leq \liminf_{n \rightarrow \infty} \mathcal{L}(u^n) = \inf_X \mathcal{L}$. This proves that $\mathcal{L}(\hat{u}) = \inf_X \mathcal{L}$.

It is easy to check that convexity implies weakly lower semicontinuity. Thus the solution of the optimization problem (8) exists and it is unique because the L^2 -norm is strictly convex. The stability follows using the semicontinuity of \mathcal{L} and the fact that u^n is bounded. ■

3.4.2 Numerical solution: gradient descent flows

To solve the optimization problem (8), a variety of iterative methods such as gradient descent [65], or fixed point method [43, 24] may be applied.

The first-order necessary condition to be satisfied by any minimizer of the functional \mathcal{L} given by (7) is that its first variation $\delta\mathcal{L}(u; v)$ vanishes at u in direction of v , that is

$$\delta\mathcal{L}(u; v) = \left. \frac{d}{d\epsilon} \mathcal{L}(u + \epsilon v) \right|_{\epsilon=0} = 0, \quad (9)$$

and a solution u of (9) is called a *weak extremal* of \mathcal{L} [36].

Using (7) and (9), we obtain the first variation $\delta\mathcal{L}(u; v)$ (see Appendix A for a proof)

$$\begin{aligned} \delta\mathcal{L}(u; v) &= \int_{\Omega} \left\{ \left(\frac{F'(|\nabla u|)}{|\nabla u|} \nabla u \cdot \nabla v \right) + \lambda(u - u_0)v \right\} dx \\ &= - \int_{\Omega} \left\{ \operatorname{div} \left(\frac{F'(|\nabla u|)}{|\nabla u|} \nabla u \right) + \lambda(u - u_0) \right\} v dx, \end{aligned} \quad (10)$$

for all $v \in X$.

Using the fundamental lemma of the calculus of variations, this vanishing first variation yields

an Euler-Lagrange equation as a necessary condition to be satisfied by minimizers of \mathcal{L} . In mathematical terms, the Euler-Lagrange equation is given by

$$-\operatorname{div} \left(\frac{F'(|\nabla u|)}{|\nabla u|} \nabla u \right) + \lambda(u - u_0) = 0, \quad \text{in } \Omega, \quad (11)$$

where “div” stands for the divergence operator. An image u satisfying (11) is called an *extremal* of \mathcal{L} .

Note that $|\nabla u|$ is not differentiable when $\nabla u = 0$ (e.g. flat regions in the image u). To overcome the resulting numerical difficulties, we use the following slight modification

$$|\nabla u|_\epsilon = \sqrt{|\nabla u|^2 + \epsilon},$$

where ϵ is positive sufficiently small.

Proposition 3.2 *Let $\lambda = 0$, and S be a convex set of an image space X . If the Lagrangian F is nonnegative convex and of class C^1 , then every weak extremal of \mathcal{L} is a minimizer of \mathcal{L} on S .*

Proof: The convexity of F yields

$$F(y) \geq F(x) + F'(x)(y - x), \quad \forall x, y \in \mathbb{R}^+. \quad (12)$$

By assumption u is a weak extremal of \mathcal{L} , ie. $\delta\mathcal{L}(u; v) = 0$ for all $v \in S$. This implies that $F'(|\nabla u|) = 0$. Therefore, using (12) we obtain

$$\int_{\Omega} F(|\nabla v|) dx \geq \int_{\Omega} F(|\nabla u|) dx.$$

This concludes the proof. ■

By further constraining λ , we may be in a position to sharpen the properties of the minimizer, as given in the following.

Proposition 3.3 *Let $\lambda = 0$, and S be a convex set of an image space X . If the Lagrangian F is nonnegative convex and of class C^1 such that $F'(0) \geq 0$, then the global minimizer of \mathcal{L} is a constant image.*

Proof: Using (12), it follows that $F(|\nabla u|) \geq F(0)$. Thus the constant image is a minimizer of \mathcal{L} . Since S is convex, it follows that this minimizer is global. ■

Proposition 3.4 *Let $\lambda > 0$, and S be a convex set of image space X . If the Lagrangian F is nonnegative strictly convex and of class C^1 , then an extremal u of \mathcal{L} is the unique minimizer of \mathcal{L} on S .*

Proof: Since $u \mapsto \frac{\lambda}{2}|u - u_0|^2$ is strictly convex when $\lambda > 0$, then the functional $\mathcal{L}(u)$ is strictly convex on S , that is

$$\mathcal{L}(v) > \mathcal{L}(u) + \nabla \mathcal{L}(u) \cdot (v - u).$$

By assumption u is an extremal of \mathcal{L} , thus $\mathcal{L}(v) > \mathcal{L}(u)$, for all $v \neq u$. ■

Using the Euler-Lagrange variational principle, the minimizer of (8) may be interpreted as the steady state solution to the following nonlinear elliptic PDE called *gradient descent flow*

$$u_t = \operatorname{div}(g(|\nabla u|)\nabla u) - \lambda(u - u_0), \quad \text{in } \Omega \times \mathbb{R}_+, \quad (13)$$

where $g(z) = F'(z)/z$, with $z > 0$, and assumed homogeneous Neumann boundary conditions. A numerical implementation of this partial differential equation is discussed in Appendix B.

3.4.3 Illustrative cases

The following examples illustrate the close connection between optimization problems of variational integrals and boundary value problems for partial differential equations in a *no noise* constraint case (i.e. setting $\lambda = 0$):

(a) Heat equation: $u_t = \Delta u$ is the gradient descent flow for the Dirichlet variational integral $\mathcal{D}(u)$.

It is important to point out that the Dirichlet functional tends to smooth out sharp jumps because it controls the second derivative of image intensity i.e. its “spatial acceleration”, and it diffuses the intensity values isotropically. Figure 3.4(b) shows this blurring effect on a clean image depicted in Figure 3.4(a).

- (b) Perona-Malik (PM) equation: It has been shown in [77] that the PM diffusion $u_t = \operatorname{div}(g(|\nabla u|)\nabla u)$ is the gradient descent flow for the variational integral

$$\mathcal{F}_c(u) = \int_{\Omega} F_c(|\nabla u|) d\mathbf{x},$$

with sample Lagrangians $F_c^1(z) = c^2 \log(1 + z^2/c^2)$ or $F_c^2(z) = c^2(1 - \exp(-z^2/c^2))$, where $z \in \mathbb{R}^+$ and c is a tuning positive constant. These Lagrangians are depicted in Figure 3.3.

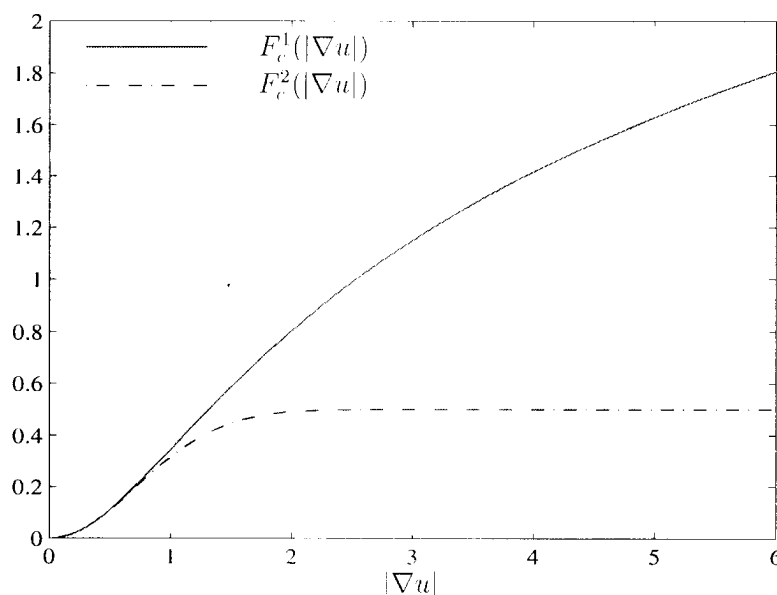


Figure 3.3: Anisotropic Lagrangians.

A minimization of such functionals encourages the smoothing of homogeneous/small gradient regions and the preservation of edges/high gradient regions. Note that ill-posedness of this formulation was addressed in a number of papers (e.g., see [77]). A result of applying the PM flow with F_c^1 to the original image in Figure 3.4(a) is illustrated in Figure 3.4(c). It is worth noting how the diffusion takes place throughout the homogeneous regions and not across the edges.

- (c) Curvature flow: $u_t = \operatorname{div}(\frac{\nabla u}{|\nabla u|})$ corresponds to the total variation integral.

While limiting spurious oscillations, TV optimization preserves sharp jumps as is often encountered in “blocky” signals/images. Figure 3.4(d) illustrates the output of the TV flow.

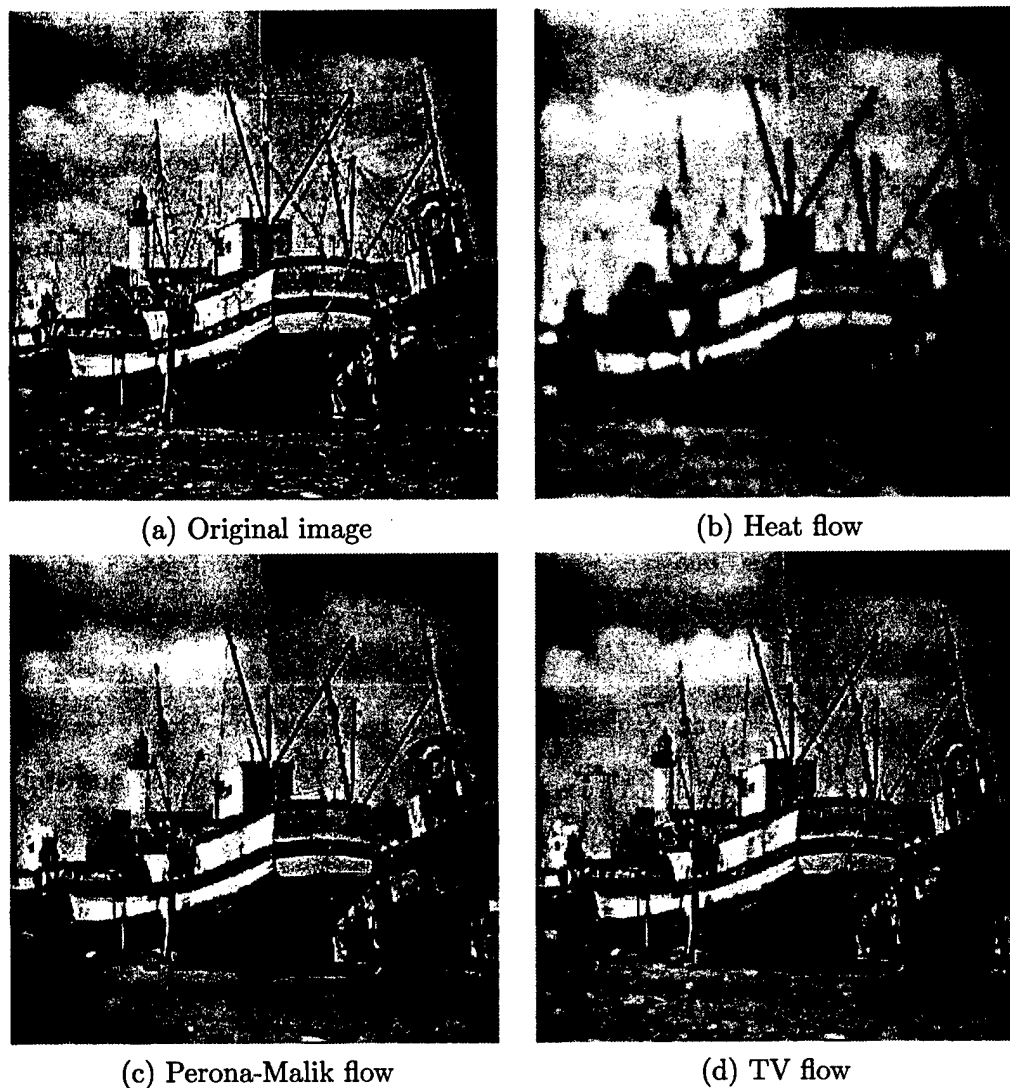


Figure 3.4: Image evolution under (b) the heat flow, (c) Perona-Malik flow, and (d) total variation flow.

3.5 Robust variational approach

3.5.1 Robustness for unknown statistics

In robust estimation, for example, a case where even the noise statistics are *not* precisely known [42, 49] arises. In this case, a reasonable strategy would be to assume that the noise is a member of some set, or of some class of parametric families, and to pick the worst case density (*least favorable*, in some sense) member of that set, and obtain the best signal reconstruction for it. Huber's ϵ -contaminated normal set \mathcal{P}_ϵ is defined as [42]

$$\mathcal{P}_\epsilon = \{(1 - \epsilon)\Phi + \epsilon H : H \in \mathcal{S}\},$$

where Φ is the standard normal distribution, \mathcal{S} is the set of all probability distributions symmetric with respect to the origin and $\epsilon \in [0, 1]$ is the known fraction of "contamination". Huber found that the least favorable distribution in \mathcal{P}_ϵ which maximizes the asymptotic variance (or, equivalently, minimizes the Fisher information) is Gaussian in the center and Laplacian in the tails. The transition between the two depends on the fraction of contamination ϵ , i.e., larger fractions correspond to smaller switching points and vice versa.

For the set \mathcal{P}_ϵ of ϵ -contaminated normal distributions, the least favorable distribution has a density function

$$f_H(z) = ((1 - \epsilon)/\sqrt{2\pi}) \exp(-\rho_k(z)),$$

where ρ_k is the Huber M-estimator cost function (see Figure 3.5) given by

$$\rho_k(z) = \begin{cases} \frac{z^2}{2} & \text{if } |z| \leq k \\ k|z| - \frac{k^2}{2} & \text{otherwise.} \end{cases}$$

Here k is a positive constant determined by the fraction of contamination ϵ by the equation

$$2 \left(\frac{\phi(k)}{k} - \Phi(-k) \right) = \frac{\epsilon}{1 - \epsilon}, \quad (14)$$

where Φ is the standard normal distribution function and ϕ is its probability density function. It is clear that ρ_k is a convex function, quadratic in the center and linear in the tails as illustrated in Figure 3.5.

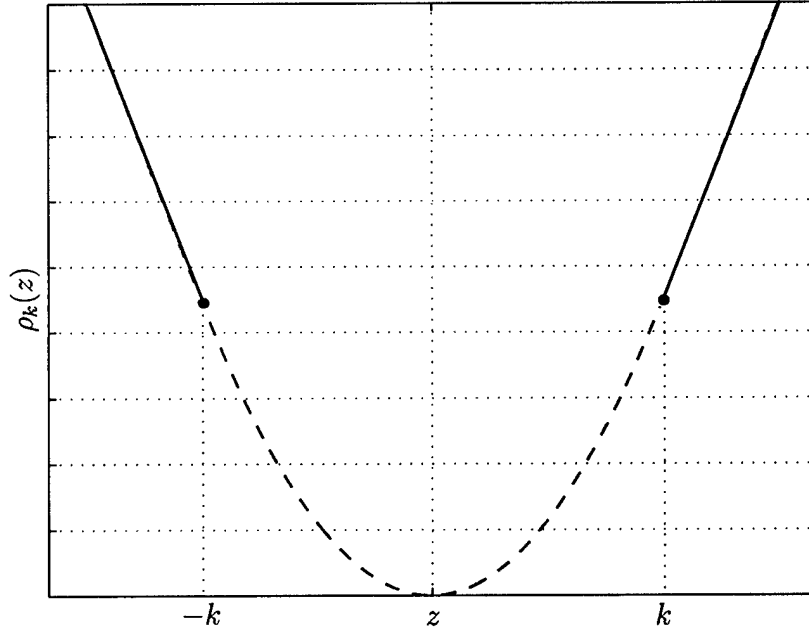


Figure 3.5: Huber function.

Motivated by the robustness of the Huber M-filter in a probabilistic setting and its resilience to impulsive noise, we propose a variational filter which, when accounting for these properties, leads to the following energy functional

$$\mathcal{R}_k(u) = \int_{\Omega} \rho_k(|\nabla u|) dx.$$

Note that the Huber variational integral is a hybrid of the Dirichlet variational integral ($\rho_k(|\nabla u|) \propto |\nabla u|^2/2$ as $k \rightarrow \infty$) and of the total variation integral ($\rho_k(|\nabla u|) \propto |\nabla u|$ as $k \rightarrow 0$). One may check that the Huber variational integral $\mathcal{R}_k : H^1(\Omega) \rightarrow \mathbb{R}^+$ is well defined, convex, and coercive. It follows from Proposition 1 that the minimization problem

$$\hat{u} = \arg \min_{u \in H^1(\Omega)} \left\{ \mathcal{R}_k(u) + \frac{\lambda}{2} \|u - u_0\|^2 \right\} = \arg \min_{u \in H^1(\Omega)} \int_{\Omega} \left(\rho_k(|\nabla u|) + \frac{\lambda}{2} |u - u_0|^2 \right) dx \quad (15)$$

has a solution. This solution is unique when $\lambda > 0$.

Proposition 3.5 *The optimization problem (15) is equivalent to*

$$\hat{u} = \arg \min_{(u, \theta) \in H^1(\Omega) \times \mathbb{R}} \left\{ \frac{\theta^2}{2} + \int_{\Omega} \left(k \left| |\nabla u| - \theta \right| + \frac{\lambda}{2} |u - u_0|^2 \right) dx \right\}. \quad (16)$$

Proof: For z fixed, define $\Psi(\theta) = \frac{1}{2}\theta^2 + k|z - \theta|$ on \mathbb{R} . It is clear that Ψ is convex on \mathbb{R} . It follows that Ψ attains its minimum at θ_0 such that $\Psi'(\theta_0) = 0$ and $\Psi''(\theta_0) > 0$, that is $\theta_0 = k \operatorname{sign}(z - k)$. Thus we have

$$\Psi(\theta_0) = \begin{cases} kz - \frac{k^2}{2} & \text{if } z > k \\ \frac{z^2}{2} & \text{if } z = k \\ -kz - \frac{k^2}{2} & \text{if } z < -k, \end{cases}$$

and therefore $\rho_k(z) = \arg \min_{\theta \in \mathbb{R}} \Psi(\theta)$. This concludes the proof. \blacksquare

Using the Euler-Lagrange variational principle, a Huber gradient descent flow is obtained as

$$u_t = \operatorname{div}(g_k(|\nabla u|)\nabla u) - \lambda(u - u_0), \quad \text{in } \Omega \times \mathbb{R}_+, \quad (17)$$

where g_k is the Huber M-estimator weight function

$$g_k(z) = \frac{\rho'_k(z)}{z} = \begin{cases} 1 & \text{if } |z| \leq k \\ \frac{k}{|z|} & \text{otherwise.} \end{cases}$$

For large k , this flow yields an isotropic diffusion (heat equation when $\lambda = 0$), and for small k , it corresponds to total variation gradient descent flow (curvature flow when $\lambda = 0$).

It is worth pointing out that in the case of no noise constraint (i.e. setting $\lambda = 0$), the Huber gradient descent flow yields a robust anisotropic diffusion [20] obtained by replacing the diffusion functions proposed in [61] with robust M-estimator weight functions [42].

Recently, we proposed a smooth Huber variational integral [18] given by

$$\Phi(u) = \int_{\Omega} \varphi(|\nabla u|) dx,$$

where the Lagrangian φ is defined as

$$\varphi(t) = \begin{cases} -ct & \text{if } t \leq -a \\ (t+a)^3/3 - ct & \text{if } -a < t < -b \\ (t^2 - b^2)/2 + ((a-b)^3 + 3bc)/3 & \text{if } -b \leq t \leq b \\ -(t-a)^3/3 + ct & \text{if } b < t < a \\ ct & \text{otherwise.} \end{cases}$$

with $a = 3/2$, $b = 1$, and $c = 5/4$. Its derivative φ' (also referred to as influence function in robust statistics) is depicted in Figure 3.6. The Huber influence function, however, is not differentiable as shown in Figure 3.6. The differentiability of the influence function is of great importance since it implies the continuity of its first derivative which in turn implies the continuity of the confidence intervals in the data points. A more detailed description of the smooth Huber gradient descent flow will be reported elsewhere.

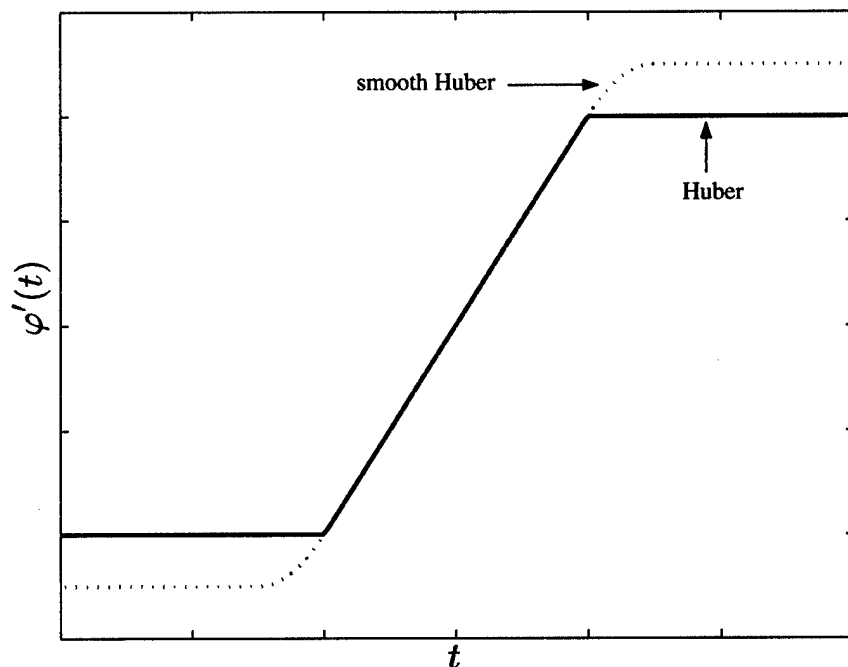


Figure 3.6: Huber influence function and its smooth version.

3.5.2 Perona-Malik equation: an estimation-theoretic perspective

In a similar spirit as above, one may proceed to justify the Perona-Malik equation from a specific statistical model. Assuming an image $u = (u_{ij})$ as a random matrix with i.i.d. elements, the output of the Log-Cauchy filter [17] is defined as a solution to the maximum log-likelihood estimation problem for a Cauchy distribution with dispersion c and estimation parameter θ . In other words,

the output of a Log-Cauchy filter is the solution to the following robust estimation problem [17]

$$\min_{\theta} \sum_{i,j} \log(c^2 + (u_{ij} - \theta)^2) = \min_{\theta} \sum_{i,j} F_c(u_{ij} - \theta),$$

where the cost function F_c coincides with the Lagrangian function which yields the Perona-Malik equation. Hence, in the probabilistic setting the Perona-Malik flow corresponds to the Log-Cauchy filter. Figure 3.7 illustrates the performance of the Log-Cauchy filter in removing heavy-tailed (impulsive) noise.

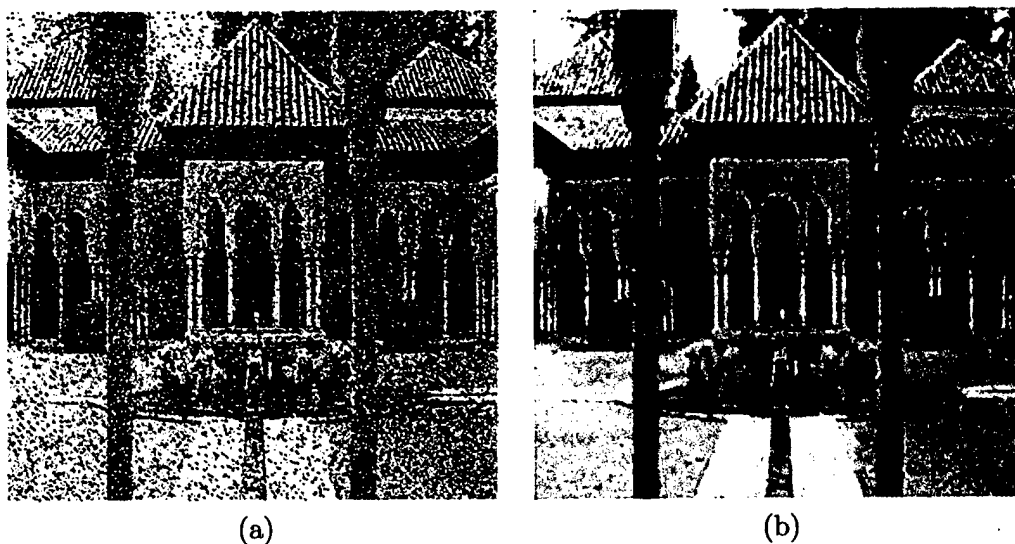


Figure 3.7: Log-Cauchy filtering: (a) contaminated image with impulsive noise, (b) filtered image.

3.6 Information based functionals

3.6.1 Information theoretic approach

In the previous section, we proposed a *least favorable* distribution as a result of exercising *our ignorance* in describing that of an image gradient within a domain. Another effective way is to adopt a criterion which bounds such a case, namely that of *entropy* [32]. The maximum entropy criterion is indeed an important principle in statistics for modeling the prior probability $p(u)$ of a

process u , and has been used with success in numerous image processing applications. The term is often associated with qualifying the selection of a distribution subject to some moments constraints (e.g. mean, variance, etc.), that is, the available information is described by way of moments of some known functions $m_r(u)$ with $r = 1, \dots, s$. Indeed coupling the finiteness of $m_r(u)$ for example with the maximum entropy condition of the data suggests a *most random* model $p(u)$ with the corresponding moments constraints as a most adapted model (equivalently minimizing negentropy see e.g. [48]).

$$\begin{aligned} \min_u \quad & \int p(u) \log p(u) du \\ \text{s.t.} \quad & \int p(u) du = 1 \\ & \int m_r(u) p(u) du = \mu_r, \quad r = 1, \dots, s \end{aligned} \quad (18)$$

Using Lagrange's theorem, the solution of (18) is given by

$$p(u) = \frac{1}{Z} \exp \left\{ - \sum_{r=1}^s \lambda_r m_r(u) \right\}, \quad (19)$$

where λ_r 's are the Lagrange multipliers, and Z is a partition function. The resulting model $p(u)$ given by (19) may hence be used as a prior in a MAP estimation formulation.

3.6.2 Entropic gradient descent flow

Motivated by the good performance of the maximum entropy principle in image/signal analysis applications and inspired by its rationale, we may naturally adapt it to describe the distribution of a gradient throughout an image. Specifically, the large gradients should coincide with tail events of this distribution, while the small and medium ones representing the smooth regions, form the mass of the distribution. Towards that end, we write

$$\mathcal{H}(u) = \int_{\Omega} H(|\nabla u|) dx = \int_{\Omega} |\nabla u| \log |\nabla u| dx.$$

where $H(z) = z \log(z)$, $z \geq 0$. Note that $-H(z) \rightarrow 0$ as $z \rightarrow 0$.

It follows from the inequality $z \log(z) \leq z^2/2$ that

$$|\mathcal{H}(u)| \leq \int_{\Omega} |\nabla u|^2 dx \leq \|u\|_{H^1(\Omega)}^2 < \infty, \quad \forall u \in H^1(\Omega),$$

where $\|\cdot\|_{H^1(\Omega)}$ denotes the H^1 -norm. Thus the negentropy variational integral $\mathcal{H} : H^1(\Omega) \rightarrow \mathbb{R}$ is well defined. Note also that the inequality $z \log(z) \leq z^2/2$ implies $\mathcal{H}(u) \leq \mathcal{D}(u)$, where $\mathcal{D}(u)$ is the Dirichlet integral. One may check that the Lagrangian H is strictly convex, and coercive, i.e. $H(z) \rightarrow \infty$ as $|z| \rightarrow \infty$. The following result follows from Proposition 1.

Proposition 3.6 *Let $\lambda > 0$. The minimization problem*

$$\hat{u} = \arg \min_{u \in H^1(\Omega)} \left\{ \mathcal{H}(u) + \frac{\lambda}{2} \|u - u_0\|^2 \right\} = \arg \min_{u \in H^1(\Omega)} \int_{\Omega} \left(|\nabla u| \log |\nabla u| + \frac{\lambda}{2} |u - u_0|^2 \right) dx$$

has a unique solution provided that $|\nabla u| \geq 1$.

Calling upon the Euler-Lagrange variational principle again, the following entropic gradient descent flow results

$$u_t = \operatorname{div} \left(\frac{1 + \log |\nabla u|}{|\nabla u|} \nabla u \right) - \lambda(u - u_0), \quad \text{in } \Omega \times \mathbb{R}_+,$$

with homogeneous Neumann boundary conditions. In addition, this energy spread of the gradient energy may be related to that sought by the total variation method, which in contrast allows for additional higher gradients.

Proposition 3.7 *Let u be an image. The negentropy variational integral and the total variation satisfy the following inequality*

$$\mathcal{H}(u) \geq TV(u) - 1.$$

Proof: Since the negentropy H is a convex function, the Jensen inequality yields

$$\begin{aligned} \int_{\Omega} H(|\nabla u|) dx &\geq H \left(\int_{\Omega} |\nabla u| dx \right) \\ &= H(TV(u)) \\ &= TV(u) \log TV(u), \end{aligned}$$

and using the inequality $z \log(z) \geq z - 1$ for $z \geq 0$, we conclude the proof. ■

Remark: (See Figure 3.8) The following inequalities between Huber variational integral, total variation and negentropy integral hold

- (i) If $|\nabla u| \in [0, e]$ then $\mathcal{H}(u) \leq TV(u)$
- (ii) If $|\nabla u| \in (e, \infty)$ then $\mathcal{H}(u) > TV(u)$
- (iii) If $|\nabla u| \in (e^{k-1}, \infty)$ and $k \geq 2$ then $\mathcal{H}(u) \leq \mathcal{R}_k(u)$,

where e is the Euler number ($e = \lim_{n \rightarrow \infty} (1 + 1/n)^n \approx 2.71$).

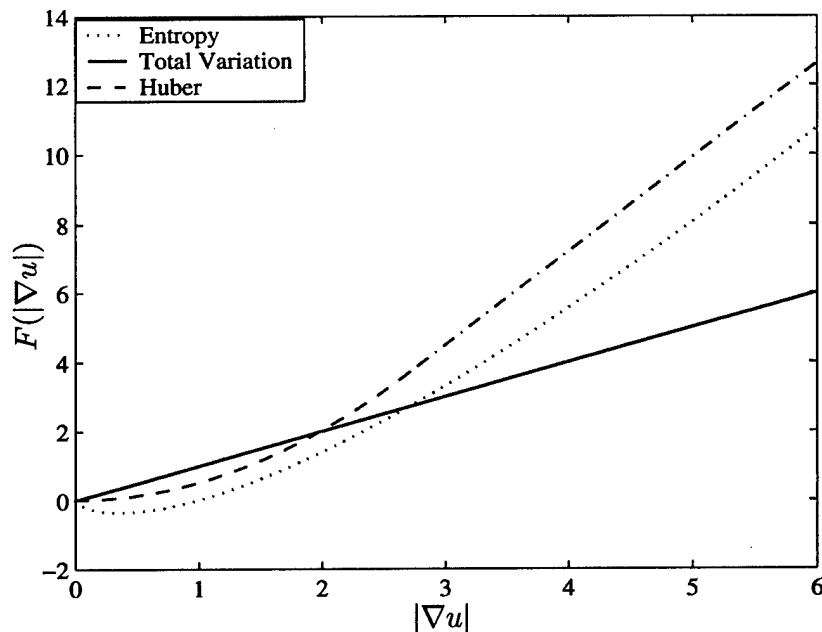


Figure 3.8: Visual comparison of some variational integrands

3.6.3 Improved entropic gradient descent flow

To summarize and for a comparison sake, we show in Figure 3.8 the behavior of the variational integrands we have discussed in this paper. It can be readily shown [6] that a differentiable hybrid functional between the negentropy variational integral and the total variation may be defined as

$$\mathcal{H}_{TV}(u) = \begin{cases} \mathcal{H}(u) & \text{if } |\nabla u| \leq e \\ 2 TV(u) - \text{meas}(\Omega)e & \text{otherwise,} \end{cases}$$

yielding an improved gradient descent flow. The quantity $\text{meas}(\Omega)$ denotes the Lebesgue measure of the image domain Ω . Note that $\mathcal{H}_{TV} : H^1(\Omega) \rightarrow \mathbb{R}$ is well defined, differentiable, convex, and

coercive. It follows from Proposition 1 that the minimization problem

$$\hat{u} = \arg \min_{u \in H^1(\Omega)} \left\{ \mathcal{H}_{TV}(u) + \frac{\lambda}{2} \|u - u_0\|^2 \right\} \quad (20)$$

has a unique solution provided that $\lambda > 0$.

Figure 3.9 depicts the improved entropic Lagrangian $H_{TV} : \mathbb{R}^+ \rightarrow \mathbb{R}$ defined as

$$H_{TV}(z) = \begin{cases} z \log(z) & \text{if } z \leq e \\ 2z - e & \text{o.w.} \end{cases}$$

Using the Euler-Lagrange variational principle, it follows that the improved entropic gradient descent flow is given by

$$u_t = \nabla \cdot \left(\frac{H'_{TV}(|\nabla u|)}{|\nabla u|} \nabla u \right) - \lambda(u - u_0), \quad \text{in } \Omega \times \mathbb{R}_+, \quad (21)$$

with homogeneous Neumann boundary conditions.

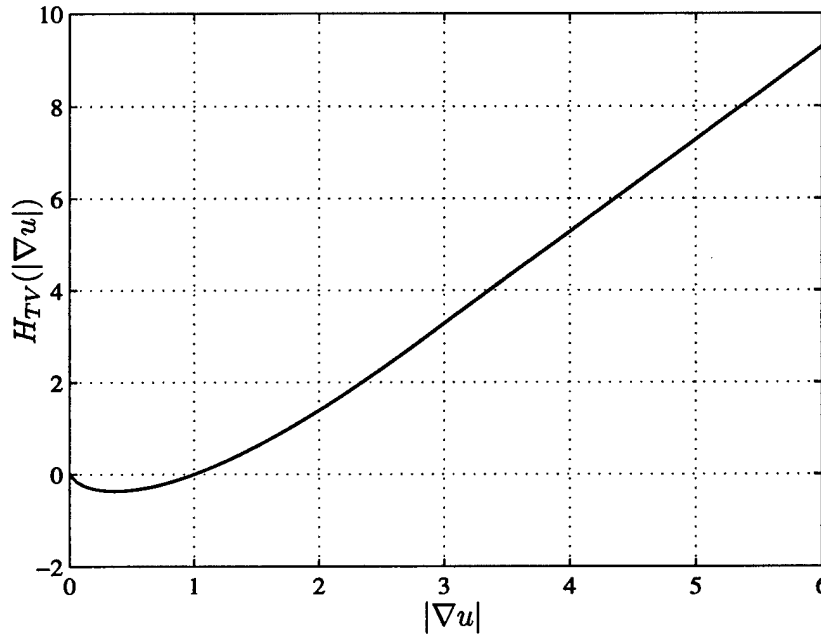


Figure 3.9: Improved entropic Lagrangian.

3.7 Experimental results

This section presents simulation results where Huber, entropic, total variation and improved entropic gradient descent flows are applied to enhance images corrupted by Gaussian and Laplacian noise.

The performance of a filter clearly depends on the filter type, the properties of signals/images, and the characteristics of the noise. The choice of criteria by which to measure the performance of a filter presents certain difficulties, and only gives a partial picture of reality. To assess the performance of the proposed denoising methods, a mean square error (MSE) between the filtered and the original image is evaluated and used as a quantitative measure of performance of the proposed techniques. The regularization parameter (or Lagrange multiplier) λ for the proposed gradient descent flows is chosen to be proportional to signal-to-noise ratio (SNR) in all the experiments.

In order to evaluate the performance of the proposed gradient descent flows in the presence of Gaussian noise, the image shown in Figure 3.10(a) has been corrupted by Gaussian white noise with $\text{SNR} = 4.79$ db. Figure 3.10 displays the results of filtering the noisy image shown in Figure 3.10(b) by Huber with optimal $k = 1.345$, entropic, total variation and improved entropic gradient descent flows. Qualitatively, we observe that the proposed techniques are able to suppress Gaussian noise while preserving important features in the image. The resulting mean square error (MSE) computations are depicted in Table 3.1.

The Laplacian noise is somewhat heavier than the Gaussian noise. Moreover, the Laplace distribution is similar to Huber's least favorable distribution [42] at least in the tails. To demonstrate the application of the proposed gradient descent flows to image denoising, qualitative and quantitative comparisons are performed to show a much improved performance of these techniques. Figure 3.11(b) shows a noisy image contaminated by Laplacian white noise with $\text{SNR} = 3.91$ db. The MSE's results obtained by applying the proposed techniques to the noisy image are shown in Table 3.2. Note that from Figure 3.11 it is clear that the improved entropic gradient descent flow outperforms the other flows in removing Laplacian noise. Comparison of these images clearly indicates that the improved entropic gradient descent flow preserves well the image structures while removing heavy tailed noise.

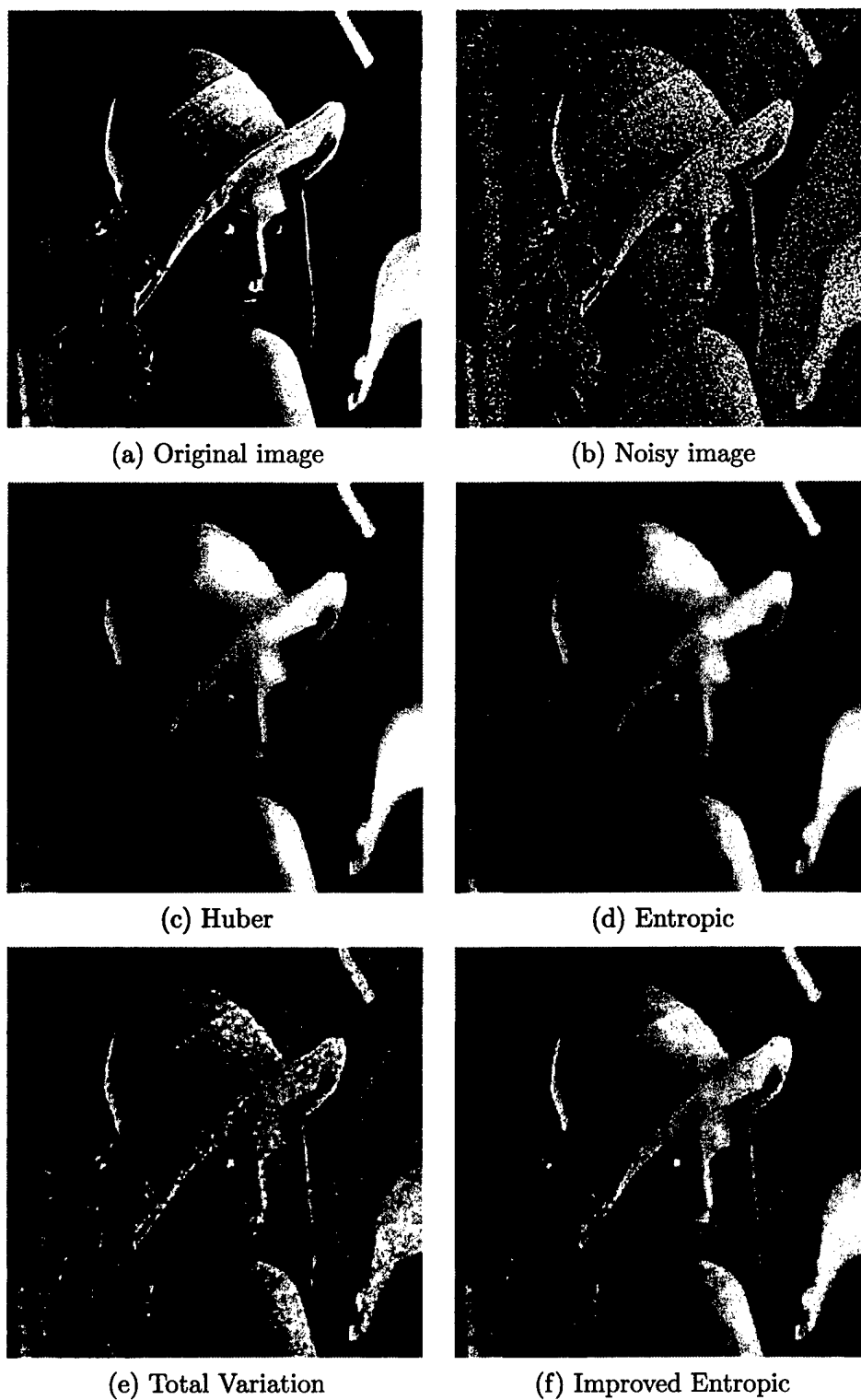


Figure 3.10: Filtering results for Gaussian noise.

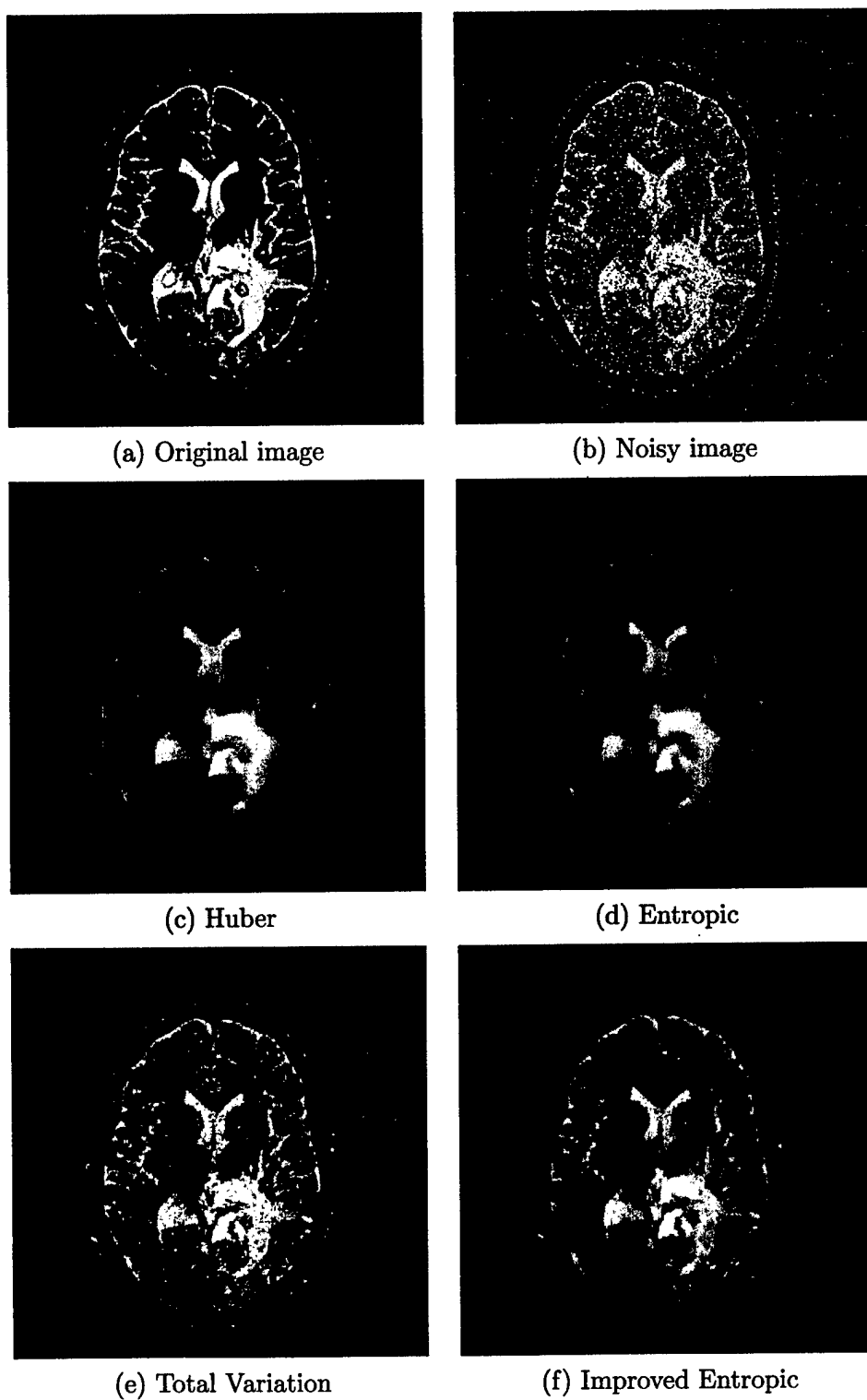


Figure 3.11: Filtering results for Laplacian noise.

| PDE | Mean Square Error (MSE) | | |
|-------------------|-------------------------|-----------------|-----------------|
| | SNR = 4.79 | SNR = 3.52 | SNR = 2.34 |
| Huber | 234.1499 | 233.7337 | 230.0263 |
| Entropic | 205.0146 | 207.1040 | 205.3454 |
| Total Variation | 247.4875 | 263.0437 | 402.0660 |
| Improved Entropic | 121.2550 | 137.9356 | 166.4490 |

Table 3.1: MSE's computations for Gaussian noise.

| PDE | Mean Square Error (MSE) | | |
|-------------------|-------------------------|-----------------|-----------------|
| | SNR = 6.33 | SNR = 3.91 | SNR = 3.05 |
| Huber | 237.7012 | 244.4348 | 248.4833 |
| Entropic | 200.5266 | 211.4027 | 217.3592 |
| Total Variation | 138.4717 | 176.1719 | 213.1221 |
| Improved Entropic | 104.4591 | 170.2140 | 208.8639 |

Table 3.2: MSE's computations for Laplacian noise

3.8 Discussions and conclusions

In this chapter, we have explored a connection between maximum *a posteriori* estimation and the variational formulation based on the minimization of a given variational integral subject to some noise constraints. A robust filter called *Huber gradient descent flow* was proposed. It minimizes the Huber variational integral subject to some noise constraints. This filter behaves as the total variation anisotropic diffusion for small gradient magnitudes and as the isotropic diffusion for large gradient magnitudes. Another filter called *entropic gradient descent flow* derived from the maximum entropy principle is proposed. It minimizes the negentropy variational integral subject to some noise constraints. The proposed gradient descent flows has been applied to enhance images corrupted with Gaussian as well as Laplacian noise, and it has been shown that these proposed techniques preserve well details while removing noise.

Topological Variational Model for Image Singularities

In this Chapter, we propose a geometric/topological variational model to preserve degenerate image singularities [16]. Such singularities carry important information for a variety of image processing and computer vision operations, such as image registration, shape analysis, and object recognition. The approach is expressed in a higher order variational framework, and it is a result of minimizing a variational integral defined in terms of the gradient and the Hessian matrix of the height function defined on a manifold.

4.1 Introduction

Over the last decade, there has been a flurry of activity in applying nonlinear partial differential equations (PDEs) to image processing and computer vision. These approaches have been proposed to address the limitations of linear scale-space and to tackle a variety of imaging applications. Many of these PDE-based techniques are solutions to variational problems [56, 7, 8], and are determined by geometric quantities. Such evolution equations have blossomed in recent years, with striking applications to image denoising, image segmentation, curve evolution, and motion estimation. One of the most important property to be investigated through these geometric flows is the local behavior of image singularities, and hence the topology of the level sets of the image. Depending on whether the Hessian matrix of the image is singular or not, the critical points may

be divided into two classes: degenerate and nondegenerate respectively [31]. The so-called Morse theory [3] studies the properties of a Morse function (i.e. a function that has only nondegenerate singular points) and it describes the topology changes of the level sets of this function at those singularities. Regular or noncritical points do not affect the number or genus of the components of the level sets. It can be shown that Morse functions are dense and stable in the set of all smooth functions, that is the structure of nondegenerate singularities does not change under small perturbations. The basic ingredients of Morse theory are *Morse lemma* and *deformation lemma*. The former states that in a neighborhood of a nondegenerate singularity, a function is reduced to a quadratic form in an appropriate system of coordinates, while the latter lemma essentially states that two level sets of a Morse function are topologically equivalent and can be deformed onto one another if there is no singularity between them.

On the other hand, degenerate singularities are unstable, and their local behavior can be studied using catastrophe theory [22] which deals with such critical points. The essential characteristics of non-Morse function can be studied by embedding it into a smooth family of functions controlled by a certain parameter. This parameterized function can be regarded as a perturbed function, and topological changes may happen when changing the control parameter in such a way that a degenerate singularity may become nondegenerate. The idea behind this perturbation method is to show how degenerate singularities behave as the control parameter changes and therefore to reduce the general problem to the nondegenerate situation so that Morse theory can be applied. If we think of the control parameter as time, then geometric evolution equations can be regarded as such a smooth family of functions. These equations are flows resulting from geometrical variational problems, and are determined by geometric quantities.

Geometry deals with shape, size and location of geometric elements, while topology is the connectivity of the geometric elements. In other words, the geometry of an object is its representation in space, while the topology is the interconnection of some geometrical objects. Furthermore, topology is a global property of a space and does not depend on local geometrical structure.

This Chapter is outlined as follows: the next section is concerned with the problem formulation,

followed by a geometric approach to image singularities. Section 4.3 describes a topological characterization of singularities in the Morse theory framework. Furthermore, using the concepts of height function and Gauss map, we show that almost all images are Morse functions. We also prove that images defined on the same domain are topologically equivalent. In Section 4.4, a topological variational approach for image singularities is proposed. Section 4.5 is devoted to experimental results showing the methodology proposed in this Chapter. Finally section 4.6 presents some conclusions.

4.2 Problem formulation

Let $u : \Omega \subset \mathbb{R}^2 \rightarrow \mathbb{R}$ be an image, where Ω is an open bounded subset of \mathbb{R}^2 with Lipschitz boundary (usually Ω is a rectangle).

4.2.1 Geometric analysis of images

To apply and benefit from the tools of geometry in image analysis, it is convenient to consider the graph of an image u which is a surface (2-dimensional manifold) $\mathcal{U} \subseteq \mathbb{R}^3$ defined as $\mathcal{U} = \{(x, y, z) : z = u(x, y)\}$ where $z = u(x, y)$ is the gray level at position (x, y) on the image domain Ω .

In order to allow partial differentiation and consequently all the features of differential calculus on \mathcal{U} , we need to consider a smooth image u , that is has continuous partial derivatives of all orders, so that the manifold \mathcal{U} is differentiable. Thus the study of this differential manifold involves topology, since differentiability implies continuity. A common way to smooth an image u is to embed it into a family of images known as *scale-space image*. For example, a Gaussian scale-space image which is the result of convolving an image with the bivariate Gaussian density. A parametric representation of \mathcal{U} is the Monge patch defined by $\mathbf{r} : \Omega \rightarrow \mathcal{U}$ such that $\mathbf{r}(x, y) = (x, y, u(x, y))$. Note that the patch \mathbf{r} covers all \mathcal{U} , that is, $\mathbf{r}(\Omega) = \mathcal{U}$, and it is regular, that is, $\mathbf{r}_x \times \mathbf{r}_y \neq 0$ or equivalently, the Jacobian matrix of \mathbf{r} has rank 2.

It is worth pointing out that the Monge patch $\mathbf{r} : \Omega \rightarrow \mathcal{U}$ of a smooth image $u : \Omega \rightarrow \mathbb{R}$ is a diffeomorphism because it is a smooth bijection, and its inverse \mathbf{r}^{-1} is the restriction to \mathcal{U} of the smooth projection $\pi : \Omega \times \mathbb{R} \rightarrow \Omega$, that is $\mathbf{r}^{-1} = \pi|_{\mathcal{U}}$.

Let $\mathbf{p} \in \mathcal{U}$, then there exists $(x, y) \in \Omega$ such that $\mathbf{p} = \mathbf{r}(x, y)$. Hence, the unit normal \mathcal{N} to \mathcal{U} is given by

$$\mathcal{N}(\mathbf{p}) = \mathcal{N}(\mathbf{r}(x, y)) = \frac{\mathbf{r}_x \times \mathbf{r}_y}{\|\mathbf{r}_x \times \mathbf{r}_y\|} = \frac{(-u_x, -u_y, 1)}{\sqrt{1 + u_x^2 + u_y^2}}. \quad (1)$$

Since \mathbf{r} is regular, it follows that the unit normal is well-defined everywhere, and therefore the image graph \mathcal{U} is orientable. The unit normal can be viewed as a mapping $\mathbf{g} : \Omega \rightarrow S^2(1)$, called *Gauss map* of \mathbf{r} and defined as $\mathbf{g}(x, y) = \mathcal{N}(\mathbf{r}(x, y))$, where $S^2(1) = \{\mathbf{p} \in \mathbb{R}^3 : \|\mathbf{p}\| = 1\}$ is the unit sphere.

4.2.2 Image singularities

Let $f : \mathbb{M} \rightarrow \mathbb{R}$ be a real-valued function defined on a smooth manifold $\mathbb{M} \subset \mathbb{R}^3$. The function f is smooth if the function $f \circ \mathbf{r} : \Omega \rightarrow \mathbb{R}$ is smooth (in the ordinary Euclidean sense), where \mathbf{r} is a smooth regular patch that covers all \mathbb{M} , that is, $\mathbf{r}(\Omega) = \mathbb{M}$. A point \mathbf{p}_0 on \mathbb{M} is a singularity or critical point of f if $\mathbf{p}_0 = \mathbf{r}(x_0, y_0)$, for some $(x_0, y_0) \in \Omega$, and the gradient of $f \circ \mathbf{r}$ at (x_0, y_0) vanishes, i.e. $\nabla(f \circ \mathbf{r}(x_0, y_0)) = 0$.

A singularity \mathbf{p}_0 is nondegenerate if the Hessian matrix $\nabla^2(f \circ \mathbf{r}(x_0, y_0))$ is nonsingular. Otherwise this singularity \mathbf{p}_0 is degenerate. The nature of the Hessian matrix is directly related to the stability of the singularity. Hence, critical points can be divided into two classes: degenerate and nondegenerate. The main theory about nondegenerate singularities is Morse theory that classifies all such points. The degenerate singularities are more difficult to handle and catastrophe theory deals with such points.

4.2.3 Image singularities: a geometric approach

A geometric characterization of image singularities is described by curvatures of the image graph. For a smooth image u , the Hessian matrix $\nabla^2 u$ provides information about the type of singularities, and also characterizes the shape of the image graph using the first and second fundamental forms

that can be formulated respectively as follows [29]

$$\mathbf{I} = \begin{pmatrix} e & f \\ f & g \end{pmatrix} = \begin{pmatrix} \mathbf{r}_x \cdot \mathbf{r}_x & \mathbf{r}_x \cdot \mathbf{r}_y \\ \mathbf{r}_y \cdot \mathbf{r}_x & \mathbf{r}_y \cdot \mathbf{r}_y \end{pmatrix} = \begin{pmatrix} 1 + u_x^2 & u_x u_y \\ u_x u_y & 1 + u_y^2 \end{pmatrix}$$

and

$$\mathbf{II} = \begin{pmatrix} \ell & m \\ m & n \end{pmatrix} = \begin{pmatrix} \mathbf{N} \cdot \mathbf{r}_{xx} & \mathbf{N} \cdot \mathbf{r}_{xy} \\ \mathbf{N} \cdot \mathbf{r}_{yx} & \mathbf{N} \cdot \mathbf{r}_{yy} \end{pmatrix} = \frac{1}{\sqrt{1 + \|\nabla u\|^2}} \begin{pmatrix} u_{xx} & u_{xy} \\ u_{xy} & u_{yy} \end{pmatrix} = \frac{\nabla^2 u}{\sqrt{1 + \|\nabla u\|^2}}$$

Note that $\det(\mathbf{I}) = 1 + u_x^2 + u_y^2 \neq 0$, and therefore the matrix \mathbf{I} is nonsingular.

The matrix $\mathbf{S} := \mathbf{I}^{-1}\mathbf{II}$ is called the matrix of the shape operator and is given by

$$\mathbf{S} = \begin{pmatrix} s_{11} & s_{12} \\ s_{21} & s_{22} \end{pmatrix} = \frac{1}{eg - f^2} \begin{pmatrix} g\ell - fm & gm - fn \\ em - f\ell & en - fm \end{pmatrix}$$

The most important curvatures in surface theory are Gaussian and mean curvatures given respectively by

$$K = \det(\mathbf{S}) = \frac{\ell n - m^2}{eg - f^2} = \frac{\det(\nabla^2 u)}{(1 + \|\nabla u\|^2)^2} = \kappa_1 \kappa_2,$$

and

$$H = \frac{1}{2} \text{Tr}(\mathbf{S}) = \frac{2fm - en - g\ell}{eg - f^2} = \frac{1}{2} \nabla \cdot \left(\frac{\nabla u}{\sqrt{1 + \|\nabla u\|^2}} \right) = \frac{\kappa_1 + \kappa_2}{2}.$$

where κ_1 and κ_2 are the principal curvatures (eigenvalues of the matrix \mathbf{S}), that is

$$\kappa_1 = H - \sqrt{H^2 - K} = \text{Tr}(\mathbf{S})/2 - \sqrt{(\text{Tr}(\mathbf{S})/2)^2 - \det(\mathbf{S})}$$

and

$$\kappa_2 = H + \sqrt{H^2 - K} = \text{Tr}(\mathbf{S})/2 + \sqrt{(\text{Tr}(\mathbf{S})/2)^2 - \det(\mathbf{S})}.$$

The corresponding eigenvectors \mathbf{e}_1 and \mathbf{e}_2 (i.e. $\mathbf{S}\mathbf{e}_1 = \kappa_1\mathbf{e}_1$ and $\mathbf{S}\mathbf{e}_2 = \kappa_2\mathbf{e}_2$) are called the principal directions, and are given by $\mathbf{e}_1 = (\kappa_1 - s_{22}, s_{21})$ and $\mathbf{e}_2 = (\kappa_2 - s_{22}, s_{21})$. These principal curvatures control the shape of the surface near an arbitrary point \mathbf{p} as illustrated in Table 4.1. Note that the principal directions may not be unique. The signs of the principal curvatures can be used to classify the local structure of the image graph.


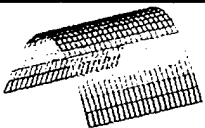

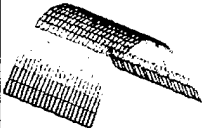

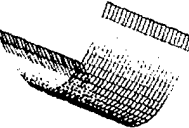

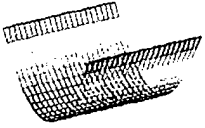

| $\kappa_1 \backslash \kappa_2$ | < 0 | $= 0$ | > 0 |
|--------------------------------|---|---|--|
| < 0 |  |  |  |
| $= 0$ |  |  |  |
| > 0 |  |  |  |

Table 4.1: Local shape of a surface.

A point $p \in \mathbb{M}$ where both principal curvatures are equal is called *umbilic*. Assume that $\kappa_1 < \kappa_2$, that is, κ_1 and κ_2 are the minimal and maximal principal curvatures with associated principal directions e_1 and e_2 respectively.

Definition 4.1 A point $p \in \mathbb{M}$ is called a *ridge point* if κ_2 attains a local positive maximum in the direction of e_2 , i.e.

$$\kappa_2(p) > 0, \quad \nabla \kappa_2(p) \cdot e_2 = 0 \quad \text{and} \quad e_2 \cdot \nabla^2 \kappa_2(p) e_2 < 0.$$

The point $p \in \mathbb{M}$ is called a *ravine point* if κ_1 attains a local negative minimum in the direction of e_1 , i.e.

$$\kappa_1(p) < 0, \quad \nabla \kappa_1(p) \cdot e_1 = 0 \quad \text{and} \quad e_1 \cdot \nabla^2 \kappa_1(p) e_1 > 0.$$

4.3 Topological analysis of images

The purpose of Morse theory is to explain the presence and the stability of critical points in terms of the topology of the underlying smooth manifold. Topology is the property that determines which

parts of the shape of objects are connected to which other parts, while geometry determines where, in a given coordinate system, each part is located. The basic principle is that the topology of a manifold is very closely related to the critical points of a smooth function on that manifold. Morse theory studies the questions, what a manifold knows about the critical points of a Morse function, and what the Morse function knows about the manifold.

4.3.1 Image singularities: a topological perspective

A typical problem in mathematics involves attempting to understand the topology, or large-scale structure, of an object with limited information. This kind of problem also occurs in mathematical physics, dynamic systems and mechanical engineering. Morse theory, when applied to smooth manifolds such as a sphere or an image graph, provides a general tool of attacking this problem. Morse proved a major result that generalizes the straightforward result that the lowest-order nonvanishing term in the Taylor series describes the local behavior of a smooth function of single variable to functions of many variables.

Definition 4.2 *A smooth function $f : \mathbb{M} \rightarrow \mathbb{R}$ on a smooth manifold \mathbb{M} is called a Morse function if all its singularities are nondegenerate.*

Nondegenerate singularities are isolated, that is, there cannot be a sequence of nondegenerate singularities converging to a nondegenerate singularity \mathbf{p} . In other words, there is no other point in the neighborhood of \mathbf{p} that is singular. This fact follows from the following Morse's lemma.

Lemma 4.3 *If $f : \mathbb{M} \rightarrow \mathbb{R}$ has a nondegenerate singularity at $\mathbf{p}_0 \in \mathbb{M}$, then there exists $(x_0, y_0) \in \Omega$ such that $\mathbf{p}_0 = \mathbf{r}(x_0, y_0)$, and f has the following representation*

$$f(\mathbf{p}) = f \circ \mathbf{r}(x_0, y_0) \pm x^2 \pm y^2 = f(\mathbf{p}_0) \pm x^2 \pm y^2,$$

for all $\mathbf{p} = \mathbf{r}(x, y) \in \mathbb{M}$, where \mathbf{r} is a regular smooth path.

Note that the only nondegenerate singularities are the minimum, maximum and saddle points as depicted in Figure 4.1. On the other hand, Figure 4.2 illustrates a degenerate singularity (cusp

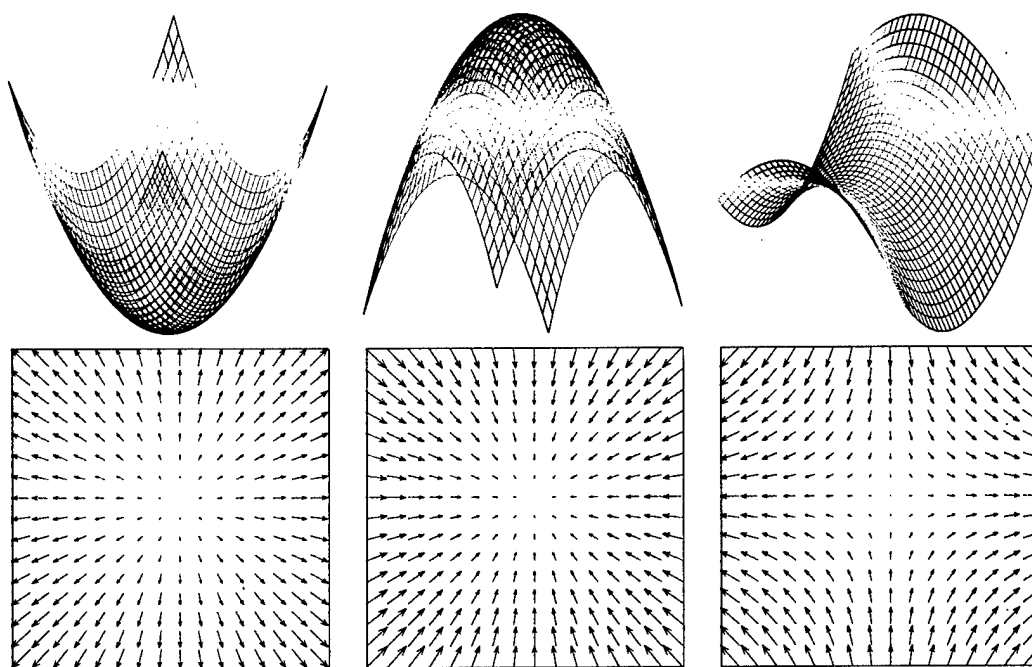


Figure 4.1: Nondegenerate singular points: Minimum, Maximum, Saddle. Bottom: corresponding gradient vector flows.

point). As we can see, a cusp curve is the intersection of a surface with the plane at the the cusp point.

Morse lemma says that near p_0 there is a smooth change of coordinates under which the resulting Taylor series of the Morse function f near p_0 is the pure quadratic function.

Theorem 4.4 *Morse functions are stable and dense in the set of all smooth functions. Equivalently, any smooth function can be converted into a Morse function as a result of a perturbation as slight as desired.*

This Morse's theorem says that a small, smooth perturbation of a Morse function yields another Morse function. The density means that there is a Morse function arbitrarily close to any non-Morse function.

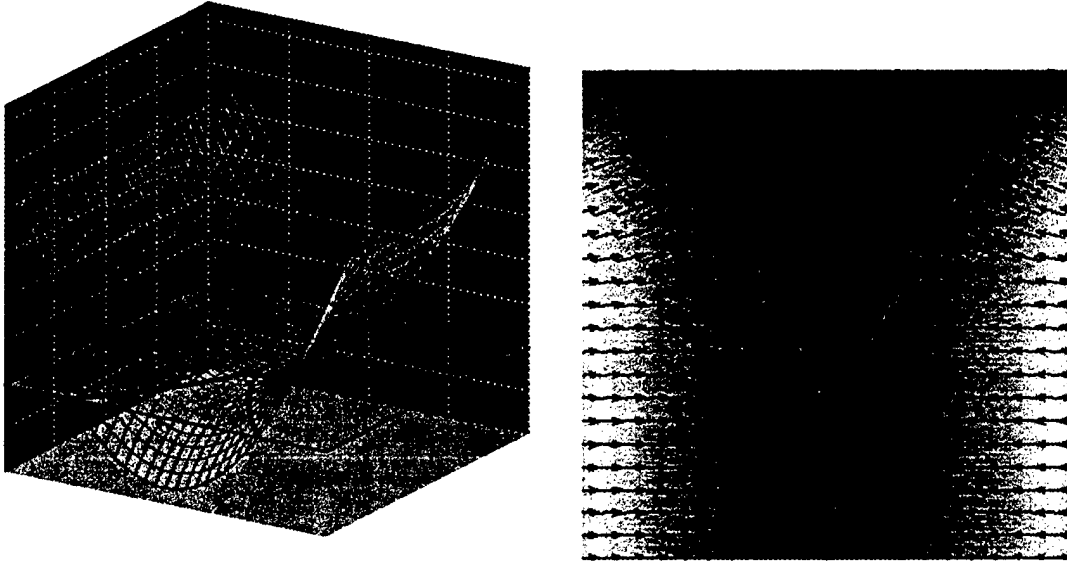


Figure 4.2: Degenerate singularity: cusp point/curve

4.3.2 Almost all images are Morse functions

A height function defined on a smooth manifold M is a real-valued function $h : M \rightarrow \mathbb{R}$ such that $h(x, y, z) = z$ for all $(x, y, z) \in M$. Hence, h is the orthogonal projection with respect to the z -axis. Figure 4.3 shows a manifold and the critical points of its height function. These singular points are all nondegenerate.

In particular, the height function defined on the graph \mathcal{U} of an image u is given by $h(r(x, y)) = u(x, y)$. Hence, the process for finding and classifying the singularities of the image u is the same as that for the singularities of h by changing its local coordinates. Let p_0 be a nondegenerate singularity of h on the graph \mathcal{U} of the image u . Then, there exists $(x_0, y_0) \in \Omega$ such that $p_0 = (x_0, y_0, u(x_0, y_0))$. Morse lemma yields

$$h(x, y, u(x, y)) = h(x_0, y_0, u(x_0, y_0)) \pm x^2 \pm y^2, \quad \forall (x, y) \in \Omega,$$

or equivalently,

$$u(x, y) = u(x_0, y_0) \pm x^2 \pm y^2, \quad \forall (x, y) \in \Omega.$$

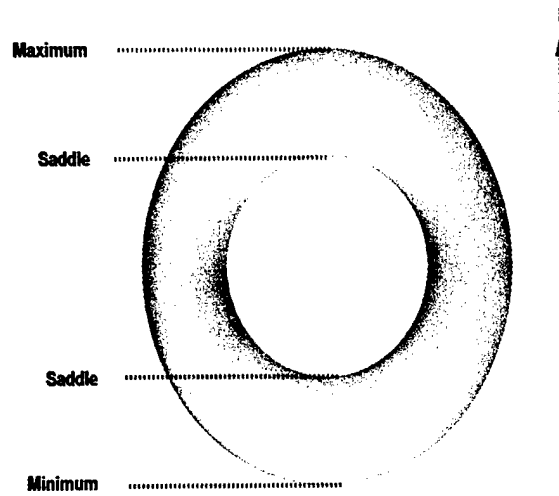


Figure 4.3: A 3-D object and the critical points of its height function.

Now we need to find out when a critical point for the height function is nondegenerate, since we are interested in functions whose critical points are nondegenerate. For this we use the concept of the Gauss map that assigns to each point $p \in \mathcal{U}$ the point on the unit sphere that is parallel to the unit normal $\mathcal{N}(p)$. Since \mathcal{U} is smooth, it follows that the Gauss map is smooth. The next result links the height function to the Gauss map.

Proposition 4.5 *The height function on the graph \mathcal{U} of an image u is a Morse function if and only if the Gauss map is a regular patch.*

Proof: By definition the height function on the image graph is u . Thus, let (x, y) be a nondegenerate critical point of the image u , that is $\nabla u(x, y) = 0$ and $\det(\nabla^2 u(x, y)) \neq 0$. For the sake of simplicity, we project the Gauss map g centrally from the origin to the plane $z = 1$ to get $g(x, y) = (-u_x, -u_y, 1)$ which is the unnormalized surface normal. Hence, the cross product $g_x \times g_y = -\det(\nabla^2 u) \neq 0$, that is the Gauss map is a regular patch. The converse clearly holds as well. ■

4.3.3 Topological equivalence of images

Let $u, v : \Omega \subset \mathbb{R}^2 \rightarrow \mathbb{R}$ two smooth images defined on the same domain Ω , and let $\mathbf{r} : \Omega \rightarrow \mathcal{U}$ and $\mathbf{s} : \Omega \rightarrow \mathcal{V}$ their respective Monge patches, where \mathcal{U} and \mathcal{V} are the image graphs of u and v respectively. Since a Monge patch of a smooth image is a diffeomorphism, it follows that the map $\mathbf{s} \circ \mathbf{r}^{-1} : \mathcal{U} \rightarrow \mathcal{V}$ is also a diffeomorphism. Hence the image graphs \mathcal{U} and \mathcal{V} are topologically equivalent, that is one can be transformed into the other.

4.4 Image singularity-based flow

Recall that by definition a degenerate singular point satisfies the conditions

$$\nabla u = 0 \quad \text{and} \quad \det(\nabla^2 u) = 0.$$

Hence, we might formulate the degeneracy of a singularity in the calculus of variations framework [36] as an optimization problem given by

$$\min_u \frac{1}{2} \int_{\Omega} \{ (1 - \epsilon) |\nabla u| + \epsilon |\det(\nabla^2 u)| \} dx, \quad \epsilon \in [0, 1] \quad (2)$$

Taking the first variation and using the identity $\frac{\partial}{\partial M} \det(M) = \det(M)(M)^{-T}$ for a non-singular matrix M , we derive the Euler-Lagrange equation which can be solved using the following gradient descent flow given by

$$u_t = (1 - \epsilon) \nabla \cdot \left(\frac{\nabla u}{|\nabla u|} \right) - \epsilon \Lambda \cdot \left(\frac{\det(\nabla^2 u)}{|\det(\nabla^2 u)|} (u_{yy}, -u_{xy}, u_{xx}) \right),$$

where $\Lambda = (\frac{\partial^2}{\partial x^2}, 2\frac{\partial^2}{\partial x \partial y}, \frac{\partial^2}{\partial y^2})$ is a second order differential operator. Here we assume homogeneous Dirichlet and Neumann boundary conditions $u = u_{\nu} = 0$, where u_{ν} denotes the directional derivative of u in the direction of the unit normal ν .

4.5 Numerical simulations

We demonstrate the performance of the proposed technique by applying it to real images. A test image of a fighter jet F16 is shown in Figure 4.4(a). In order to extract the degenerate critical

points, we use a zero crossing technique to find the locations where both the gradient and the Hessian determinant of the image vanish. Figure 4.4(b) shows the extracted 330 degenerate singularities that are indicated by the sign “+” in the image. Figure 4.4(c) and 4.4(d) show the results of applying the heat flow and the proposed flow with their corresponding degenerate singularities. As we can see, the proposed flow preserves more degenerate critical points (178 landmarks), while for the heat flow the number of landmarks drops rapidly to 12. In Figure 4.5, we plot the number of degenerate singular points versus the iteration number for the heat flow and the proposed technique, and it can be seen clearly that the proposed approach performs the best.

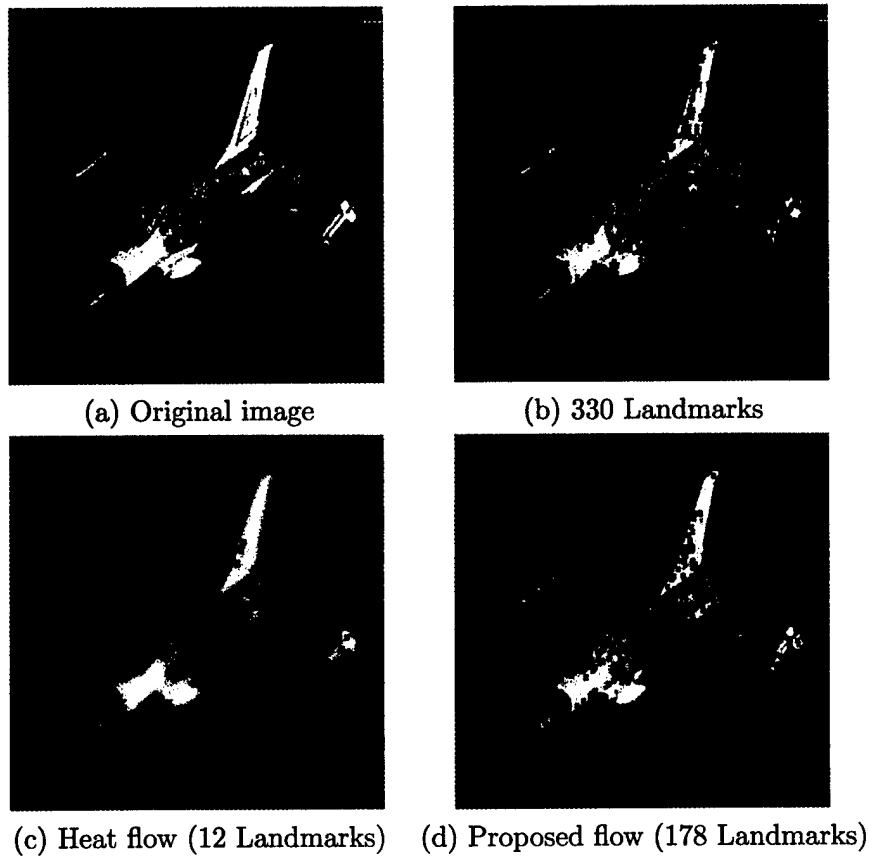


Figure 4.4: Evolution of image singularities.

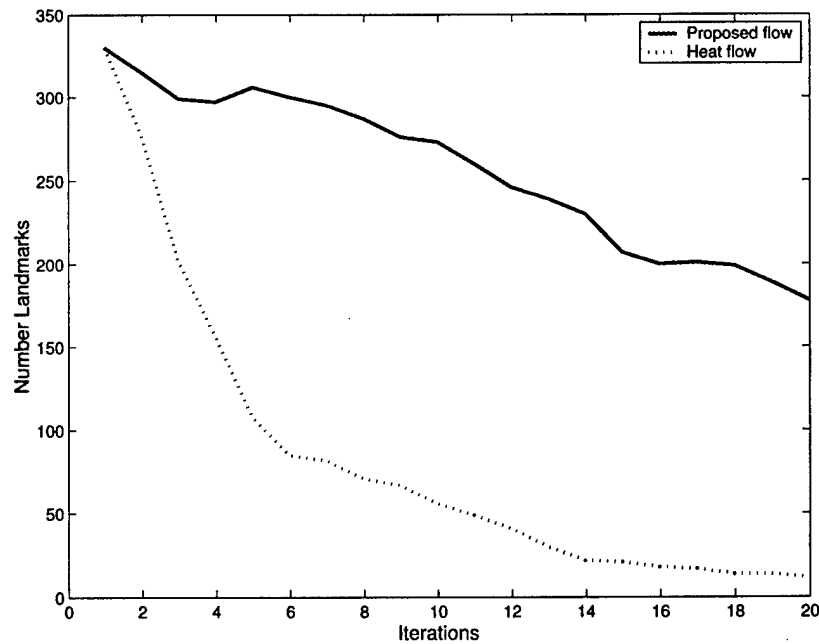


Figure 4.5: Number of degenerate singularities vs. iteration number.

4.6 Conclusions

We have presented an image singularity-based flow expressed in the calculus of variations framework. This approach is based on a variational functional that incorporates both differential geometry and topology. The proposed model provides motivation for further investigation, and our future efforts will be focused in applying this approach to a variety of image processing and computer vision tasks such as image registration, motion estimation, shape from shading, and object recognition.

Topological Modeling of Illuminated Surfaces

In this Chapter, we give a formulation of object singularities in a Morse theoretic setting. Then, we analyze the Reeb graph representation in the shading problem framework, and we derive some relevant theoretical properties of the height function in the light direction of an illuminated 3D object [18]. In addition, we prove that such a height function is closely related to the generalized bas-relief transformation.

5.1 Introduction

The Reeb graph concept is an efficient representation that captures the topological properties of three-dimensional (3D) objects. The vertices of the Reeb graph are the singular points of a function defined on the underlying surface of a 3D object [67, 31]. The vertices of the Reeb graph are the singular points of a function defined on the underlying object [67, 68, 31]. These singularities are prominent landmarks and their detection, recognition, and classification is a crucial step in image processing and computer vision [31]. Such singularities carry important information for further operations, such as image registration, shape analysis, motion estimation, object recognition, and surface/image evolution [52, 16]. Depending on whether the Hessian matrix of a function defined on the underlying object is singular or not, the critical points may be divided into two classes: degenerate and nondegenerate respectively [55, 31]. The so-called Morse theory [55, 31] studies the properties of a Morse function (i.e. a function that has only nondegenerate singular points) and it describes the topology changes of the level sets of this function at those singularities. Regular

or noncritical points do not affect the number or genus of the components of the level sets. It can be shown that Morse functions are dense and stable in the set of all smooth functions, that is the structure of nondegenerate singularities does not change under small perturbations. The basic ingredients of Morse theory are *Morse lemma* and *deformation lemma* [55, 31]. The former states that in a neighborhood of a nondegenerate singularity, a function is reduced to a quadratic form in an appropriate system of coordinates, while the latter lemma essentially states that two level sets of a Morse function are topologically equivalent and can be deformed onto one another if there is no singularity between them. The Reeb graph representation is a result of extracting and encoding the singular points of a Morse function defined on a 3D object.

The rest of this Chapter is organized as follows. The next section is devoted to the topological characterization of object singularities with an emphasis on Morse theory and its implications, followed by a mathematical description of the Reeb graph representation for 3D data. In Section 5.3, we establish a link between the shading problem and the height function in the light direction. Then, we derive some relevant properties of this height function, and we show its relation to the generalized bas-relief transformation. And finally in Section 5.4, we provide numerical simulations to show the application and the power of object singularities in topological modeling through the Reeb graph representation.

5.2 Reeb graph representation

5.2.1 Morse theory and singularities

Morse theory explains the presence and the stability of critical points in terms of the topology of the underlying smooth manifold. Topology is the property that determines which parts of the shape of objects are connected to which other parts [38], while geometry determines where, in a given coordinate system, each part is located [29]. The basic principle is that the topology of a manifold is very closely related to the critical points of a smooth function on that manifold [55].

Let $\varphi : \mathbb{M} \rightarrow \mathbb{R}$ be a real-valued function defined on a smooth manifold $\mathbb{M} \subset \mathbb{R}^3$. The function φ is smooth if the composition function $\varphi \circ r : \Omega \rightarrow \mathbb{R}$ is smooth (in the ordinary Euclidean sense),

where \mathbf{r} is a smooth regular parametrization of \mathbb{M} (i.e. $\mathbf{r} : \Omega \rightarrow \mathbb{R}^3$). A point \mathbf{p}_0 on \mathbb{M} is a singularity or critical point of φ if $\mathbf{p}_0 = \mathbf{r}(x_0, y_0)$, for some $(x_0, y_0) \in \Omega$, and the gradient of $\varphi \circ \mathbf{r}$ at (x_0, y_0) vanishes, i.e. $\nabla(\varphi \circ \mathbf{r}(x_0, y_0)) = 0$.

A singular point \mathbf{p}_0 is nondegenerate if the Hessian matrix $\nabla^2(\varphi \circ \mathbf{r}(x_0, y_0))$ is nonsingular [55, 21, 31].

Definition 5.1 *A smooth function $\varphi : \mathbb{M} \rightarrow \mathbb{R}$ on a smooth manifold \mathbb{M} is called a Morse function if all its singular points are nondegenerate.*

Nondegenerate singularities are isolated, that is, there cannot be a sequence of nondegenerate singularities converging to a nondegenerate singularity \mathbf{p} . This fact follows from a Morse lemma which says that near \mathbf{p}_0 there is a smooth change of coordinates under which the resulting Taylor series of the Morse function h near \mathbf{p}_0 is a pure quadratic function. Note that the only nondegenerate singularities are the minimum, maximum and saddle points.

Another important result is Morse theorem which says that a small, smooth perturbation of a Morse function yields another Morse function. The density means that there is a Morse function arbitrarily close to any non-Morse function.

5.2.2 Height function

A height function on a smooth manifold \mathbb{M} is a real-valued function $h : \mathbb{M} \rightarrow \mathbb{R}$ such that $h(x, y, z) = z$ for all $(x, y, z) \in \mathbb{M}$. Hence, h is an orthogonal projection with respect to the z -axis. Figure 5.1 shows a 2D manifold (a double torus) and the critical points of its height function. These singular points are all nondegenerate.

5.2.3 Reeb graph

An interesting concept related to Morse theory and very useful to analyze a surface topology is the Reeb graph. The latter is defined as a quotient space \mathbb{M}/\sim with the equivalence relation given by $\mathbf{p} \sim \mathbf{q}$ if and only if $h(\mathbf{p}) = h(\mathbf{q})$ and \mathbf{p}, \mathbf{q} belong to the same connected component of $h^{-1}(h(\mathbf{p}))$. In particular, each connected component is represented by a point in the Reeb graph as illustrated

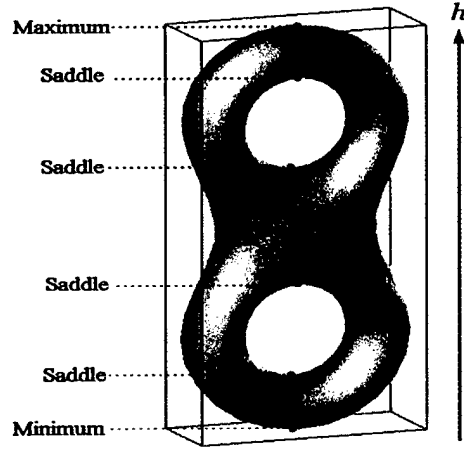


Figure 5.1: A 3-D object and the critical points of its height function.

in Figure 5.2. The left figure shows a torus with the critical points of its height function (Morse function). The figure in the middle illustrates the geometric features of the torus represented by cross-sections along its height. The right figure shows the topological features represented by the Reeb graph. By taking an appropriate number of cross-sections and smooth interpolation between, Shinagawa *et al.* [67, 68] proposed a Reeb graph based approach or so-called *homotopy model* for object reconstruction. The Reeb graph is a topological representation of an object (skeletal structure), and has the advantage to be stored or transmitted with a much smaller amount of data.

Mathematically, a quotient space $\mathbb{M}/\sim = \{[p] : p \in \mathbb{M}\}$ is the set of equivalence classes of the relation \sim , where $[p] = \{q \in \mathbb{M} : q \sim p\}$ is the equivalence class of $p \in \mathbb{M}$. Intuitively, \mathbb{M}/\sim is a space created by taking the space \mathbb{M} and gluing p to any q that satisfies $q \sim p$. The classes $[p]$ are the connected components for the Reeb graph, and being in the same component is an equivalence relation:

$$q \sim p \iff h(q) = h(p) \text{ and } p, q \in \text{ConComp}\{h^{-1}(h(p))\},$$

where $\text{ConComp}\{\cdot\}$ denotes the connected component. In the Reeb graph representation, each connected component of a contour (i.e. $h^{-1}(z)$ where $z = h(x, y, z)$) corresponds to a point.

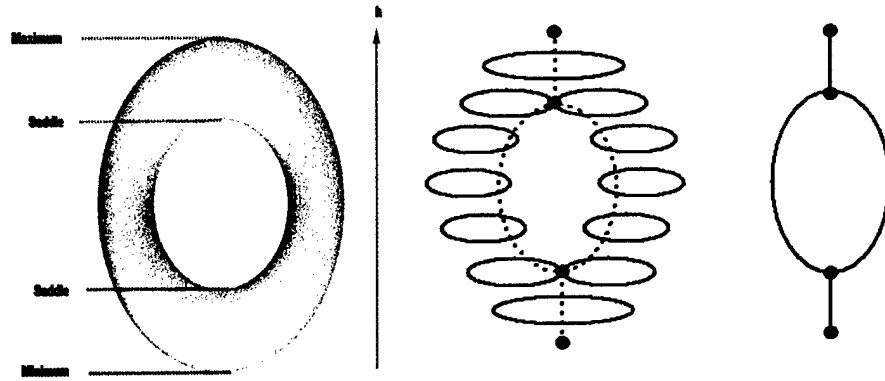


Figure 5.2: Reeb graph representation of a torus. The dot \bullet denotes a critical point of the height function.

5.3 Shading problem and height function

5.3.1 Shading function

Shadows provide perceptually important information about the shape of an illuminated surface. Shadows occur when objects totally or partially occlude direct light rays from a light source. A shadow can be divided into two classes: self-shadow (or attached shadow) and cast shadow [41]. The former is a portion of a surface not illuminated by light rays (i.e. facing away from the light source), while the latter is the area projected by the object in the direction of light source on the surface (extrinsic cast shadow) or projected on the surface itself (intrinsic cast shadow). Note that a convex object such as an egg-shell does not cast shadow on itself, that is there is no intrinsic cast shadow. Both shadows provide perceptually important information about the shape of the surface or object. These two types of shadows are illustrated in Figure 5.3(a)

Let M be a Lambertian surface with unit constant albedo, that is, it reflects light equally in all directions. Assuming distant point source illumination in the direction $L = (\ell_1, \ell_2, \ell_3)$. The unit vector $L \in S^2$ (unit sphere) is pointing towards the light source. We define the *shading function* $\sigma : M \rightarrow \mathbb{R}$ as the inner product $\sigma(p) = N(p) \cdot L$, where N is the surface unit normal (see

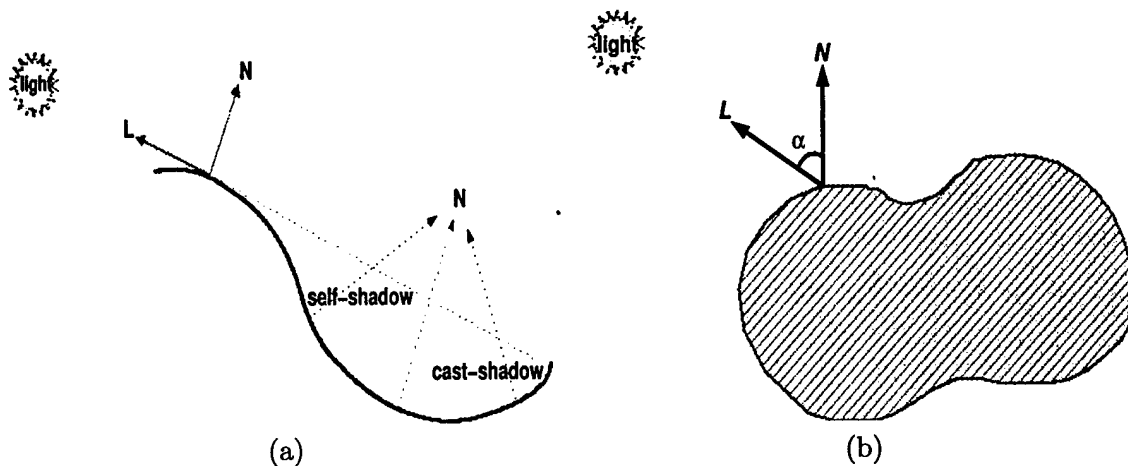


Figure 5.3: (a) Self-shadow and cast shadow, (b) illumination of a Lambertian surface.

Figure 5.3(b)). It is important to note that the shading function has a similar definition to that of the surface curvatures such as the Gaussian curvature $K : \mathbb{M} \rightarrow \mathbb{R}$.

The zero-level set $C = \sigma^{-1}(0)$ of the shading function is called the *horizon curve*, that is, the set of points where the light direction is orthogonal to the surface. The set of points in the surface not reached by the light rays (the part of the surface that is not illuminated), that is, $\Sigma = \{p \in \mathbb{M} : \sigma(p) < 0\}$, is called *self-shadow*. It is known that if the surface \mathbb{M} is convex and illuminated in all directions, then the self-shadow is a connected set. The converse problem, however, does not always hold. Ghomi [34, 35] recently studied the question: *does connectedness of the self-shadows imply convexity of the surface?* Using Morse theory, Ghomi proved that the answer is *yes* provided that each self-shadow is *simply* connected.

For almost all $L \in S^2$ the horizon curve is a regular curve. It can also be shown that if the horizon curve is connected, then it coincides with the boundary of the self-shadow [35].

In particular, if we consider the surface \mathbb{M} as a graph of an image or function $u : \Omega \subset \mathbb{R}^2 \rightarrow \mathbb{R}$, that is, \mathbb{M} is a parametric surface given by a Monge patch $r : \mathbb{M} \rightarrow \mathbb{R}$, then for notational convenience, we may abbreviate $\sigma \circ r$ to σ , so that the shading function or shading image (i.e. the image of the Lambertian surface) may be defined as $\sigma : \Omega \rightarrow \mathbb{R}$ such that $\sigma(x, y) = N(x, y) \cdot L = (-u_x \ell_1 - u_y \ell_2, \ell_3) / \sqrt{1 + u_x^2 + u_y^2}$ for all $(x, y) \in \Omega$. In other words, $\sigma(x, y)$ will denote the values of the shading function at $r(x, y)$. The shading image depends on the illumination, the properties

of the underlying surface and its orientation. It can be expressed as the angle α between the unit surface normal N and the direction of the light source L .

The self-shadow image $\Sigma = \{(x, y) \in \Omega : \sigma(x, y) < 0\}$ is defined as the orthographic projection of the self-shadow curve onto the image plane, that is, the (x, y) -plane.

The local properties of the shading image are better described with respect to its local Gauge frame (η, ξ) defined in terms of the normal and the tangent to the level sets of the shading image as

$$\eta = \frac{\nabla \sigma}{|\nabla \sigma|} \quad \text{and} \quad \xi = \frac{(\nabla \sigma)^\perp}{|\nabla \sigma|}.$$

Figure 5.4 shows the normal and tangential vector fields of the shading image for a synthetic vase model.

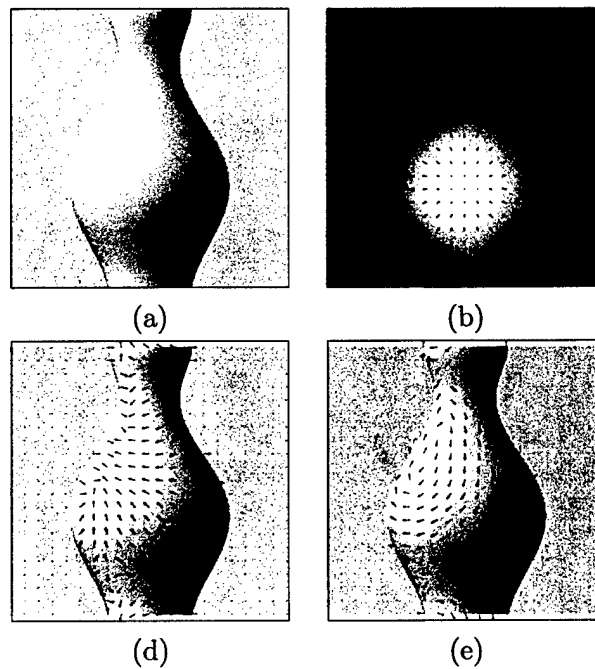


Figure 5.4: (a) Shading image, (b) gradient vector field, (c) shading normal field, and (d) shading tangent field.

5.3.2 Height function in the direction of light

The height function in the light direction \mathbf{L} of an illuminated surface \mathbb{M} is given by $h(\mathbf{p}) = \mathbf{p} \cdot \mathbf{L}$, for all $\mathbf{p} \in \mathbb{M}$.

In particular, if \mathbb{M} is a parametric surface given by $\mathbf{r} : \Omega \rightarrow \mathbb{M}$ such that $\mathbf{r}(x, y) = (x, y, u(x, y))$ where u is a given image or a real-valued function, then the height function on \mathbb{M} in the direction of light \mathbf{L} is the composition of \mathbf{r} with the orthogonal projection to the line spanned by \mathbf{L} , and is defined as $h(x, y) = \mathbf{r}(x, y) \cdot \mathbf{L} = \ell_1 x + \ell_2 y + \ell_3 u(x, y)$.

Denote by \mathcal{H} the graph of the function h , and let $\mathbf{q} \in \mathcal{H}$. It is easy to verify that $\mathbf{q} = \mathcal{Z}\mathbf{p}$, where \mathcal{Z} is the matrix given by

$$\mathcal{Z} = \begin{pmatrix} 1 & 0 & 0 \\ 0 & 1 & 0 \\ \ell_1 & \ell_2 & \ell_3 \end{pmatrix}.$$

Proposition 5.2 Assume that $\ell_3 \neq 0$, and let $\widehat{\mathbf{N}}$ be the unit surface normal the surface \mathcal{H} , we then have

$$\widehat{\mathbf{N}} = \left(\frac{1 + \|\nabla u\|^2}{1 + \|\nabla h\|^2} \right)^{1/2} \det(\mathcal{Z}) \mathcal{Z}^{-T} \mathbf{N}.$$

Proof: By definition, the unit normal to the surface \mathcal{H} is given by

$$\begin{aligned} \widehat{\mathbf{N}} &= \frac{\widehat{\mathbf{r}}_x \times \widehat{\mathbf{r}}_y}{\|\widehat{\mathbf{r}}_x \times \widehat{\mathbf{r}}_y\|} \\ &= \left(\frac{\|\mathbf{r}_x \times \mathbf{r}_y\|}{\|\widehat{\mathbf{r}}_x \times \widehat{\mathbf{r}}_y\|} \right) \begin{pmatrix} \ell_3 & 0 & -\ell_1 \\ 0 & \ell_3 & -\ell_2 \\ 0 & 0 & 1 \end{pmatrix} \frac{\mathbf{r}_x \times \mathbf{r}_y}{\|\mathbf{r}_x \times \mathbf{r}_y\|} \\ &= \left(\frac{\|\mathbf{r}_x \times \mathbf{r}_y\|}{\|\widehat{\mathbf{r}}_x \times \widehat{\mathbf{r}}_y\|} \right) \det(\mathcal{Z}) \mathcal{Z}^{-T} \mathbf{N}, \end{aligned}$$

where \mathbf{r} and $\widehat{\mathbf{r}}$ are the Monge patches for \mathbb{M} and \mathcal{H} respectively. ■

Proposition 5.3 *Let $(p, q) \in \mathbb{M} \times \mathcal{H}$. The point p is a on the self-shadow of \mathbb{M} in the light direction L if and only if the point q is on the self-shadow of \mathcal{H} in the light direction $\hat{L} = ZL$.*

Proof: The result follows using Proposition 5.2 and the following relation

$$\begin{aligned}\widehat{N} \cdot \widehat{L} &= \left(\frac{1 + \|\nabla u\|^2}{1 + \|\nabla h\|^2} \right)^{1/2} \det(Z) \left((Z^{-T} N) \cdot (ZL) \right) \\ &= \left(\frac{1 + \|\nabla u\|^2}{1 + \|\nabla h\|^2} \right)^{1/2} \det(Z) (N \cdot L).\end{aligned}$$

Thus, $\widehat{N} \cdot \widehat{L} < 0$ if and only if $N \cdot L < 0$. ■

It is interesting to point out that the height function in the direction of an arbitrary vector (a, b, c) with $c > 0$ is also referred to as the generalized bas-relief transformation proposed by Belhumeur *et al.* [5] who have shown that there exists an ambiguity in determining the structure of the underlying surface since both the surface and its generalized bas-relief surface produce identical set of images under arbitrary illumination, and therefore they are indistinguishable for recognition purposes [5]. The above propositions prove that the generalized bas-relief transformation is not the only one that produces the same set of images under arbitrary illumination as suggested in [5], and that the height function in the light direction on an illuminated surface is another alternative representation to further understand and investigate the shading problem.

5.3.3 Singularities of the shading function

The shading function of a manifold \mathbb{M} is defined as $\sigma(p) = N(p) \cdot L$, where N is the surface unit normal, and $L = (\ell_1, \ell_2, \ell_3)$ is a unit vector representing the light source direction. By a rigid motion, we may move \mathbb{M} tangent to the (x, y) -plane at $p = 0$, so that \mathbb{M} is locally a graph given by $z = u(x, y)$ with $u(0, 0) = u_x(0, 0) = u_y(0, 0) = 0$. Thus, the unit normal can be written as $N = (-u_x, -u_y, 1) / \sqrt{1 + u_x^2 + u_y^2}$. To study the singularities of the shading function and therefore the singularities of the Gauss map, it is more easy to simplify the expression of the unit normal by projecting centrally from the origin to the plane $z = 1$ to get $(-u_x, -u_y, 1)$, and then project to the (x, y) -plane to get a simplified mapping referred to as the modified gauss map \overline{N} defined as

$\overline{N}(x, y) = (-u_x, -u_y)$. Recall that a central projection of a point $p = (x, y, z) \in \mathbb{M}$ onto the plane $z = 1$ is equal to $(x/z, y/z, 1)$.

The modified gauss map is singular when its Jacobian matrix $\mathcal{J}_{\overline{N}} = -\nabla^2 u$ has rank less than 2, that is, when $\det(\nabla^2 u) = 0$. On the other hand, assuming that the third component of the light direction is positive (i.e. $\ell_3 > 0$), the shading function is equivalent a shading function with light direction $(\ell_1, \ell_2, 1)$, where ℓ_1 and ℓ_2 are arbitrary and $\ell_3 = 1$. Hence, the shading function simplifies to $\sigma(x, y) = \overline{N}(x, y) \cdot \overline{L}$, where $\overline{L} = (\ell_1, \ell_2)$. The shading function is still denoted $\sigma(x, y)$ for convenience.

Proposition 5.4 *Then the gradient of the shading function is given by*

$$\nabla \sigma(x, y) = -(\nabla^2 u(x, y)) \overline{L}.$$

A critical point of the shading function satisfies $(\nabla^2 u) \overline{L} = 0$. At regular points of the shading function, the horizon curve is locally a smooth curve.

Proof: Taking the gradient of the shading function, we get

$$\nabla \sigma(x, y) = (-u_{xx}\ell_1 - u_{xy}\ell_2, -u_{xy}\ell_1 - u_{yy}\ell_2) = -(\nabla^2 u(x, y)) \overline{L}.$$

Hence, $\nabla \sigma(x, y) = 0$ if and only if $(\nabla^2 u) \overline{L} = 0$. At a regular point, we have $(\nabla^2 u) \overline{L} \neq 0$, and using the implicit function theorem, it follows that the horizon curve is smooth in the neighborhood of a regular point. ■

The above result shows that the local orientation of the shading function is related to the local curvature of the underlying surface. Furthermore, in the orthonormal coordinate frame $\{e_1, e_2\}$, where e_1 and e_2 are the principal directions, the Hessian matrix can be expressed as

$$\nabla^2 u = \begin{pmatrix} \kappa_1 & 0 \\ 0 & \kappa_2 \end{pmatrix},$$

where κ_1 and κ_2 are the principal curvatures. Hence the gradient of the shading function becomes $\nabla \sigma = -\kappa_1 \ell_1 - \kappa_2 \ell_2$. At a singular point of the shading function, we have $\text{atan}(\kappa_2/\kappa_1) = -\text{atan}(\ell_1/\ell_2)$, that is the shape index of the surface depends only on the light coordinates.

The next result gives a necessary and sufficient condition for a nondegenerate singular point of the shading function.

Proposition 5.5 *The Hessian matrix of the shading function is given by*

$$\nabla^2 \sigma(x, y) = \begin{pmatrix} -u_{xxx}\ell_1 - u_{xxy}\ell_2 & -u_{xxy}\ell_1 - u_{xyy}\ell_2 \\ -u_{xxy}\ell_1 - u_{xyy}\ell_2 & -u_{xyy}\ell_1 - u_{yyy}\ell_2 \end{pmatrix}.$$

The shadow function is a Morse function if and only if $\det(\nabla^2 \sigma) \neq 0$.

5.4 Experimental results

The Reeb graph describes the topological structure of objects, and illustrates the topological changes occurred at singular points of the height function (i.e. topological changes of the level sets $h^{-1}(z)$ such as merging or splitting). The topological structure offered by the Reeb graph is very useful for object reconstruction from real data sets such as computed tomography (CT) and magnetic resonance imaging (MRI) usually available as cross-sections. So we need to reconstruct the object from these cross-sections and using the a priori topological information given by the Reeb graph. Furthermore, the Reeb graph describes how the cells are glued to reconstruct an object surface.

Figure 5.5 and Figure 5.6 illustrate the Reeb graph representations of two 3D models: the heart and the hand models. The vertices of these Reeb graphs are the singular points of the height function in the light direction $L = (0, 0, 1)$. The polygonal mesh of the 3D heart model consists of 861 vertices and 1717 faces (triangles), whereas the 3D hand object is a laser scanner model consisting of 38219 vertices and 76438 faces.

5.5 Conclusions

Shadows provide perceptually important information about the shape of an illuminated surface. We have proposed a new surface representation function that provides a flexible and orientation-based

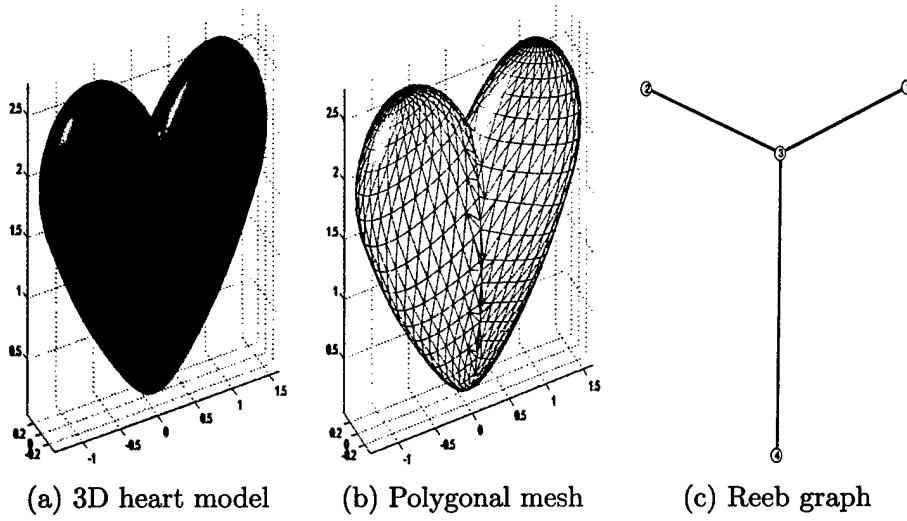


Figure 5.5: Reeb graph of the heart model.

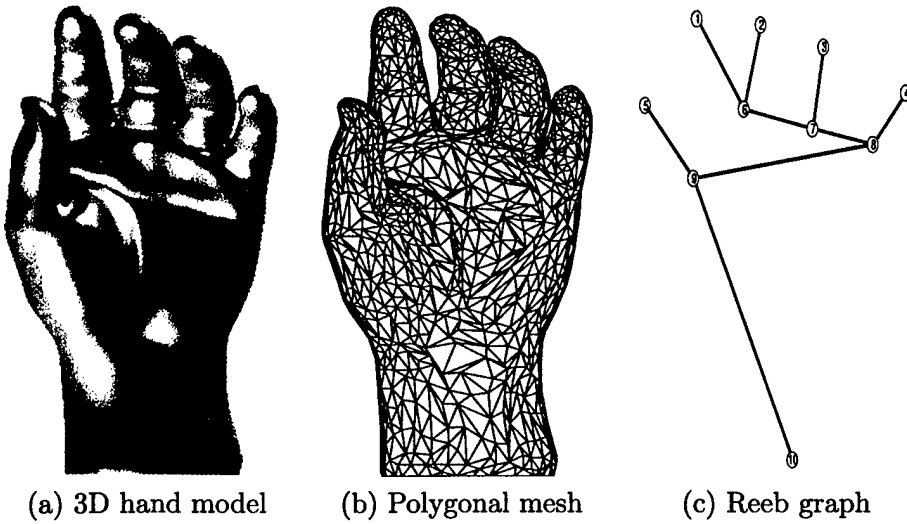


Figure 5.6: Reeb graph of the hand model.

model for geometric and topological modeling of surfaces. The geometric and topological properties of the proposed representation function have been analyzed in the Morse theory framework.

Geodesic Matching of 3D Objects

In this Chapter, we propose a new approach for object matching based on a global geodesic measure. The key idea behind our methodology is to represent an object by a probabilistic shape descriptor called *geodesic shape distribution* [10] that measures the global geodesic distance between two arbitrary points on the surface of an object. In contrast to the Euclidean distance which is more suitable for linear spaces, the geodesic distance has the advantage to be able to capture the (nonlinear) intrinsic geometric structure of the data. The matching task therefore becomes a one-dimensional comparison problem between probability distributions which is clearly much simpler than comparing 3D structures. Object matching can then be carried out by dissimilarity measure calculations between geodesic shape distributions, and is additionally computationally efficient and inexpensive.

6.1 Introduction

Three-dimensional objects consist of geometric and topological data, and their compact representation is an important step towards a variety of computer vision applications including indexing, retrieval, and matching in a database of 3D models. The latter will be the focus of the present Chapter. There are two major steps in object matching. The first step involves finding a reliable and efficient shape representation or descriptor, and the second step is the design of an appropriate dissimilarity measure for object comparison between the shape representations.

Most three-dimensional shape matching techniques proposed in the literature of computer

graphics, computer vision and computer-aided design are based on geometric representations which represent the features of an object in such a way that the shape dissimilarity problem reduces to the problem of comparing two such object representations. Feature-based methods require that features be extracted and described before two objects can be compared. Among feature-based methods, one popular approach is graph matching, where two objects are represented by their graphs composed of vertices and edges. An efficient representation that captures the topological properties of 3D objects is the *Reeb graph* descriptor proposed by Shinagawa *et al.* [67, 68]. The vertices of the Reeb graph are the singular points of a function defined on the underlying object [67, 68, 31]. These singularities are prominent landmarks and their detection, recognition, and classification is a crucial step in image processing and computer vision [31]. Such singularities carry important information for further operations, such as image registration, shape analysis, motion estimation, object recognition, and surface/image evolution [53, 21, 52].

An alternative to feature-based representations, called *shape distribution*, is developed by Osada *et al* [59]. The idea here is to represent an object by a global histogram based on the Euclidean distance defined on the surface of an object. The shape matching problem is then performed by computing a dissimilarity measure between the shape distributions of two arbitrary objects. This approach is computationally stable and relatively insensitive to noise. Because of unsuitability of the Euclidean distance when dealing with nonlinear manifolds, the shape distribution, however, does not capture the nonlinear geometric structure of the data.

The geodesic shape distribution may be used to facilitate representation, indexing, retrieval, and object matching in a database of 3D models. More importantly, the geodesic shape distribution provides a new way to look at the object matching problem by understanding the intrinsic geometry of the shape.

Information-theoretic measures provide quantitative entropic divergences between two probability distributions. A common entropic dissimilarity measure is the Kulback-Liebler (or directed) divergence [50] which has been successfully used in many applications including indexing and image retrieval [69]. Another entropy-based measure is the Jensen-Shannon divergence which may be defined between an arbitrary number of probability distributions [51]. Due to this generalization, the

Jensen-Shannon divergence may be used as a coherence measure between any number of distributions and may be applied to a variety of signal/image processing and computer vision applications including graph matching [39], image edge detection [37] and segmentation of DNA sequences into homogenous domains [64].

The rest of this Chapter is organized as follows. The next section is devoted to the problem formulation. Section 6.3 describes some the related work to our proposed approach for 3D object matching. In Section 6.4, we describe the representation step of our proposed methodology. In Section 6.5, we present the Jensen-Shannon divergence measure and show its attractive properties as a dissimilarity measure between probability distributions. Section 6.6 presents an information geometric approach to geodesic shape distributions. In Section 6.7, we provide numerical simulations to show the power of the proposed shape measure for object matching. And finally, Section 6.8 provides some conclusions.

6.2 Problem formulation

Three-dimensional objects are usually represented as polygonal or triangle meshes in computer graphics and geometric-aided design. A triangle mesh \mathbb{M} is a pair $\mathbb{M} = (\mathcal{V}, \mathcal{T})$, where $\mathcal{V} = \{v_1, \dots, v_m\}$ is the set of vertices, and $\mathcal{T} = \{T_1, \dots, T_n\}$ is the set of triangles.

In scientific visualization and analysis, a triangle mesh is too large to be examined without simplification. One way to overcome this limitation is to represent a triangle mesh by its surface features that can easily be computed and can effectively characterize the global surface shape. The centroids of the set of triangles \mathcal{T} are desirable features which may be computed efficiently and have a global significance for the surface shape representation as illustrated in Figure 6.1. In addition, there is a well defined correspondence between the centroid and the region (triangle) from which it is computed as depicted in Figure 6.1. It is important to point out that centroid-based methods have been used in a variety of computer vision applications including clustering, and one of the widely centroid-based technique used for cluster analysis in the K-mean algorithm [54].

6.2.1 Global shape measure

Let $\mathbb{M} = (\mathcal{V}, \mathcal{T})$ be a triangle mesh. The centroid \mathbf{c}_j of a triangle T_j is the mean of its vertices, that is, the point located at the center of the triangle. Note that the cardinality of the set of centroids $\mathcal{C} = \{\mathbf{c}_1, \dots, \mathbf{c}_n\}$ of the triangle mesh \mathbb{M} is equal to the cardinality of its set of triangles \mathcal{T} .

Unless we establish a meaningful measure of distance between the centroids of a triangle mesh, no meaningful exploration of the underlying structure of an object is possible. In order to take into account the interaction between the centroids, we compute a pairwise distance measure $d(\mathbf{c}_i, \mathbf{c}_j)$ from any centroid \mathbf{c}_i to all the other centroids $\mathbf{c}_j \in \mathcal{C}$. Figure 6.1 illustrates an arbitrary distance between two centroids. Notice that distance d need not be an Euclidean metric.

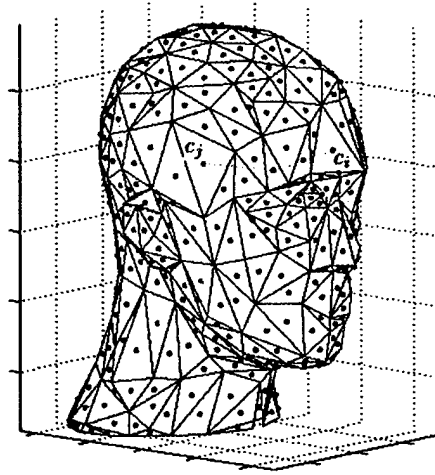


Figure 6.1: Distance between two arbitrary centroids of a 3D camel.

To obtain a global measure of the shape \mathbb{M} , we simply integrate over all centroids. More precisely, we define a function $f : \mathcal{C} \subset \mathbb{M} \rightarrow \mathbb{R}$ such that

$$f(\mathbf{c}_i) = \frac{1}{|\mathcal{C}|} \int_{\mathcal{C}} d(\mathbf{c}_i, \mathbf{c}_j)^2 d\mathbf{c}_j, \quad (1)$$

where $d\mathbf{c}_j$ denotes the area element that contains the centroid \mathbf{c}_j , that is, in the discrete domain, $d\mathbf{c}_j = \text{area}(T_j)$ the area of the triangle T_j , and $|\mathcal{C}| = \sum_{j=1}^n \text{area}(T_j)$ is the total area of the surface \mathbb{M} . The function f clearly represents a global measure or a distribution of the shape and therefore

to each 3D model M we will assign its global measure f .

The problem addressed in this Chapter may now be concisely described by the following statement: Given two 3D objects M_1 and M_2 to be matched, find their global measures f_1 and f_2 , and calculate how dissimilar these objects are based on a predefined dissimilarity measure $D(f_1, f_2)$. In other words, the dissimilarity between two objects measures “how different they are”, and a smaller value of D means that the two objects are more similar. Figure 6.2 depicts a block-diagram of the proposed framework.

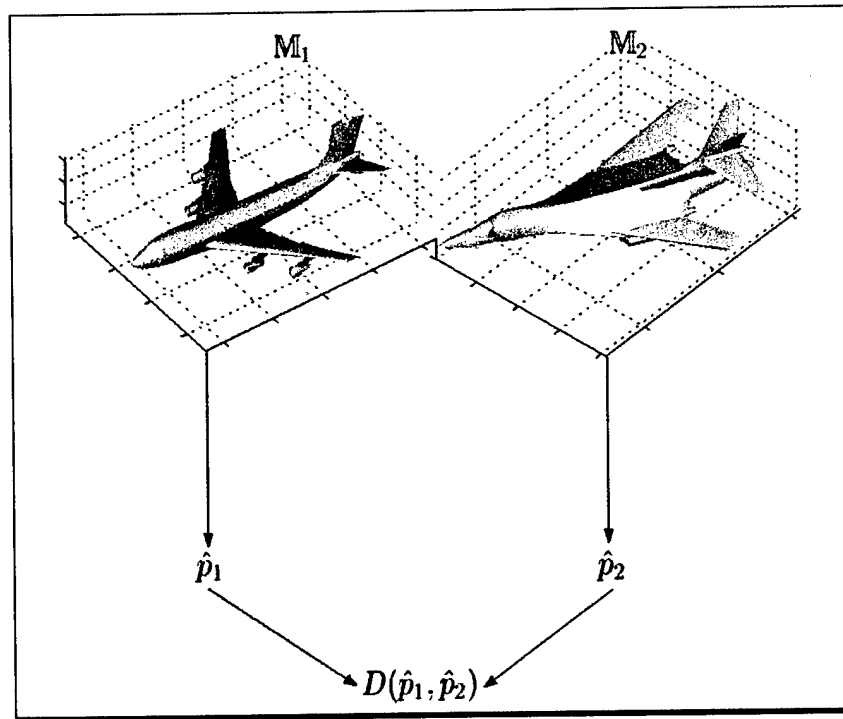


Figure 6.2: Block-diagram of the proposed methodology.

6.2.2 Construction of a measure space

A measure space on a 3D model \mathbb{M} is given by the triple $(\mathcal{C}, \mathcal{B}, \mu)$, where \mathcal{B} is a σ -algebra of subsets of \mathcal{C} , and μ is a measure defined on the set of triangles \mathcal{T} as $\mu(T_j) = \text{area}(T_j) = dc_j$. Note that

$$\mu(\mathcal{C}) = \mu(\cup_{j=1}^n T_j) = \sum_{j=1}^n \mu(T_j) = \sum_{j=1}^n \text{area}(T_j) < \infty,$$

hence μ is a σ -finite measure.

If $\mu(\mathcal{C}) = 1$, then μ is a probability measure and therefore we may define a random vector $X : \mathcal{C} \rightarrow \mathbb{R}^3$ such that $X(c)$ represents the coordinates of the centroid c in the Euclidean space.

The expected value of X is given by

$$E(X) = \min_{p \in \mathbb{M}} \int_{\mathcal{C}} d(p, X(c))^2 d\mu \quad (2)$$

where d is a distance function defined along the surface \mathbb{M} . This expected value provides a nice statistical interpretation of our global shape measure defined in Equation (1).

6.3 Related work

In this section, we will review two representative methods for object matching that are closely related to our proposed approach. We briefly show their mathematical foundations and algorithmic methodologies as well as their limitations.

6.3.1 Reeb graph

Morse theory explains the presence and the stability of critical points in terms of the topology of the underlying smooth manifold [55]. Topology is the property that determines which parts of the shape of objects are connected to which other parts [38], while geometry determines where, in a given coordinate system, each part is located [29]. The basic principle is that the topology of a manifold is very closely related to the critical points of a smooth function on that manifold.

An interesting concept related to Morse theory and very useful to analyze a surface topology is the Reeb graph. The latter is defined as a quotient space \mathbb{M}/\sim with an equivalence relation

given by $p \sim q$ if and only if $h(p) = h(q)$ and p, q belong to the same connected component of $h^{-1}(h(p))$, where $h : M \rightarrow \mathbb{R}$ is the height function such that $h(x, y, z) = z$ for all $(x, y, z) \in M$. In particular, each connected component is represented by a point in the Reeb graph as illustrated in Figure 6.3. The left figure shows a torus with the critical points of its height function (Morse function). The figure in the middle illustrates the geometric features of the torus represented by cross-sections along its height. The right figure shows the topological features represented by the Reeb graph. By taking an appropriate number of cross-sections and smooth interpolation between, Shinagawa *et al.* [67, 68] proposed a Reeb graph based approach or so-called *homotopy model* for object reconstruction.

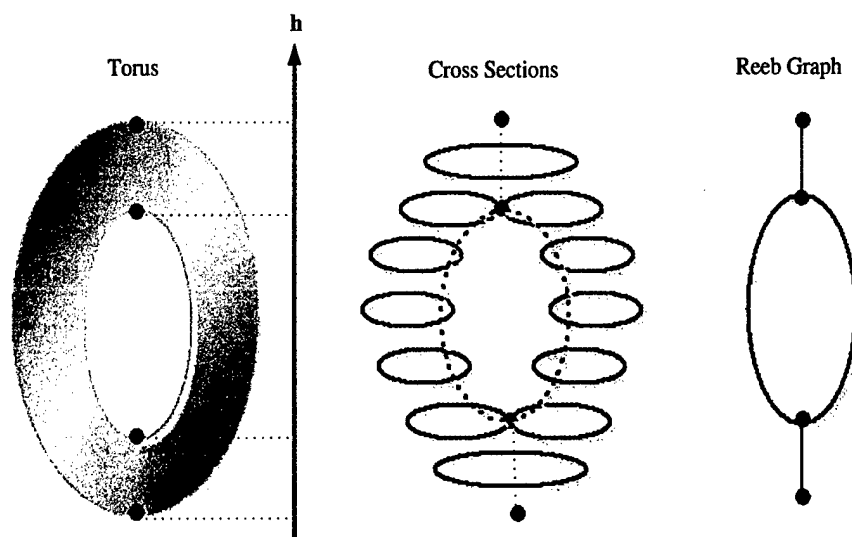


Figure 6.3: Reeb graph representation of a torus.

Figure 6.4 illustrates the Reeb graph representation of a 3D hand model. The vertices of the Reeb graph are the singular points of the height function. The polygonal mesh of the 3D hand object is a laser scanner model consisting of 38219 vertices and 76438 faces.

Reeb graph has a nice mathematical definition that makes it very attractive from a theoretical point of view. This representation, however, is not rotationally invariant. This limitation lead

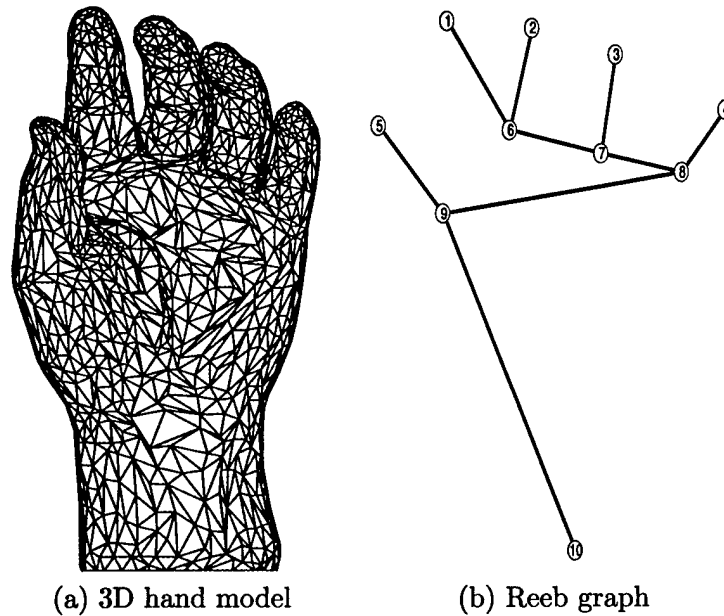


Figure 6.4: Reeb graph of the hand model.

Hilaga *et al* to develop a geodesic-based Reeb graph technique [40]. In this approach a multiresolution Reeb graph is computed efficiently and a similarity distance is calculated to compare two Reeb graphs.

6.3.2 Shape distribution

Recently, Osada *et al* [59] proposed a shape distribution based approach for three-dimensional object matching. The key idea is to compute the Euclidean distance between all pairs of random points on the surface to obtain the so-called *D2 shape histogram*. Given a triangle $T_j = \{v_{j1}, v_{j2}, v_{j3}\}$, each random point is generated as

$$p_j = (1 - \sqrt{r_1})v_{j1} + \sqrt{r_1}(1 - r_1)v_{j2} + \sqrt{r_1}r_2v_{j3},$$

where r_1 and r_2 are pseudo-random numbers between zero and the total cumulative area. Then, the comparison of objects is carried out by computing a dissimilarity measure between their D2 shape distributions. Figure 6.5 illustrates an ellipsoid and its D2 shape distribution. The main drawback

of the shape distribution approach, which is based on the Euclidean distance, is its inability to capture the nonlinear structure of the data.

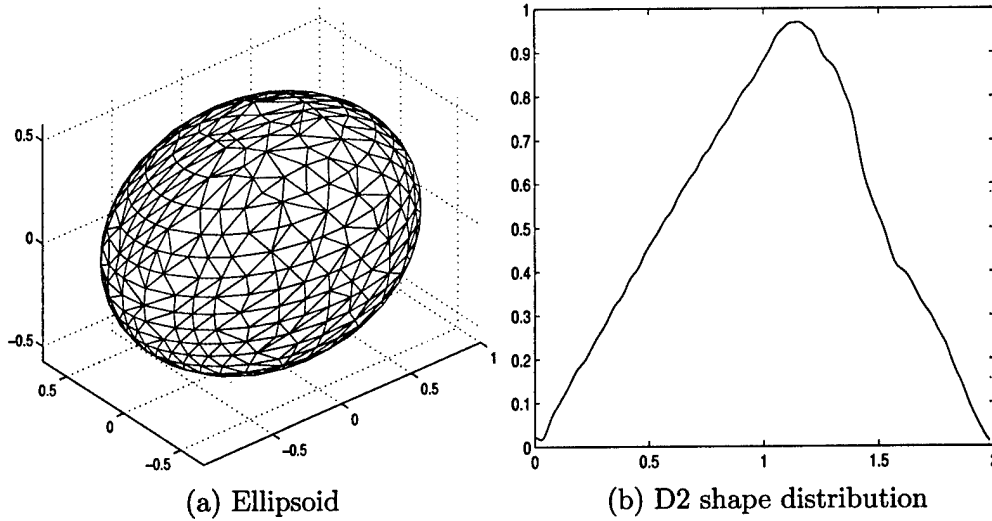


Figure 6.5: D2 shape distribution of an ellipsoid.

6.4 Proposed methodology

The goal of our proposed approach may be described as follows: Given two 3D objects M_1 and M_2 to be matched, find their global measures or shape descriptors f_1 and f_2 , and calculate how dissimilar these objects using a dissimilarity measure $D(f_1, f_2)$ that has to be quantified. The basic idea behind the shape descriptor is to characterize a 3D object with a one-dimensional function which will help us discriminate between objects in a database of 3D models.

6.4.1 Global geodesic shape function

The Reeb graph concept has been shown to be very effective in modeling 3D objects based on cross sections such as MRI or CT images. It is more appropriate to modeling applications where the height is of special interest such as terrain imaging. The height function, however, has some limitations as an object signature for matching, indexing, or retrieval of arbitrary 3D objects. The

main reason is that the height function is not rotationally invariant. To overcome these limitations, we propose a global geodesic function defined on the object surface as follows. Let \mathbf{c}_i and \mathbf{c}_j be two points (centroids) on a manifold \mathbb{M} . The geodesic distance $g(\mathbf{c}_i, \mathbf{c}_j)$ between \mathbf{c}_i and \mathbf{c}_j is the shortest length $L(\gamma) = \int_a^b \|\gamma'(t)\| dt$ of a smooth curve $\gamma : [a, b] \rightarrow \mathbb{M}$ such that $\gamma(a) = \mathbf{c}_i$ and $\gamma(b) = \mathbf{c}_j$. The geodesic distance may be locally viewed as the Euclidean $d_E(\mathbf{c}_i, \mathbf{c}_j) = \|\mathbf{c}_i - \mathbf{c}_j\|$, and is hence clearly invariant to rotation and translation.

Inspired by the geodesic-based representation for 3D topology matching proposed by Hilaga *et al.* [40], we define a global shape function $f : \mathcal{C} \rightarrow \mathbb{R}$ expressed in terms of a rotationally invariant (square) geodesic distance as follows

$$f(\mathbf{c}_i) = \frac{1}{|\mathcal{C}|} \int_{\mathcal{C}} g(\mathbf{c}_i, \mathbf{c}_j)^2 d\mathbf{c}_j. \quad (3)$$

The primary motivation behind the geodesic distance is of overcoming the limitations of the Euclidean distance which by virtue of its linearity in nature cannot account for nonlinear structures in the underlying object.

Unlike the Euclidean distance which is basically a straight line between two points in 3D space, the geodesic distance captures the global nonlinear structure and the intrinsic geometry of the data as illustrated in Figure 6.6. This clearly shows that the Euclidean distance between two arbitrary points in a nonlinear manifold is just a straight segment connecting two points and does not reflect the nonlinear structure of the object, whereas the geodesic distance which is the shortest curve along the manifold connecting both points clearly captures the intrinsic geometry of the object.

Geodesic distance calculation

Given a set of centroids $\mathcal{C} = \{\mathbf{c}_1, \dots, \mathbf{c}_n\}$ of a 3D object represented by a triangle mesh \mathbb{M} , the geodesic distance calculation is based on a similar approach used for computing the isometric feature mapping (Isomap) for multidimensional scaling on nonlinear manifolds [71]. The algorithm has two main steps:

- (i) Construct a neighborhood graph by connecting a given centroid to its k -nearest neighbors, and link these neighboring centroids by edges with weights equal to the Euclidean distances.

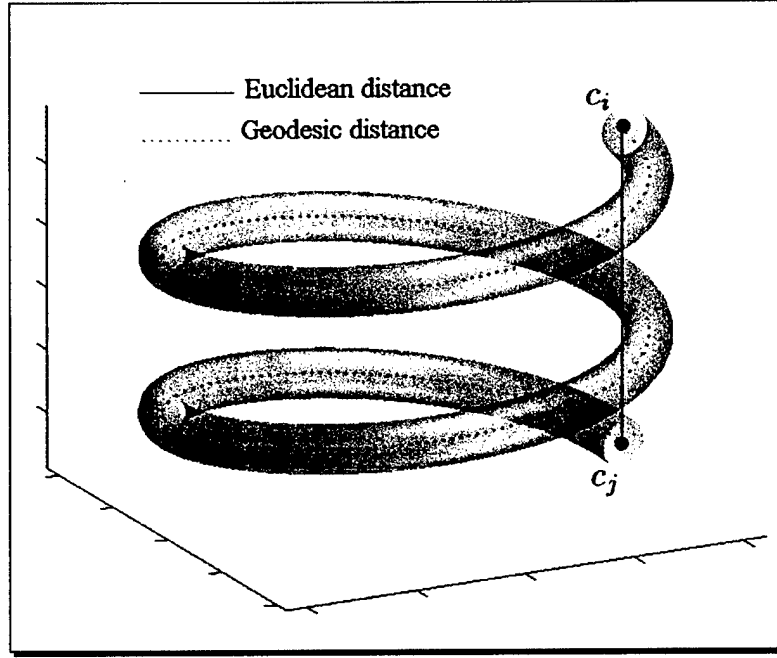


Figure 6.6: Euclidean vs. geodesic distance on a nonlinear manifold.

- (ii) Compute the geodesic distances (shortest paths) between all pairs of n points in the constructed graph using Dijkstra's or Floyd's algorithm

Note that Step (i) may be alleviated by choosing a random subset of \mathcal{C} in order to reduce the computational complexity of the geodesic calculation.

From Equation (3), it is clear that a discrete form of the geodesic shape function can be written as

$$f(c_i) = \frac{(Ga)_i}{|\mathcal{C}|} = \frac{(Ga)_i}{\|\mathbf{a}\|_1}, \quad i = 1, \dots, n \quad (4)$$

where $\mathbf{G} = (g_{ij}^2)$ is the (square) geodesic distance matrix of size $n \times n$, and $\mathbf{a} = (a_1, \dots, a_n)^T$ is an $n \times 1$ vector of triangle areas, i.e. $a_j = \text{area}(T_j)$, and $|\mathcal{C}| = \sum_{j=1}^n a_j = \|\mathbf{a}\|_1$ is the total area. The geodesic distance matrix $\mathbf{G} = (g_{ij}^2)$ is symmetric with zeros in the diagonal, and positive off-diagonal elements

Triangle area calculation

Denote by $\{v_1, v_2, v_3\}$ the vertices of an arbitrary triangle T of a given triangle mesh \mathbb{M} . Using Newell method, the area of the triangle T can be computed as

$$a = \text{area}(T) = \frac{\|N\|}{2},$$

where $N = (N_1, N_2, N_3)$ is the triangle normal vector with coordinates given by

$$\begin{aligned} N_1 &= \sum_{i=1}^d (y_i - y_{\text{next}(i)})(z_i + z_{\text{next}(i)}) \\ N_2 &= \sum_{i=1}^d (z_i - z_{\text{next}(i)})(x_i + x_{\text{next}(i)}) \\ N_3 &= \sum_{i=1}^d (x_i - x_{\text{next}(i)})(y_i + y_{\text{next}(i)}) \end{aligned}$$

and (x_i, y_i, z_i) are the coordinates of each vertex v_i (with dimension $d = 3$) of a triangle T . Note that $v_{\text{next}(i)} = (x_{\text{next}(i)}, y_{\text{next}(i)}, z_{\text{next}(i)})$ denotes the next vertex in the list after v_i , taking into account that v_1 follows the last vertex v_d .

6.4.2 Global geodesic shape distribution

Note that the geodesic shape function can be expressed as a geodesic shape vector $\mathcal{X} = \{X_1, \dots, X_n\}$, where $X_i = f(c_i)$. This vector may be viewed as a shape descriptor that may be used for 3D shape comparison.

Assume that the geodesic shape vector \mathcal{X} of an object \mathbb{M} is a random sample with a common (unknown) probability density function p . A common approach to approximate the probability density function p is through the kernel density estimation which is an important data analytic tool that provides a very effective way of showing structure in a data set [73]. The kernel density estimator \hat{p} is given by

$$\hat{p}(x) = \frac{1}{nh} \sum_{i=1}^n K\left(\frac{x - X_i}{h}\right), \quad (5)$$

where K is the Gaussian kernel, and h is the bandwidth or window width to be estimated. A good

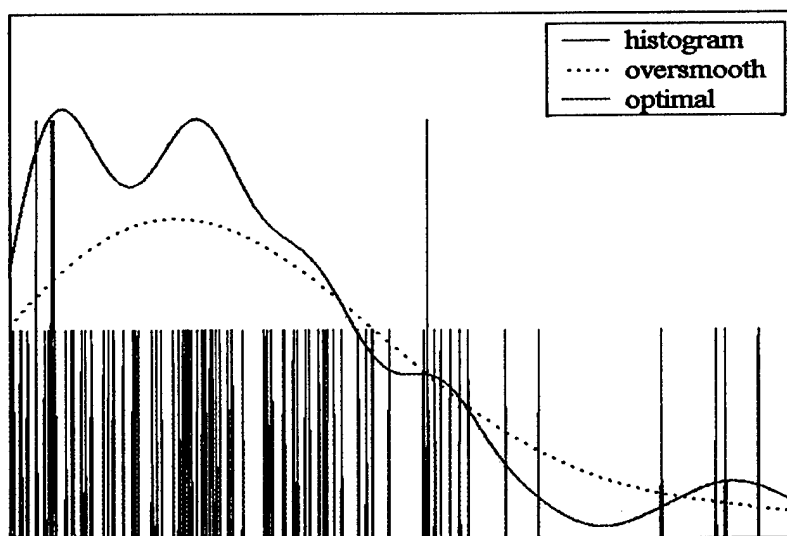


Figure 6.7: Effect of the bandwidth parameter h .

selection rule of this bandwidth is given by

$$\hat{h} = \left[\frac{243 R(K)}{35 \mu_2(K)^2 n} \right]^{1/5} \hat{\sigma},$$

where $R(K) = \int K(t)^2 dt$, $\mu_2(K) = \int t^2 K(t) dt$, and $\hat{\sigma} = \text{med}_j\{|X_j - \text{med}_i\{X_i\}|\}$ is the median absolute deviation. The effect of the bandwidth parameter h is illustrated in Figure 6.7.

Hence to each 3D object represented by a triangle mesh M , we associate a kernel density \hat{p} which we will refer to as a *geodesic shape distribution*, and it is computed using the algorithm depicted in Figure 6.8. This probabilistic shape descriptor represents an object information and will be used in our matching experiments. Figure 6.9 depicts a 3D model of a tank and its geodesic shape distribution.

6.4.3 Properties of geodesic shape signature

In addition to its rotational, translational and scale invariance, the geodesic shape signature is also robust to resampling and simplification as illustrated in Figures 6.10 and 6.11. Note that for triangulation, we use the barycentric subdivision shown in the top row of Figure 6.10. This

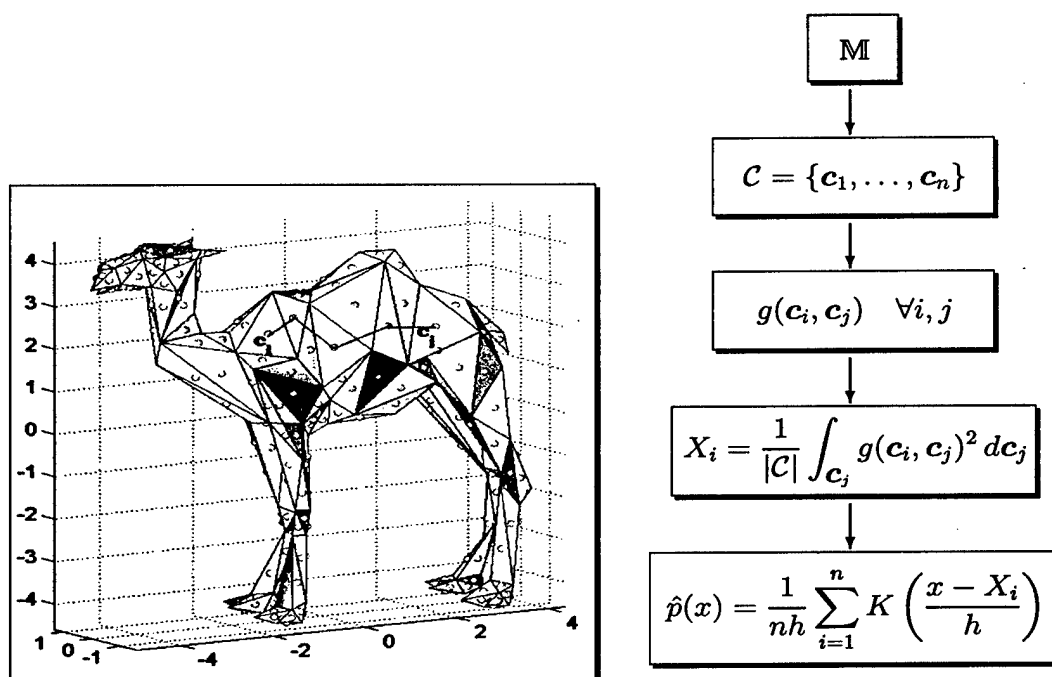


Figure 6.8: Geodesic shape distribution algorithm.

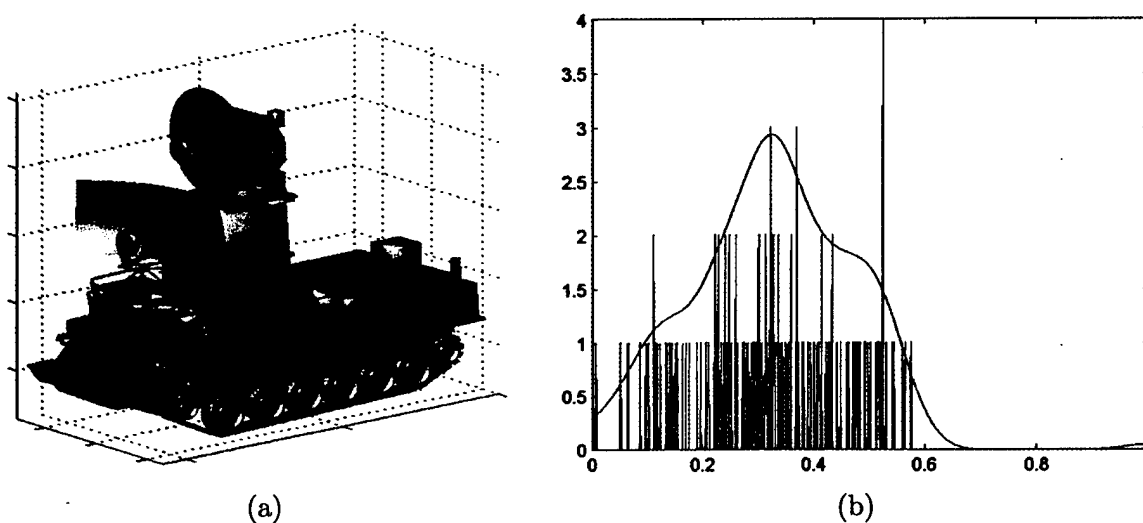


Figure 6.9: (a) 3D tank model, and its (b) geodesic shape distribution.

subdivision technique consists of introducing a new vertex at the center of each triangle and a new vertex at the midpoint of each edge and drawing edges from the centroid of the triangle to each of the new midpoint vertices and to the original vertices.

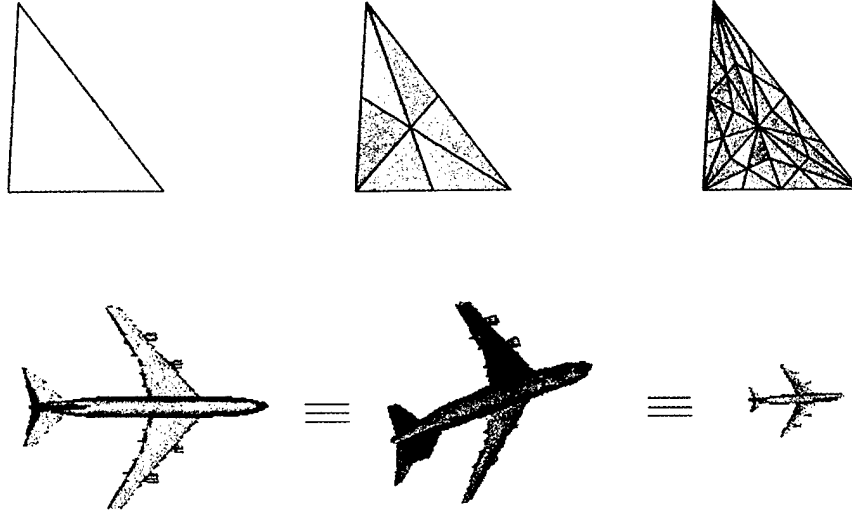


Figure 6.10: Robustness and invariance.

In order to compare two geodesic shape distributions and hence to measure the performance of the proposed scheme, we will describe in the next section an information-theoretic distance that quantifies the difference between two 3D shapes through their probabilistic shape descriptors.

6.5 Probabilistic dissimilarity

Let M_1 and M_2 be two 3D objects with geodesic shape distributions \hat{p} and \hat{q} respectively. Information theoretic measures provide quantitative entropic divergences between two probability distributions. A common entropic dissimilarity measure is Kulback-Liebler (KL) divergence \mathcal{K} defined as

$$\mathcal{K}(\hat{p}, \hat{q}) = \int \hat{p}(x) \log_2 \frac{\hat{p}(x)}{\hat{q}(x)} dx = \mathbb{E} \left\{ \log \frac{p(x)}{q(x)} \right\},$$

where $\mathbb{E}\{\cdot\}$ denotes the expected value with respect to $p(x)$.

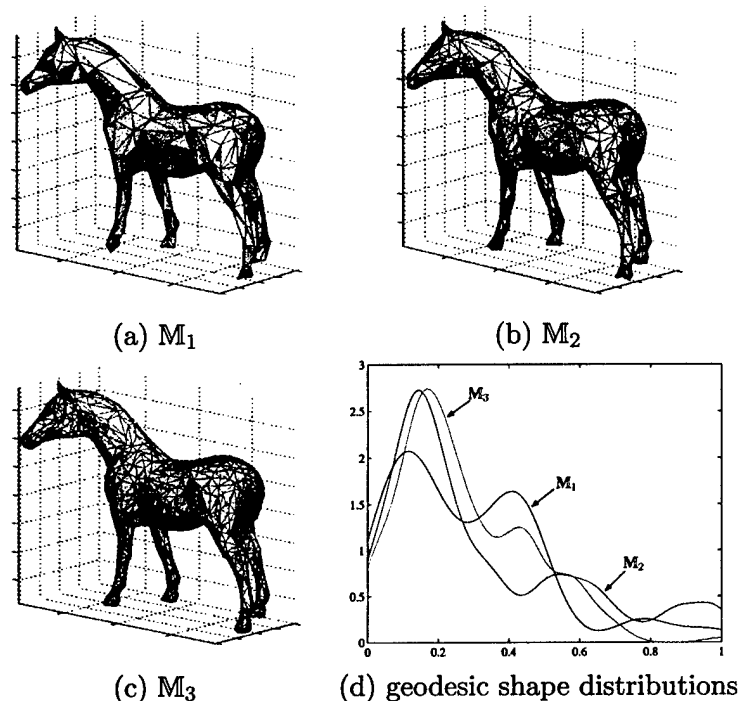


Figure 6.11: Robustness and invariance (cont.).

The KL dissimilarity measure, however, is non-symmetric, unbounded, and undefined if \hat{p} is not absolutely continuous with respect to \hat{q} [37]. To overcome these limitations, we use the Jensen-Shannon divergence D given by

$$\begin{aligned} D(\hat{p}, \hat{q}) &= \frac{1}{2} \left[\mathcal{K} \left(\hat{p}, \frac{\hat{p} + \hat{q}}{2} \right) + \mathcal{K} \left(\hat{q}, \frac{\hat{p} + \hat{q}}{2} \right) \right] \\ &= H \left(\frac{\hat{p} + \hat{q}}{2} \right) - \frac{H(\hat{p}) + H(\hat{q})}{2}, \end{aligned}$$

where $H(\hat{p}) = -\int \hat{p}(x) \log_2 \hat{p}(x) dx$ is the differential entropy, which corresponds to Shannon's entropy in the discrete domain. Shannon's entropy is a measure of uncertainty, dispersion, information, and randomness. The maximum uncertainty or equivalently minimum information is achieved by the uniform distribution. Hence, we can think of the entropy as a measure of uniformity of a probability distribution. Consequently, when uncertainty is higher it becomes more difficult to predict the outcome of a draw from a probability distribution.

The Jensen-Shannon divergence is a statistical distance that is very useful in quantifying differences between probability distributions or densities. In other words, this dissimilarity measure quantifies differences in shape between two arbitrary objects. Unlike the Kullback-Leibler divergence, the Jensen-Rényi divergence has the advantage of being symmetric, always defined, and generalizable to any arbitrary number of probability distributions, with a possibility of assigning weights to these distributions [51]. Figure 6.12 shows a three-dimensional graph and a contour plot of the Jensen-Shannon divergence between two discrete Bernoulli distributions.

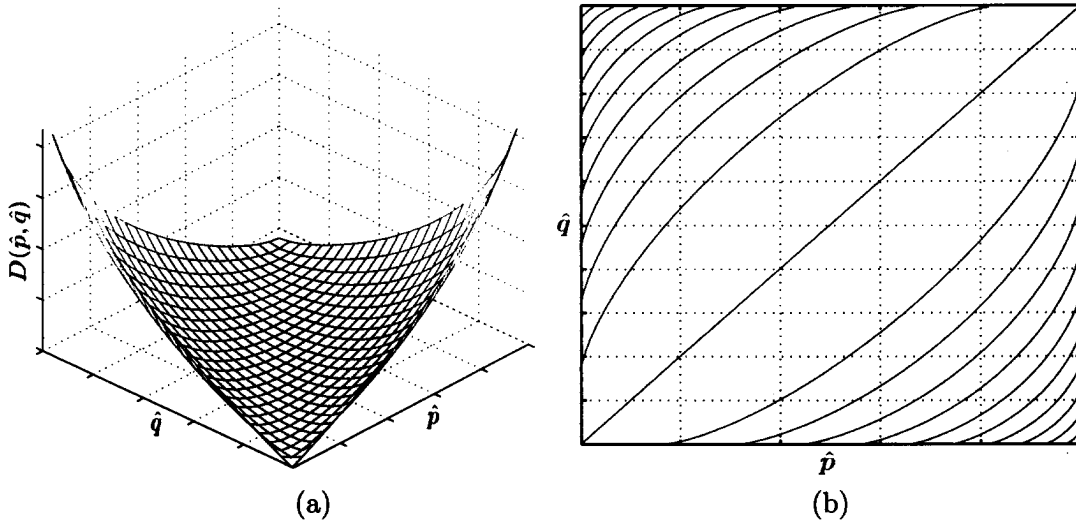


Figure 6.12: (a) 3D plot and (b) contour plot of the Jensen-Shannon divergence.

The following result establishes the convexity of the Jensen-Shannon divergence.

Proposition 6.1 *The Jensen-Shannon divergence $D(\hat{p}, \hat{q})$ is a convex function of \hat{p} and \hat{q} .*

In addition to its convexity property, the Jensen-Shannon divergence is shown to be an adapted measure of disparity among probability distributions. Using the theory of majorization, it can be shown that the Jensen-Shannon divergence is bounded, and its upper bound is achievable.

Proposition 6.2 *The Jensen-Shannon divergence between two geodesic shape distributions \hat{p} and*

\hat{q} is upper bounded

$$D(\hat{p}, \hat{q}) \leq \log_2(2) = 1.$$

6.6 Information-geometric approach to geodesic shape distributions

The Jensen-Shannon divergence

$$D(p, q) = \frac{1}{2} \left[\mathcal{K} \left(p, \frac{p+q}{2} \right) + \mathcal{K} \left(q, \frac{p+q}{2} \right) \right]$$

satisfies the triangle inequality property

$$D(p_1, p_2) + D(p_2, p_3) \geq D(p_1, p_3)$$

if and only if

$$H \left(\frac{p_1 + p_2}{2} \right) + H \left(\frac{p_2 + p_3}{2} \right) \geq H \left(\frac{p_1 + p_3}{2} \right) + H(p_2)$$

While the Jensen-Shannon divergence is not a metric, it can be shown that its square root $\sqrt{D(\cdot, \cdot)}$ is a metric between probability distributions.

6.6.1 Statistical manifolds

A Riemannian manifold is a differentiable manifold equipped with a positive definite inner product $\langle \cdot, \cdot \rangle_{\mathbf{x}}: T_{\mathbf{x}}\mathcal{M} \times T_{\mathbf{x}}\mathcal{M} \rightarrow \mathbb{R}$. The collection of all these inner products is called the Riemannian metric. An example of such a metric is the first fundamental form derived in the Appendix.

Statistical Manifolds are differentiable manifolds such that each point can be identified with a probability density with respect to a given measure, and a family of distributions correspond to a set of points which form a manifold. The theory of statistical manifolds also called *information geometry* was originally proposed by Rao [63] who considered a parametrized statistical model as a Riemannian manifold with the metric tensor given by the Fisher information metric. This metric defines a notion of a distance between two probability distributions. In other words, it measures “how far apart are these distributions?”. A good reference to information geometry is the book by Amari [19] who introduced α -connections and showed how they relate to asymptotic inference.

Let \mathcal{M} be a differentiable manifold representing a statistical model $\mathcal{M} = \{p(x; \theta) : \theta \in \Theta\}$ of probability distributions $p(x; \theta)$ parametrized by a real-valued vector θ . In other words, \mathcal{M} is a parametric surface which can be represented as a Monge patch defined by $\mathbf{r} : \Theta \rightarrow \mathcal{M}$ such that $\mathbf{r}(\theta) = (\theta, p(x; \theta))$. Note that the patch \mathbf{r} covers all \mathcal{M} , that is, $\mathbf{r}(\Theta) = \mathcal{M}$. It is worth pointing out that the Monge patch $\mathbf{r} : \Theta \rightarrow \mathcal{M}$ of a smooth probability density $p(x; \cdot) : \Theta \rightarrow \mathbb{R}$ is a diffeomorphism because it is a smooth bijection, and its inverse \mathbf{r}^{-1} is the restriction to \mathcal{M} of the smooth projection $\pi : \Theta \times \mathbb{R} \rightarrow \Theta$, that is $\mathbf{r}^{-1} = \pi|_{\mathcal{M}}$.

The Kullback-Leibler divergence two points $p(x; \theta)$ and $p(x; \theta')$ in \mathcal{M} is given by

$$\mathcal{K}(\theta, \theta') = \int p(x; \theta) \log \frac{p(x; \theta)}{p(x; \theta')} dx = \mathbb{E} \left\{ \log \frac{p(x; \theta)}{p(x; \theta')} \right\},$$

where $\mathbb{E}\{\cdot\}$ denotes the expected value with respect to $p(x; \theta)$.

When θ and θ' are infinitesimally close to each other (i.e. $\theta' = \theta + \epsilon$ with ϵ sufficiently small), it can be shown that

$$\mathcal{K}(\theta, \theta') = \frac{1}{2} (\theta' - \theta)^T \Sigma(\theta) (\theta' - \theta) + \mathcal{O}(\|\theta' - \theta\|^3),$$

where $\Sigma(\theta) = (\sigma_{ij}(\theta))$ is the Fisher information metric tensor given by

$$\sigma_{ij}(\theta) = \int p(x; \theta) \partial_i \log p(x; \theta) \partial_j \log p(x; \theta) dx = \mathbb{E} \{ \partial_i \log p(x; \theta) \partial_j \log p(x; \theta) \},$$

and $\partial_i \log p(x; \theta)$ denotes the partial derivative with respect to the i -th component of the vector θ .

6.6.2 Geodesic shape manifold

Let $\mathbb{M} = (\mathcal{V}, \mathcal{T})$ be a triangle mesh, where $\mathcal{V} = \{v_1, \dots, v_m\}$ is the set of vertices, and $\mathcal{T} = \{T_1, \dots, T_n\}$ is the set of triangles. Denote by α the total area of the triangle mesh, that is $\alpha = \sum_{j=1}^n \text{area}(T_j)$.

To apply information geometry to our proposed geodesic shape distribution and using Equation (4), we may rewrite the geodesic kernel density in parametric form as

$$p(x; \theta) = \frac{1}{nh} \sum_{i=1}^n K \left(\frac{x - X_i}{h} \right) = \frac{1}{nh} \sum_{i=1}^n K \left(\frac{1}{h} \left(x - \frac{(Ga)_i}{\alpha} \right) \right),$$

where $\theta = (n, \alpha)$ defines the distribution parameters: the number of triangles n and the surface total area α . The 3D object matching by the information geometric approach may be stated as follows: Given a database of 3D models $\{\mathcal{M}_1, \mathcal{M}_2, \dots, \mathcal{M}_\ell\}$, the first step is to compute the corresponding parametrized probability shape distributions $\{p(x; \theta_1), p(x; \theta_2), \dots, p(x; \theta_\ell)\}$, that is each 3D model can be viewed as a point in a set $\mathcal{S} = \{p(x; \theta) : \theta \in \mathbb{N} \times \mathbb{R}_+\}$ embedded in the 3D Euclidean space as displayed in Figure 6.13. This set \mathcal{S} of geodesic shape distributions forms a statistical model that carries the structure of a smooth manifold, and will be referred to as geodesic shape manifold. Note that the parameter $\theta = (n, \alpha)$ plays the role of coordinates of a geodesic shape density $p(x; \theta) \in \mathcal{S}$.

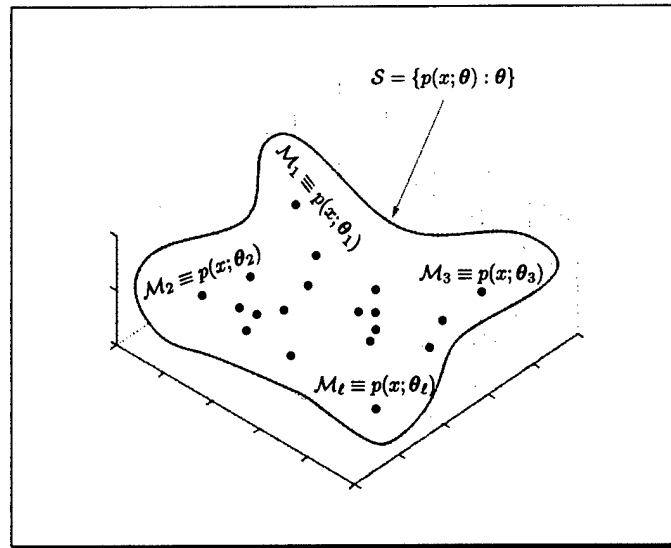


Figure 6.13: Illustration of geodesic shape statistical manifold.

6.7 Experimental results

Object matching experiments were performed using a database of 3D models collected online. Each model is represented as a triangle mesh. We conducted four sets of experiments. The first set consists of 3D airplane models as shown in Figure 6.14, and the second set consists of 3D tanks as

illustrated in Figure 6.15.

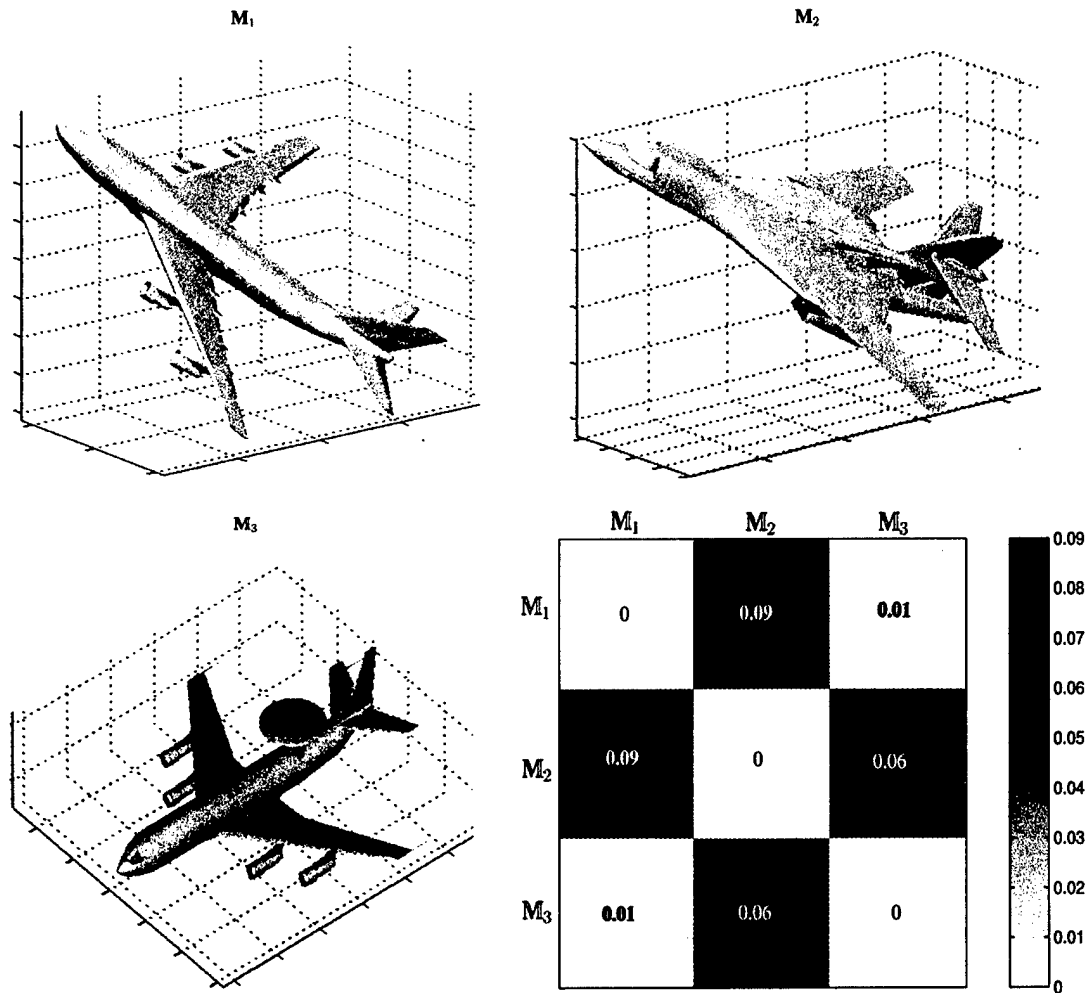


Figure 6.14: First set of experiments: 3D airplanes.

The third set deals with objects that are topologically equivalent to a sphere (i.e. with genus equal to zero) as shown in Figure 6.16. The numerical results using the Jensen-Shanon dissimilarity measure are depicted in Table 6.1 where the grayscale colorbar displays the grayscale colormap of this dissimilarity matrix. This grayscale colormap ranges from white (maximum similarity) to black (maximum dissimilarity), and passes through the gray colors indicating the values of the matching

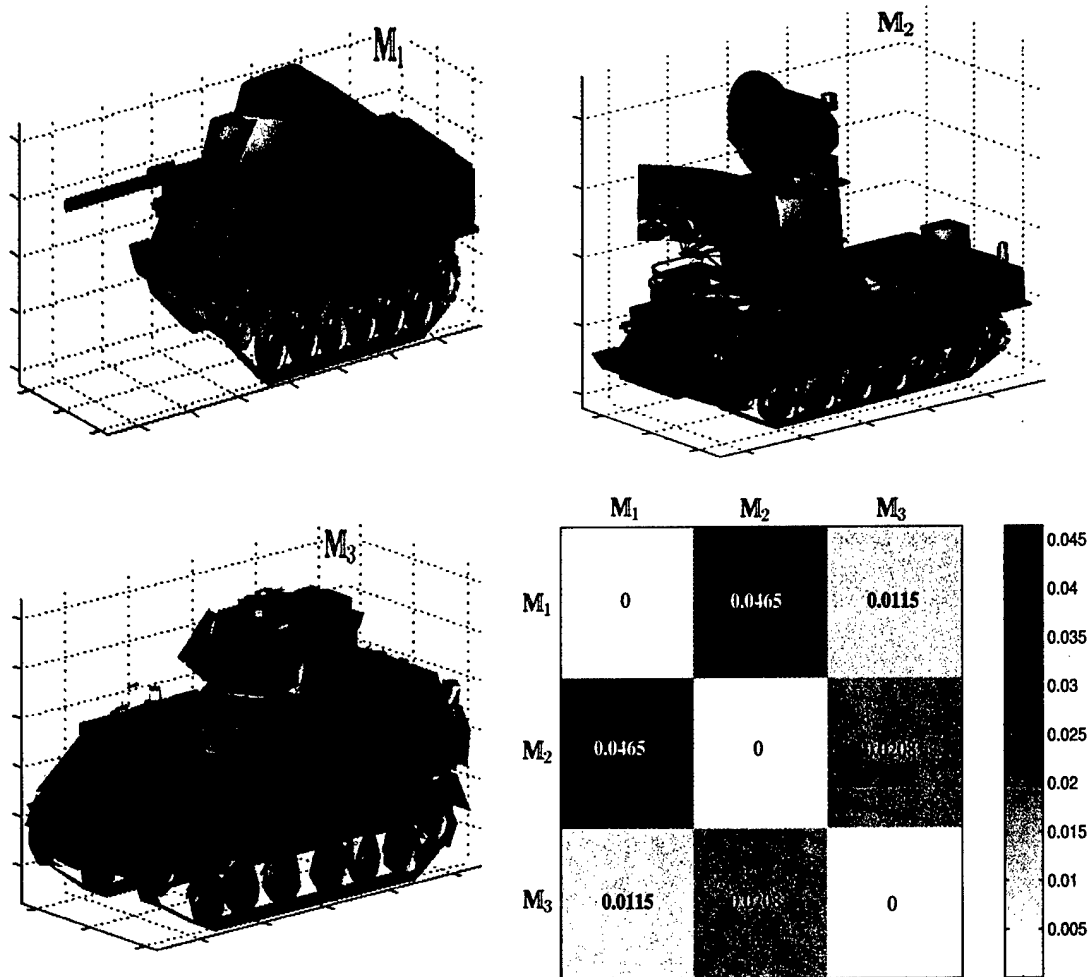


Figure 6.15: Second set of experiments: 3D tanks.

algorithm. Note that the minimum dissimilarity rate is about 9%, that is the matching rate is about 81%.

The fourth set of experiments is similar to the third, except that the underlying objects are topologically different from than the ones in the third set of the experiments. Figure 6.17 shows a set of objects with genus equal to one. Matching is achieved by the minimum Jensen-Shannon distance computations as illustrated in Table 6.2. Note that the minimum dissimilarity rate is

about 2%, that is the matching rate is about 98%.

[h!]

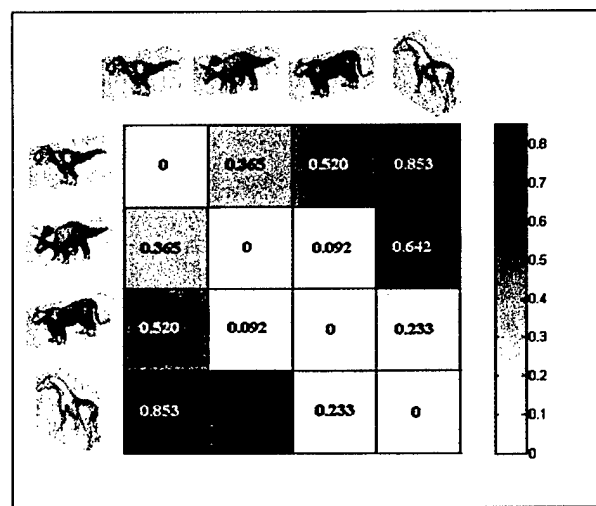


Table 6.1: Jensen-Shannon dissimilarity results for the third set of experiments.

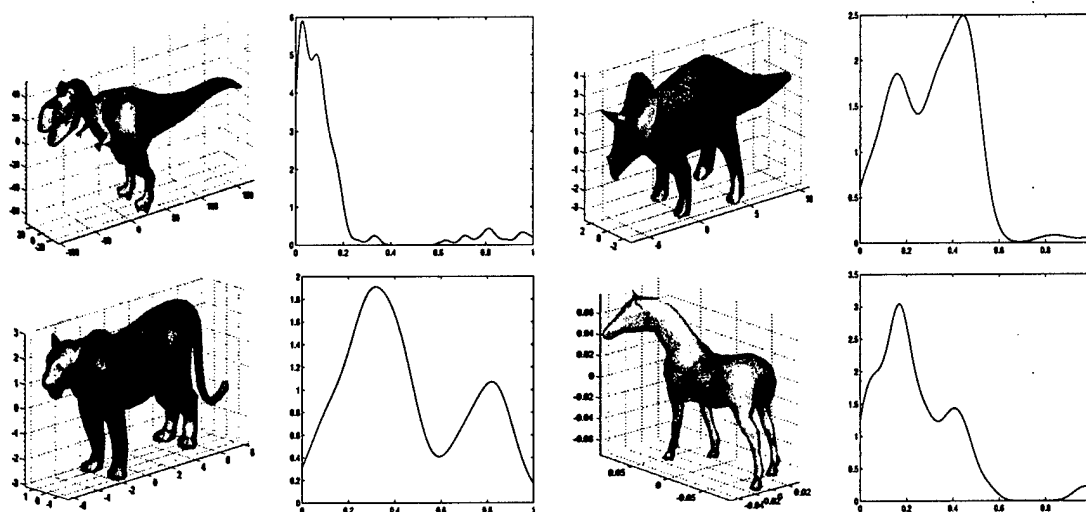


Figure 6.16: Third set of experiments: 3D models and their geodesic shape distributions.

[h!]

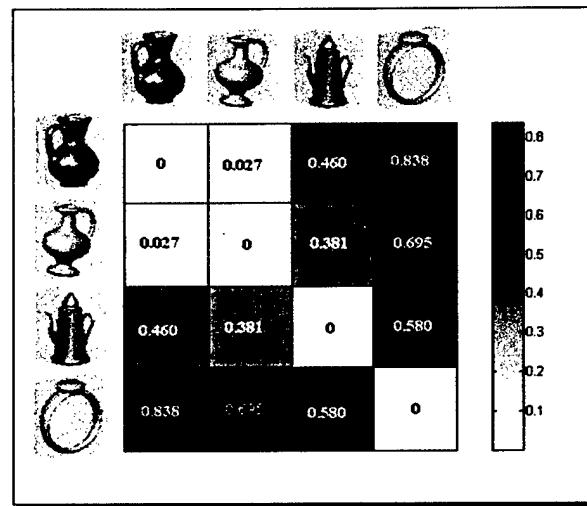


Table 6.2: Jensen-Shannon dissimilarity results for the fourth set of experiments.

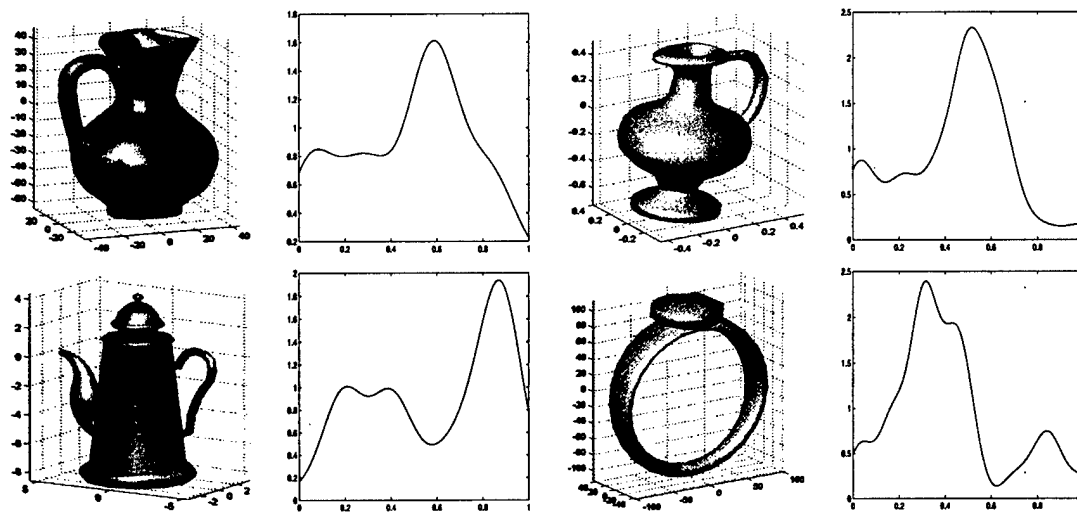


Figure 6.17: Fourth set of experiments: 3D models and their geodesic shape distributions.

6.8 Conclusions

In this Chapter, we proposed an new methodology for object matching. The key idea is to encode a 3D shape into a 1D geodesic shape distribution. Object matching is then achieved by calculating an information-theoretic measure of dissimilarity between the probability distributions. That is, the dissimilarity computations are carried out in a low-dimensional space of geodesic shape distributions. The main advantages of the proposed approach are:

- The geodesic distance captures the intrinsic geometry of the data
- The approach is simple and computationally inexpensive
- The simulations results indicate the suitability of the proposed technique for object matching

For future work, it would be of interest to incorporate topology into the proposed methodology through Morse singularities of the global geodesic shape function. Finally we note that while the experimental results presented in this section are very promising, significant additional performance gains are still possible. For example, our current way of selecting centroids as landmarks is rather one of many possible options and by no means the best option, and a multiresolution geodesic shape distribution may also provide better key to landmarks.

Distance Function-based Object Recognition

In this Chapter we propose a distance function-based approach to topological modeling of 3D objects. Despite the theoretical nature of the results presented in this Chapter, the key idea is to identify and encode regions of topological interest of a 3D object in the Morse-theoretic framework. The main motivation behind using the distance function is its rotational invariance which makes it more adapted to object recognition than the Morse height function. We prove that a surface may be reconstructed from its intersections with concentric spheres centered at the barycenter of the underlying surface. The topological changes in the surface occur as we increase the value of the sphere radius. At singular points, the level curves of the distance function may split or merge which indicate topological changes. We also show that when a surface is embedded in a sphere, the height function and the distance function are equivalent in a Morse-theoretic setting, that is both functions have the same singularities.

7.1 Introduction

In computer graphics applications, one is typically interested in locating geometric regions of topological nature on a surface. The simplest non-trivial regions are areas with genus equal to one. Such regions are *handles*. As mentioned in Chapter 1, a handle intuitively corresponds to its definition per se. For example, a coffee mug with a handle has genus equal to one. Our challenge in this research effort is to present computational topology algorithms which are adapted to discrete surfaces and which simultaneously account for the geometry of a surface. The main objectives of

this chapter consist of:

- identifying regions of topological interest, that is where topology changes on a surface occur. Identifying the topology of a surface is tightly related to Morse theory which establishes a relationship of critical points of a smooth function defined on a smooth manifold to its connectivity.
- coding a surface topology into a Reeb graph. The nodes of this graph represent the critical points of a function defined on the surface, and the edges in the graph represent the connected components of the surface between critical points.

7.2 Topology identification

Topology is a branch of mathematics dealing with qualitative questions about geometrical structures. We do not ask: how big is it? but rather: does it have any holes in it? Is it all connected together, or can it be separated into parts? Geometry, on the other hand, deals with measuring and computing lengths, areas, volumes, angles etc., and that is actually where the word “geo-metry” comes from. The subject of topology is concerned with those features of geometry which remain unchanged after twisting, stretching or other deformations of a geometrical space. It includes such problems as distinguishing knots and classifying surfaces. One of the key tools used to study the topology of spaces is Morse theory which is the study of the relationship between functions on a space and the shape of the space. Although Morse theory can be applied to spaces of infinite dimension, we are particularly interested in the application of Morse theory to 2-manifolds. Based on the calculus of variations, Morse theory draws a relationship between critical points of a smooth function defined on a smooth manifold and the global topology of that manifold. To better understand Morse theory, we start by briefly introducing some basic definitions in differential geometry and topology.

Definition 7.1 *An abstract surface or 2-manifold is a topological space M such that each point of M has a neighborhood U in M homeomorphic to an open 2-disk D^2 in \mathbb{R}^2 .*

In other words, a 2-manifold is locally homeomorphic to an open disk D^2 . Homeomorphism is a continuous function defined between two spaces which is bijective and also has a continuous inverse.

If M is a 2-manifold, then we can find a countable system of open sets U_i and homeomorphisms $\varphi_i : U_i \rightarrow D^2$ such that $M = \cup_i U_i$. This homeomorphism is illustrated in Figure 7.1. A collection of charts is called an *atlas*. A 2-manifold M may be embedded in \mathbb{R}^3 meaning that it has no self-intersections.

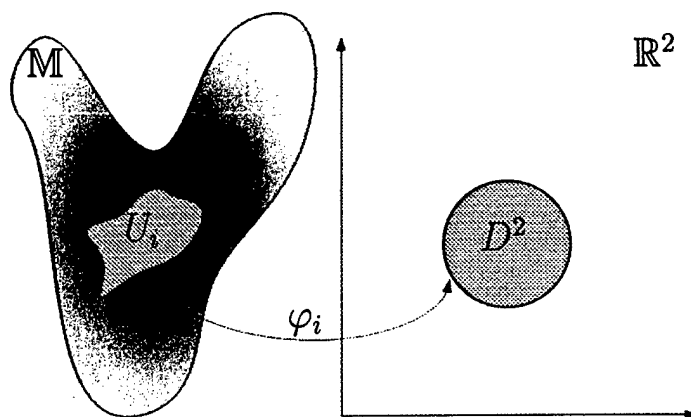


Figure 7.1: Definition of a 2-manifold.

A 2-manifold is a surface where the local area around every point on the surface is Euclidean, meaning, around each point the surface appears to be nearly flat. The world around us is an excellent example of a 2-manifold. Manifolds are a preferable surface representation because the surface can be divided into charts which allow 2-manifolds embedded in 3D to be flattened into a two dimensional domain (through parametrization). Surfaces used in computer graphics are typically oriented, this refers to the fact that the surface has two sides. For example, a sphere has two sides, while a Mobius strip has only one side. Another attribute of surfaces is whether the surface is closed or with boundary. This refers to the number of open boundary components of a surface. For example, an egg shell is closed but once it has been cracked open, it becomes a surface with boundaries.

We refer to a *surface* as a smooth and compact 2-manifold without boundary and possibly embedded in the Euclidean space \mathbb{R}^3 . Mathematically, surfaces are often conceived of as continuous and smooth, i.e., one that has a sufficient number of partial derivatives. Smooth often refers to a surface with infinitely many partial derivatives, but in practice second-order derivatives are sufficient. In computer graphics we operate in a discrete setting, where only a finite number of samples are used to represent a surface. These surfaces are often continuous, but are only piecewise linear and are represented only by a discrete set of points which are connected together as triangles or polygons.

7.2.1 Singular points

Let $\varphi : M \rightarrow \mathbb{R}$ be a real-valued function defined on a smooth manifold $M \subset \mathbb{R}^3$. The function φ is smooth if the composition function $\varphi \circ \mu : U \rightarrow \mathbb{R}$ is smooth (in the ordinary Euclidean sense), where μ is a smooth regular parametrization of M (i.e. $\mu : U \subset \mathbb{R}^2 \rightarrow \mathbb{R}^3$). A point p_0 on M is a singularity or critical point of φ if $p_0 = \mu(x_0, y_0)$, for some $(x_0, y_0) \in U$, and the gradient of $\varphi \circ \mu$ at (x_0, y_0) vanishes, i.e. $\nabla(\varphi \circ \mu(x_0, y_0)) = 0$.

A singularity p_0 is nondegenerate if the Hessian matrix $\nabla^2(\varphi \circ \mu(x_0, y_0))$ is nonsingular. Otherwise this singularity p_0 is said to be degenerate.

7.2.2 Morse function

Morse theory explains the presence and the stability of critical points in terms of the topology of an underlying smooth manifold. Topology is the property that determines which parts of an object are connected to which other parts [38], while geometry determines where, in a given coordinate system, each part is located [29]. The basic principle is that the topology of a manifold is very closely related to the critical points of a smooth function on that manifold.

Morse proved a major result which generalizes the straightforward result that the lowest-order nonvanishing term in a Taylor series describes the local behavior of a smooth function of a single variable to functions of many variables.

Definition 7.2 A smooth function $\varphi : M \rightarrow \mathbb{R}$ on a smooth manifold M is called a *Morse function*

if all its singularities are nondegenerate.

Examples of nondegenerate singular points are shown in Figure 7.2.

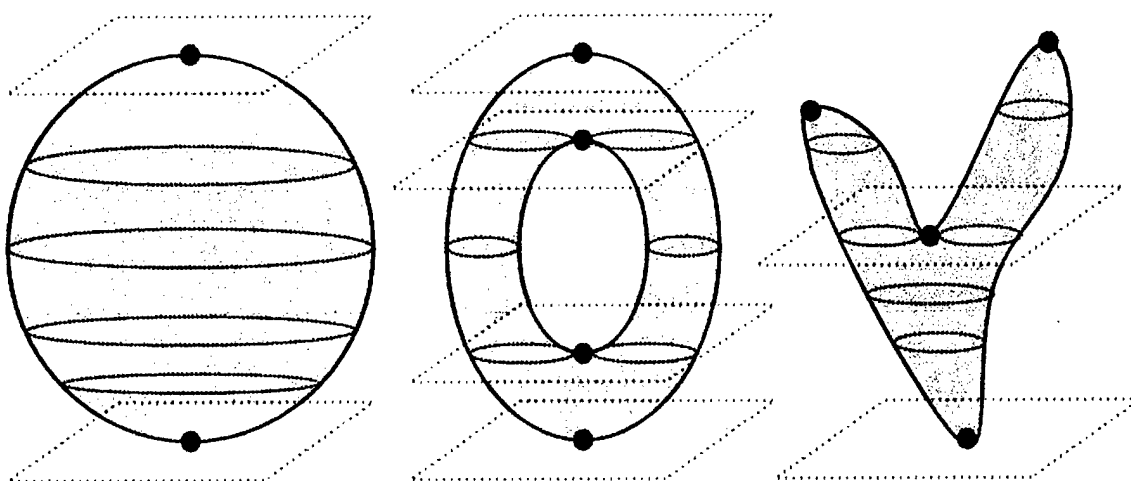


Figure 7.2: Critical points.

Nondegenerate singularities are isolated, that is, there cannot be a sequence of nondegenerate singularities converging to a nondegenerate singularity p . In other words, there is no other point in the neighborhood of p that is singular. This fact follows from the following Morse's lemma.

Lemma 7.3 *If $\varphi : M \rightarrow \mathbb{R}$ has a nondegenerate singularity at $p_0 \in M$, then there exists $(x_0, y_0) \in \Omega$ such that $p_0 = r(x_0, y_0)$, and φ has the following representation*

$$\varphi(p) = \varphi \circ r(x_0, y_0) \pm x^2 \pm y^2 = \varphi(p_0) \pm x^2 \pm y^2,$$

for all $p = r(x, y) \in M$, where r is a regular smooth path.

Note that the only nondegenerate singularities are the minimum, maximum and saddle points. By decomposing a smooth manifold along these singularities, its global shape and topology is revealed. Morse theory also presents methods to classify critical points. Specifically, by examining the number of negative eigenvalues of the Hessian, the critical point can be indexed. That is, a minimum has zero negative eigenvalues, a saddle point has one, and a maximum has two negative eigenvalues.

This analysis corresponds to the fact that a minimum has no downhill sides, while an isolated saddle point has two downhill sides, one parallel to the direction of the eigenvector associated with the negative eigenvalue and one anti-parallel. A maximum has downhill sides associated with both directions of both eigenvectors.

7.2.3 Sard's theorem

Let $f : \mathbb{M} \rightarrow \mathbb{R}$ be a smooth function. A point \mathbf{p} is called a *regular point* of f if the differential $df : T_{\mathbf{p}}\mathbb{M} \rightarrow \mathbb{R}$ is *surjective*, that is, the Jacobian matrix (3×1 in this case) has rank equal to $\dim(\mathbb{R}) = 1$. Otherwise, the point \mathbf{p} is called a *critical point*. Denote by $\text{Crit}(f)$ the set of critical points of f .

Theorem 7.4 (Sard) *The set $f(\text{Crit}(f))$ of critical values of f has measure zero in \mathbb{R} (in the sense of Lebesgue measure).*

Corollary 7.5 *The set $\mathbb{R} - f(\text{Crit}(f))$ of regular values of f is dense in \mathbb{R} .*

Note: f can be defined between two smooth manifolds with arbitrary dimensions, i.e., $f : \mathbb{M} \rightarrow \tilde{\mathbb{M}}$.

Definition 7.6 *A smooth map $f : \mathbb{M} \rightarrow \tilde{\mathbb{M}}$ is called an immersion if at any point $\mathbf{p} \in \mathbb{M}$, the differential $df : T_{\mathbf{p}}\mathbb{M} \rightarrow T_{f(\mathbf{p})}\tilde{\mathbb{M}}$ is injective, i.e., no nonzero vector maps to zero. If, moreover, f is a homeomorphism when considered as a map from \mathbb{M} to $f(\mathbb{M})$, we say that f is an embedding.*

7.2.4 Height function

A classic result from Morse theory is that given a closed surface \mathbb{M} and a Morse function $f : \mathbb{M} \rightarrow \mathbb{R}$, we can show that if this function has only two non-degenerate critical points then \mathbb{M} is topologically equivalent to a sphere. For example, a typical Morse function is a height function, and if we consider such a function defined on a sphere, we can identify two critical points which corresponding to the maximum and minimum at the north and south pole of the sphere (see Figure 7.2). More precisely,

the the Euler characteristic of a surface is defined in terms of the number of critical points as follows:

$$\chi = \#minima - \#saddlepoints + \#maxima.$$

Another essential result from Morse theory shows that between critical points the topology of the manifold is guaranteed not to change (called the *deformation lemma*).

To further illustrate the relationship of critical points and the global topology of a surface, consider the following geometric interpretation. Given a Morse function, $f : M \rightarrow \mathbb{R}$ which is a height function which may, for example, define parallel planes. A height function in the z -direction on a smooth manifold M is a real-valued function $h : M \rightarrow \mathbb{R}$ such that $h(x, y, z) = z$ for all $(x, y, z) \in M$. Hence, h is the orthogonal projection with respect to the z -axis. Figure 7.3 shows a 2D manifold (a double torus) and the corresponding critical points of its height function. These singular points are all nondegenerate.

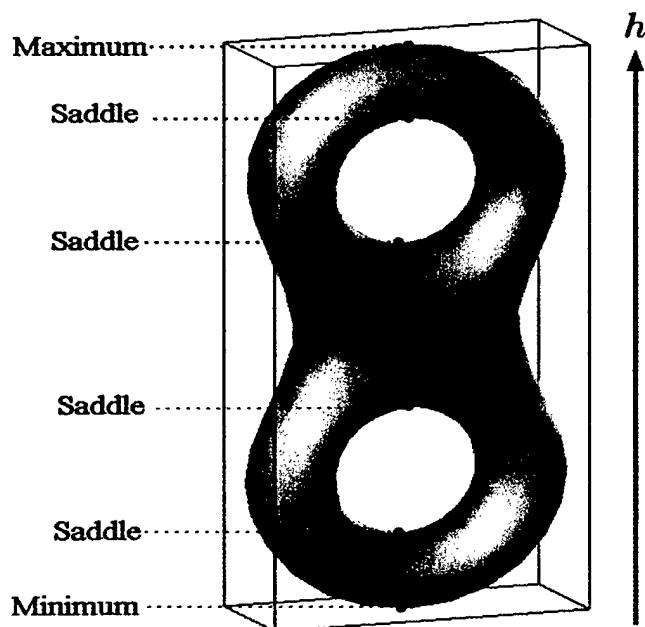


Figure 7.3: A 3-D object and the critical points of its height function.

Now imagine a torus standing on its end (see Figure 7.2). When considering each of the tangent planes to the torus, the critical points may be identified as those at which tangent planes coincide with height planes of the Morse function. For example the torus, as we expected there will be critical points corresponding to the maximum and minimum (at the north and south poles of the torus) and the two saddle points at the handle.

There is further geometric interpretation of Morse theory for a 2-manifold by correlating the tangent plane of the surface at each point to the planes defined by a height function. Specifically, we consider classifying critical points and trivial points (non-critical points). Similar to the method presented above, where we classify points based on their shape, we consider analyzing the local shape of the surface, by looking at the relationship between a small circular neighborhood of each point on the surface and the height planes of a height function.

Morse lemma says that near p_0 there is a smooth change of coordinates under which the resulting Taylor series of the Morse function h near p_0 is the pure quadratic function.

Theorem 7.7 *Morse functions are stable and dense in the set of all smooth functions. Equivalently, any smooth function can be converted into a Morse function as a result of a perturbation as slight as desired.*

This Morse's theorem says that a small, smooth perturbation of a Morse function yields another Morse function. The density means that there is a Morse function arbitrarily close to any non-Morse function.

7.2.5 Generalized height function

The height function in the direction of a vector v (we may assume $v \in \mathbb{S}^2$, i.e. $\|v\| = 1$) is defined as $h_v : M \rightarrow \mathbb{R}$ such that $h_v(p) = p \cdot v$.

The level sets of the height function are the intersections of M with planes orthogonal to v (considered as a line) as pictured in Figure 7.4. Denote by \mathbb{P}_z the plane at height z . The original object (surface) can be reconstructed if we know all its sections by these parallel planes (i.e. the surface is the union of these planes).

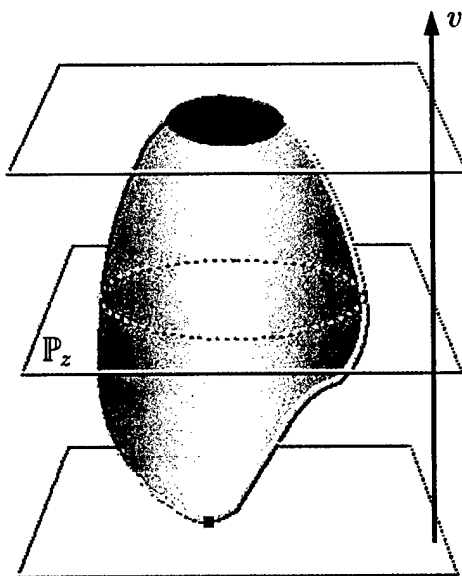


Figure 7.4: Illustration of the height function.

Clearly, the level sets of the height function may have isolated points, or curves, or may contain an open subset of the plane. Furthermore, the level sets may be connected or disconnected, and the curves may have complicated singularities (e.g. generalized Monkey saddle surface).

A point p is a critical point of h if and only if $\bar{g}(p) = \pm v$, where $\pm v$ is the point in $\mathbb{R}P^2$ corresponding to $v \in S^2$, that is, the inverse image $\bar{g}^{-1}(\pm v)$ consists exactly of all points on the surface M whose tangent planes are orthogonal to v . Hence, p is a nondegenerate critical point of h if and only if it is a *regular point* for \bar{g} . Therefore, $\pm v$ is a regular value of \bar{g} if and only if all the critical points of h are nondegenerate.

Proposition 7.8 *The height function $h : M \rightarrow \mathbb{R}$ in the direction of $v \in S^2$ is a Morse function if and only if the corresponding point $\pm v$ is a regular value for the Gauss map $\bar{g} : M \rightarrow \mathbb{R}P^2$.*

Applying Sard's theorem to the map \bar{g} , we conclude that the set of $\pm v$ for which the height function h is not a Morse function has measure zero in $\mathbb{R}P^2$.

7.2.6 Height function and immersion

Defining a height function for a closed 2-manifold and examining its pre-image for various intervals along the z -direction, will create a sequence of closed contours on the surface. This corresponds to placing the closed 2-manifold in a tank and slowly immersing it in liquid up to various heights by adding more and more water to the tank. The level set for a given height z will be the intersection of the surface with the top of the water (see Figure 7.5). We observe that as the surface is immersed in the water, the topology of the level sets change, i.e., the number of components of the level set changes for various heights. For example, imagine we are pouring water into a tank with the surface shown in Figure 7.5. As we first pour water in to level z_0 , we do not intersect the surface and the pre-image of our height function will be empty (it will have no contours). When the water first touches the surface at level z_i , the topology of the level set changes and the pre-image now consists of a single contour. As we continue pouring water into the tank, the topology of the level sets will continue to change. For example, when the water level first reaches a “hole” of one of the handles, the topology of the level set will change from a single contour to two. Finally, consider when we pour in the last of the water and the level set changes such that we once again have no contours. This analogy of immersing a surface in water is often used to describe the process of finding critical points in a surface.

7.3 Topology coding

7.3.1 Reeb graph

An interesting concept related to Morse theory and very useful in analyzing a surface topology is the Reeb graph. The latter is defined as a quotient space M/\sim with an equivalence relation given by $p \sim q$ if and only if $h(p) = h(q)$ and p, q belonging to the same connected component of $h^{-1}(h(p))$. In particular, each connected component is represented by a point in the Reeb graph as illustrated in Figure 7.6. The left figure shows a torus with the critical points of its height function (Morse function). The figure in the middle illustrates the geometric features of the torus represented by cross-sections along its height. The right figure shows the topological features

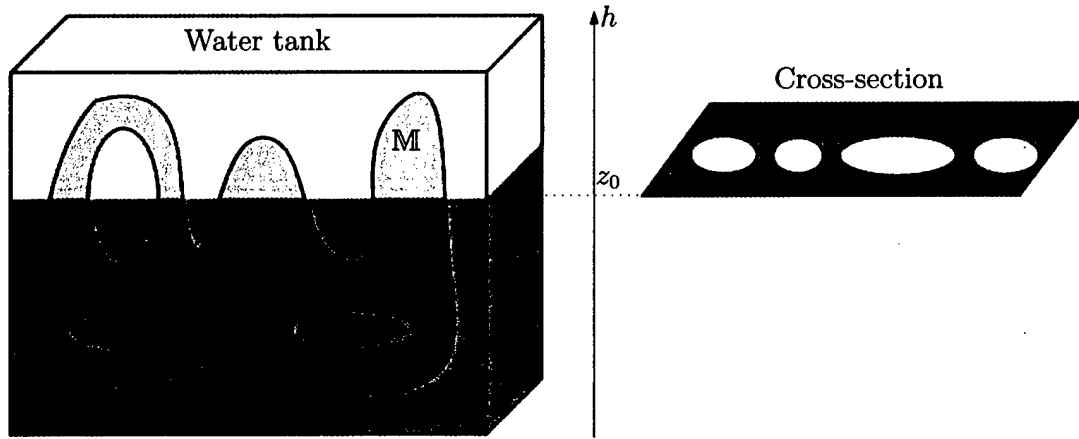


Figure 7.5: Surface immersed in water.

captured by the Reeb graph. By taking an appropriate number of cross-sections and a smooth interpolation in between, Shinagawa *et al.* [67, 68] proposed a Reeb graph based approach or so-called *homotopy model* for object reconstruction. The Reeb graph is a topological representation of an object (skeletal structure), and has storage and transmission advantages due to a parsimonious data representation.

Mathematically, a quotient space $M/\sim = \{[p] : p \in M\}$ is a set of equivalence classes with relation \sim , and where $[p] = \{q \in M : q \sim p\}$ is the equivalence class of $p \in M$. Intuitively, M/\sim is a space created by taking the space M and gluing p to any q that satisfies $q \sim p$. The classes $[p]$ are the connected components for the Reeb graph, and being in the same component is an equivalence relation:

$$q \sim p \iff h(q) = h(p) \text{ and } p, q \in \text{ConComp}\{h^{-1}(h(p))\},$$

where $\text{ConComp}\{\cdot\}$ denotes the connected component. In a Reeb graph representation, each connected component of a contour (i.e. $h^{-1}(z)$ where $z = h(x, y, z)$) corresponds to a point.

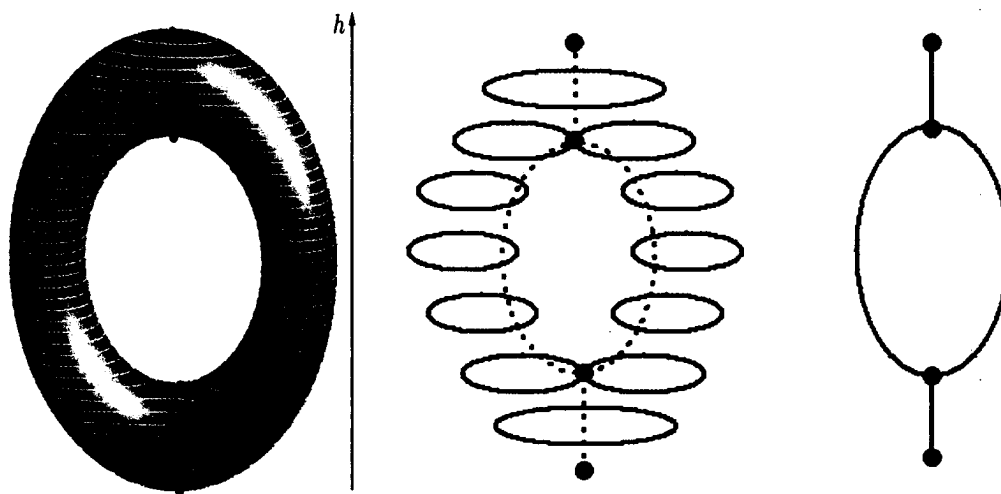


Figure 7.6: Reeb graph representation of a torus.

7.4 Level sets around Morse points

Let $f : M \rightarrow \mathbb{R}$ be a Morse function defined on a compact surface M . The following result shows that a Morse function on a surface may determine the shape of the surface.

Proposition 7.9 *If $f : M \rightarrow \mathbb{R}$ has exactly two nondegenerate singular points, then M is diffeomorphic to the sphere S^2 .*

Denote by M_a the sub-surface of M consisting of all points at which h takes values less than or equal to a real number a

$$M_a = \{p \in M : f(p) \leq a\}$$

and denote by L_a the set of points where the value of h is exactly a , that is $L_a = f^{-1}(a)$. Note that when a is a regular value, the set L_a is a smooth curve of M and it is the boundary of M_a .

Proposition 7.10 *Let $a < b$ be real numbers such that the function $f : M \rightarrow \mathbb{R}$ has no critical value in the interval $[a, b]$, then*

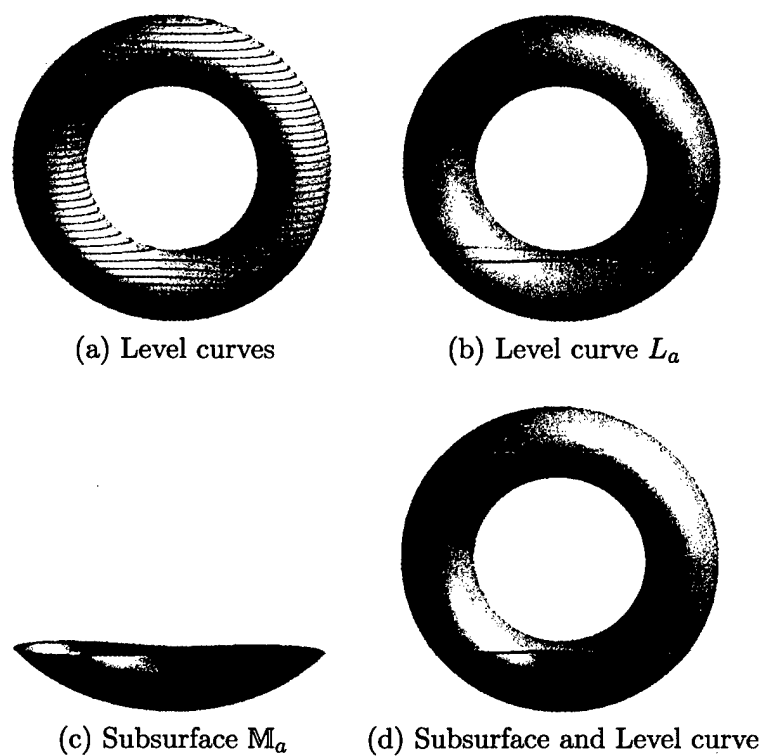
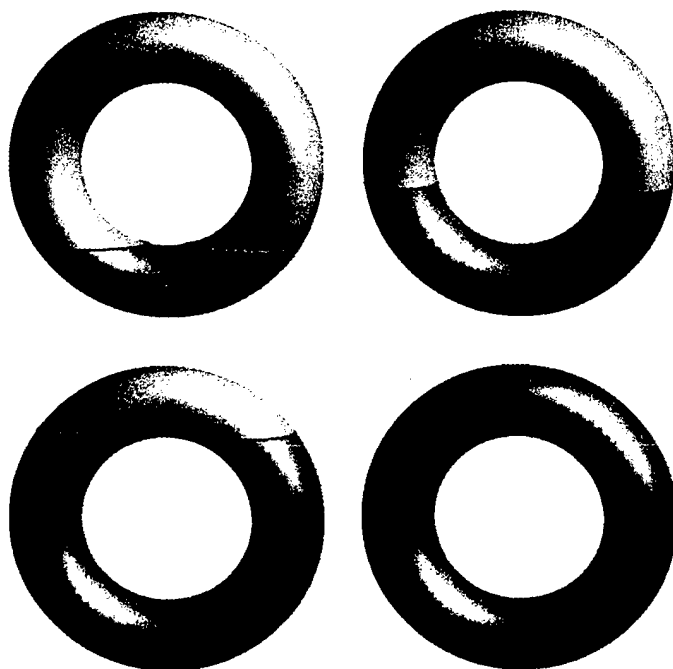


Figure 7.7: Illustration of M_a and L_a .

- (a) The level curves $L_a = f^{-1}(a)$ and $L_b = f^{-1}(b)$ are diffeomorphic.
- (b) The subsurfaces M_a and M_b are diffeomorphic, with boundaries L_a and L_b respectively.

Figure 7.8 shows the evolution of the subsurface M_a as the parameter a changes. If $a < \min_{p \in M} \{f(p)\}$, then $M_a = \emptyset$. And as we increase the parameter a , the subsurface M_a changes until it covers the entire surface M . We may think of the height function $f : M \rightarrow \mathbb{R}$ as dipping a doughnut into a cup of chocolate cream.

Figure 7.8: Evolution of M_a as a changes.

7.4.1 Handle decompositions

Let $f : M \rightarrow \mathbb{R}$ be a Morse function defined on a compact surface M . Each time the value of f passes through a critical value, a handle appears and is attached to the previously built-up subsurface. The index of the handle coincides with the index of the corresponding critical points, that is the number of negative eigenvalues of the Hessian matrix of f . For example, let p_1, p_2, p_3, p_4 be the critical points of a height function $h : T \rightarrow \mathbb{R}$ defined on a torus T , and denote by v_1, v_2, v_3, v_4 their critical values, i.e. $h(p_i) = v_i$ is the z -coordinate of each point p_i . We further assume that these critical values are ordered $v_1 < v_2 < v_3 < v_4$, that is v_1 is the minimum value, v_4 is the maximum value, and v_3, v_4 are the saddle values.

To track the topological changes of the surface M , we look at how M_a changes as the parameter a increases. In the case of a torus, we start from a value less than v_1 , that is for $a < v_1$ we have $M_a = \emptyset$. As soon as a passes v_1 , a 2-disk (upright bowl) pops out and we have $M_a = D^2$. This

2-disk corresponds to the minimum critical point of index 0 and is called *0-handle*. Similarly, a *1-handle* corresponds to a saddle point and a *2-handle* corresponds to a maximum critical point.

Consequently, we deduce that any closed surface can be decomposed into a union of a finite number of 0-, 1-, and 2-handles. In other words, any closed surface admits a handle decomposition.

The diagram depicted in Figure 7.9 shows the sequence of steps in the gradual buildup of a torus, starting with a disk (or 0-handle), adding two consecutive 1-handles, and finally completing the torus with a 2-handle.

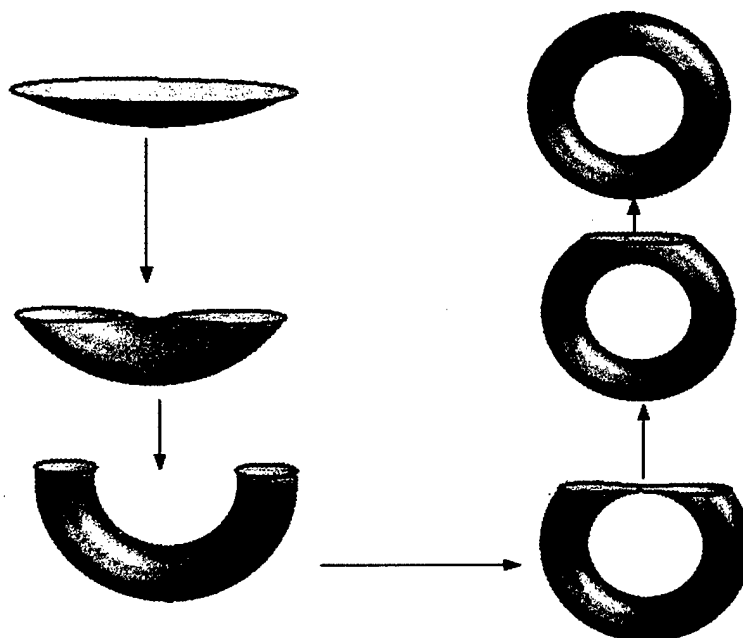


Figure 7.9: handle decomposition.

7.5 Distance function

The concept of distance is central to topology, with the actual numeric values being of less importance. In fact, topologists often use a distance function, but the attributed numerical values have only secondary meaning. To illustrate this, suppose we are given an object in the ordinary

three-dimensional space, and a point outside the object, and the question is: does the object come arbitrarily close to this reference point?. This may be stated as: is the point a boundary point of the object? "Arbitrarily close" means that if one imagines a ball around the reference point, then the ball contains some points belonging to the object no matter how small the ball is. The actual distances between the points belonging to the object and the reference point do not matter, and there just have to be arbitrarily small values among them.

The distance function is a function which has nondegenerate critical points, and it can be shown that almost all distance functions are Morse functions. In fact, for fixed $\mathbf{v} \in \mathbb{R}^3$, we may define a distance function of \mathbb{M} to \mathbf{v} as $d_{\mathbf{v}} : \mathbb{M} \rightarrow \mathbb{R}$ such that $d_{\mathbf{v}}(\mathbf{p}) = \|\mathbf{p} - \mathbf{v}\|^2$.

If a surface \mathbb{M} is given in parametric form $\mathbf{r}(x, y)$ where $\{x, y\}$ is the coordinate system, then the distance function may be expressed as $d_{\mathbf{v}}(\mathbf{r}(x, y)) = \|\mathbf{r}(x, y) - \mathbf{v}\|^2$. The first partial derivatives are given by $d_x = 2\mathbf{r}_x \cdot (\mathbf{r}(x, y) - \mathbf{v})$ and $d_y = 2\mathbf{r}_y \cdot (\mathbf{r}(x, y) - \mathbf{v})$. Hence d has a critical point at $\mathbf{p} = \mathbf{r}(x, y)$ if and only if $\mathbf{v} - \mathbf{p}$ is orthogonal to \mathbb{M} at \mathbf{p} , i.e. $\mathbf{v} - \mathbf{r}(x, y)$ is parallel to the surface normal \mathbf{N} . Thus $\mathbf{v} = \mathbf{r}(x, y) + a\mathbf{N}$.

The distance function from the origin of a coordinate system is given by $d(x, y) = \|\mathbf{r}(x, y)\|^2 = x^2 + y^2 + u(x, y)^2$. Its gradient is $\nabla d(x, y) = 2[(x, y) + u(x, y)\nabla u(x, y)]$, and its Hessian matrix is $\nabla^2 u(x, y) = 2[(1 + \|\nabla u(x, y)\|^2)I_2 + u(x, y)(\nabla^2 u(x, y))]$, where I_2 is the 2×2 identity matrix. The second partial derivatives at a critical point can be easily derived as

$$d_{xx} = 2(\mathbf{r}_x \cdot \mathbf{r}_x + \mathbf{r}_{xx} \cdot (\mathbf{r}(x, y) - \mathbf{v})) = 2(\mathbf{r}_x \cdot \mathbf{r}_x - a\mathbf{r}_{xx} \cdot \mathbf{N}).$$

Hence, the Hessian matrix may be expressed in terms of the first and second fundamental forms as follows

$$\nabla^2 d = 2(\mathbf{I} - a\mathbf{II}),$$

where \mathbf{I} and \mathbf{II} are the first and second fundamental forms respectively.

A degenerate critical point of the distance function satisfies $\det(\nabla^2 d) = 0$ if and only if $\det(\nabla^2 u) = 1/a^2 = \kappa_1\kappa_2$, where κ_1 and κ_2 are the principal curvatures. A point $\mathbf{p} \in \mathbb{M}$ is therefore a degenerate critical point of the distance function $d_{\mathbf{v}}$ if and only if \mathbf{v} is a focal point of (\mathbb{M}, \mathbf{p}) . In addition, the Morse index of a nondegenerate critical point of the distance function $d_{\mathbf{v}}$

is equal to the number of focal points of (M, \mathbf{p}) which lie on the segment from \mathbf{p} to \mathbf{v} . This can be shown using the Hessian matrix $\nabla^2 d$ since the number of its negative eigenvalues is equal to the number of eigenvalues of the \mathbf{H} (assuming that \mathbf{I} is the identity matrix) which are $\geq 1/a$.

Without loss of generality we choose \mathbf{v} to be the centroid \mathbf{c} of the surface M , and for simplicity we consider the centroid to be the origin of the Euclidean coordinate system as pictured in Figure 7.10. Hence the distance function becomes

$$d(\mathbf{p}) = \|\mathbf{p}\|^2 = x^2 + y^2 + z^2,$$

where $\mathbf{p} = (x, y, z)$. Note that for $r > 0$, the level sets $\{\mathbf{p} \in M : d(\mathbf{p}) = r^2\}$ of the distance function are concentric spheres of radii r , and the object can be reconstructed if we know its intersections with these concentric spheres (see Figure 7.10).

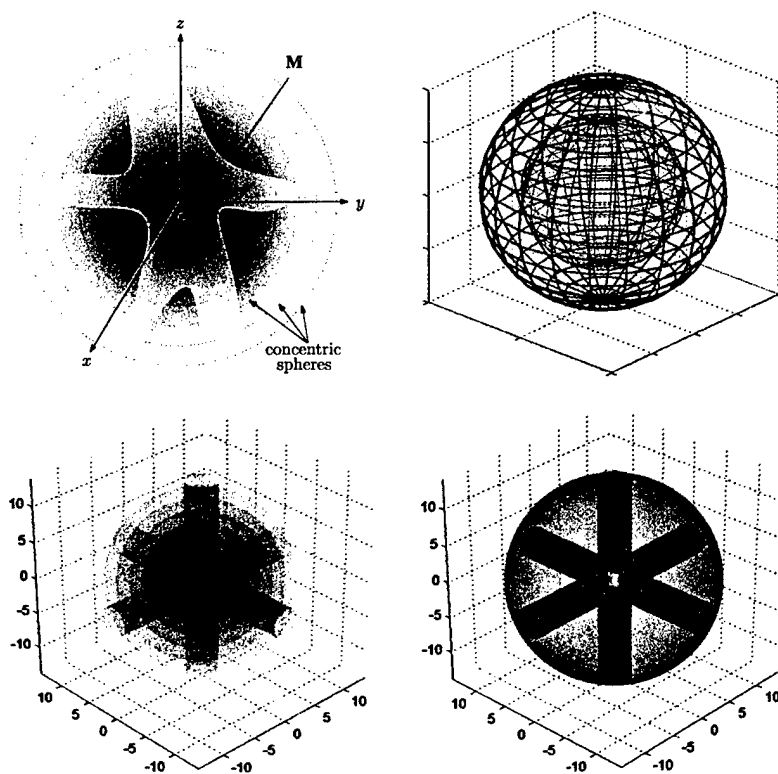


Figure 7.10: Illustration of the distance function.

7.6 Connection between height function and distance function

For certain purposes such as terrain image reconstruction, the height function has nicer properties, while for others the distance function behaves better due mainly to its rotational invariance. There is, however, one situation when these two functions are essentially the same. Suppose that a surface M is embedded in a sphere S^2 centered at the origin and with radius R (see Figure 7.11), then the height function h_v and the distance function d_v differ by a constant and therefore have the same critical points:

$$d_v(p) = \|p - v\|^2 = \|v\|^2 + \|p\|^2 - 2p \cdot v = \underbrace{(\|v\|^2 + R^2)}_{\text{constant}} - 2h_v(p).$$

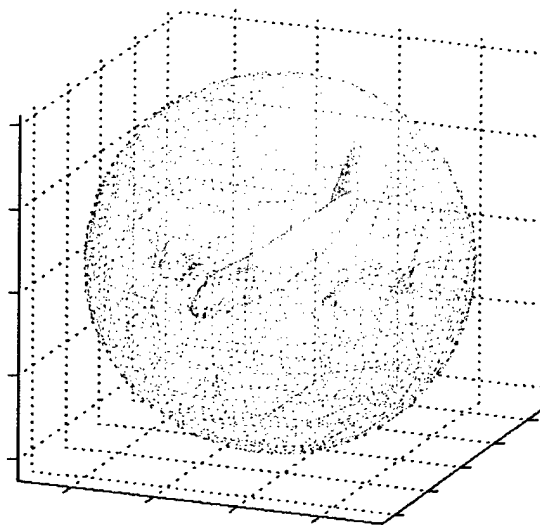


Figure 7.11: Embedding of a 3D airplane into a sphere.

The key idea behind using the distance function is to track the changes in topology as we cross a surface singularity. In the first step, we start with a sphere having a sufficiently small radius, and centered as the barycenter of the underlying surface, then we evolve this sphere by increasing its radius so that we will have a set of concentric spheres covering the entire surface. As we cross a surface singularity, a topological change of the level curves will take place as illustrated

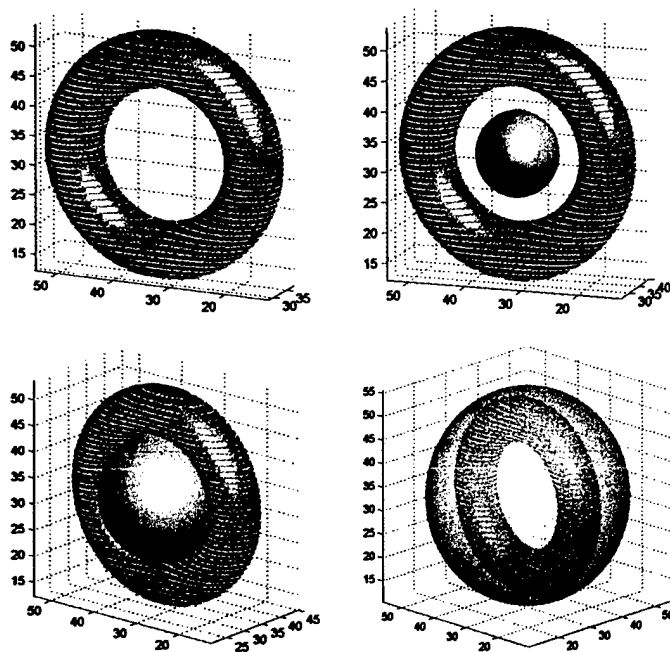


Figure 7.12: Distance function defined on a torus.

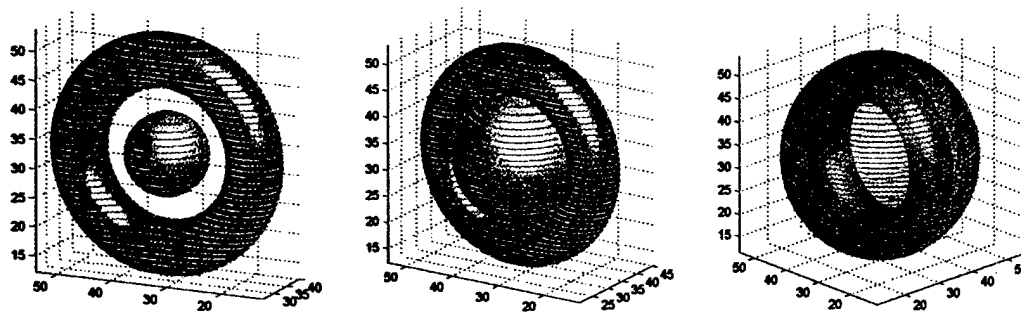


Figure 7.13: Distance function defined on a torus (cont.).

in Figures 7.12, 7.13, and 7.14. The level curves for two 3D real data objects are pictured in Figure 7.15. In other words, some level curves may split or merge. We are essentially interested in these changes for topological modelling purposes which in turn may be explained by applying Morse theory to the distance function.

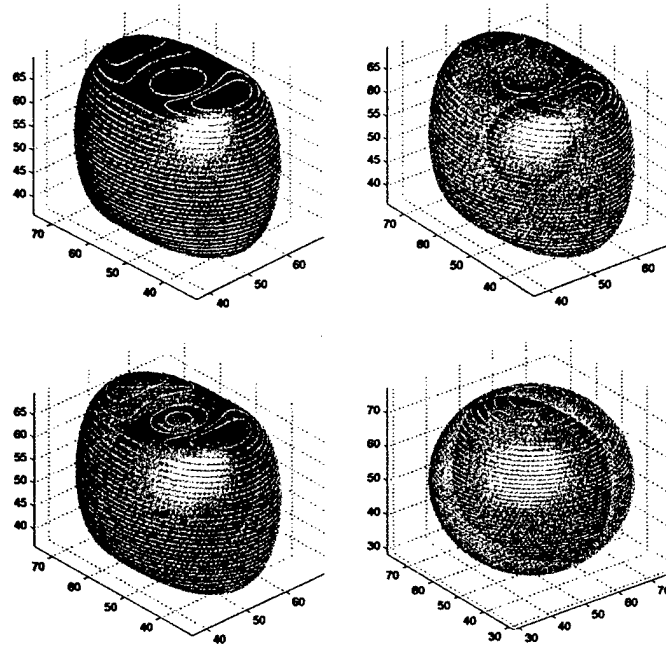


Figure 7.14: Distance function defined on a dimple.

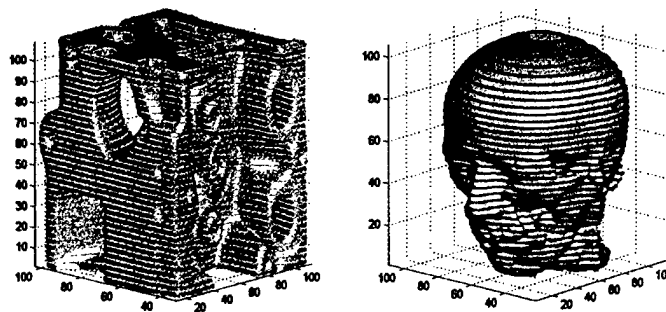


Figure 7.15: Isocontours of 3D real data.

Conclusions and Future Research

This thesis has presented computational algorithms for variational image denoising, topological modeling, three-dimensional object recognition, and geometric matching. We have demonstrated the use of these algorithms through a variety of imaging and computer vision applications including image filtering, singularity extraction and evolution, topological modeling of illuminated surfaces, geodesic matching of triangle meshes, and distance function-based object recognition. The geometric/topological algorithms are tailored for the discrete representation of surfaces as triangle meshes. We have demonstrated the effectiveness of the proposed methods through numerical simulations with synthetic and real data in 2D and 3D computer imagery.

In the next Section, the contributions made in each of the previous chapters and the concluding results drawn from the associated research work are presented. Suggestions for future research directions related to this thesis are provided in Section 8.2.

8.1 Contributions of the thesis

8.1.1 Robust and efficient variational filters for image denoising

Using the theoretical fundamentals of robust statistics, a variational filter referred to as a Huber gradient descent flow was proposed in Chapter 3. It is a result of optimizing a Huber functional subject to some noise constraints, and it takes a hybrid form of a total variation diffusion for large gradient magnitudes and of a linear diffusion for small gradient magnitudes. Using the gained insight, and as a further extension, we proposed an information-theoretic gradient descent flow

which is a result of minimizing a functional that is a hybrid between a negentropy variational integral and a total variation. Illustrating experimental results demonstrated a much improved performance of the approach in the presence of Gaussian and heavy-tailed (impulsive) noise.

8.1.2 A topological variational model for image singularities

Image singularities are prominent landmarks and their detection, recognition, and classification is a crucial step in image processing and computer vision. Such singularities carry important information for further operations, such as image registration, shape analysis, motion estimation, and object recognition. In Chapter 4, we proposed a topological gradient descent flow for image singularities. The approach is expressed in the higher order variational framework as a minimizer of a variational integral involving the gradient and the Hessian matrix of the height function defined on a manifold. We demonstrated through numerical simulations the power of the proposed technique in preserving image singularities.

8.1.3 Topological modeling of illuminated surfaces using Reeb graph

In Chapter 5 we introduced a reliable and efficient feature based object representation for topological modeling of three-dimensional illuminated surfaces. The proposed approach encodes an object into the Reeb graph concept from computational topology. This skeletal structure is based on a generalized height function in the light direction defined on an illuminated surface. The topological properties of the proposed representation were analyzed in the Morse theoretic framework, and its close relationship to the shading problem was also highlighted. Some numerical simulations with synthetic and real 3D data were provided to demonstrate the potential of object singularities in topological modeling.

8.1.4 Geodesic object representation and recognition

In Chapter 6 we proposed a shape signature that captures the intrinsic geometric structure of 3D objects. The primary motivation of the proposed approach is to encode a 3D shape into a

one-dimensional geodesic distribution function. This compact and computationally simple representation is based on a global geodesic distance defined on an object surface, and takes the form of a kernel density estimate. To gain further insight into the geodesic shape distribution and its practicality in 3D computer imagery, some numerical experiments were provided to demonstrate the potential and the much improved performance of the proposed methodology in 3D object matching. This was carried out using an information-theoretic measure of dissimilarity between probabilistic shape distributions.

8.1.5 Distance function-based object recognition

In Chapter 7 we introduced a topological approach to object recognition using a distance function. Similarly to the height function strategy which consists of reconstructing surface from its cross-sections, the key idea behind using a distance function is that a surface may be reconstructed from its intersections with concentric spheres centered at the centroid of the underlying surface. The topological changes in the surface occur as we increase the value of the sphere radius. At singular points, the level curves of the distance function may split or merge which indicate topological changes. We also show that when a surface is embedded in a sphere, the height function and the distance function are equivalent in a Morse-theoretic setting, that is both functions have the same singularities.

8.2 Future research directions

Several interesting research directions motivated by this thesis are discussed next. In addition to designing new methodologies for image denoising and segmentation, we intend to accomplish the following projects in the near future:

8.2.1 Attributed Reeb graph matching, indexing, and retrieval

Recently we have been working on the representation, matching, indexing and retrieval in a database of 3D objects based on the topological and geometric information. Building a database requires

collecting 3D models, computing their Reeb graph representations, and indexing in the data base based on an abstracted information given by their Reeb graphs. An appropriate and efficient representation of the Reeb graph is the attributed Reeb graph that represents topology and geometry in a compact representation, where vertices and edges have geometric attributes. In other words, we associate to the graph as much geometric information as possible that will be attached to the graph for further tasks such as matching, indexing and retrieval.

8.2.2 Entropic minimum spanning Reeb trees for terrain image analysis

The vertices of a Reeb tree can be characterized using the minimum spanning tree (MST) which aims to quantify spacial dot patterns by revealing hidden nearest-neighbor correlations. The MST representation is naturally translation and rotation invariant, and therefore constitutes a good candidate for geo-registration and other image registration applications. The Jensen-Rényi divergence may be used as a robust dissimilarity measure between the Morse features of the target and the reference images.

8.2.3 Divergence measures and information geometry

There are many possibilities for extending the Jensen-Rényi divergence using more generalized entropy measures, and borrowing concepts from information geometry in order to fully employ the mathematical machinery of differential geometry and topology. Information geometry is the branch of probability theory dedicated to provide families of probability distributions with differential geometrical structures. One then uses the tools of differential geometry in order to have a clear and intuitive picture of a family of probability distributions which form a differentiable manifold. Information geometry elucidates the geometric structure of such a manifold.

Theoretically we hope to develop more rigorous analysis for the Jensen-Rényi divergence. It is also worthwhile to combine other computational techniques with our approach. Furthermore, we are planning to apply this divergence measure to other imaging applications including DNA segmentation, microarray images and independent component analysis.

List of References

- [1] L. Alvarez, P.L. Lions, and J.M. Morel, "Image selective smoothing and edge detection by nonlinear diffusion (II), " *SIAM J. Numerical Analysis*, vol. 29, pp. 845-866, 1992.
- [2] L. Alvarez, and L. Mazorra, "Signal and image restoration using shock filters and anisotropic diffusion, " *SIAM J. Numerical Analysis*, vol. 31, pp. 590-605, 1994.
- [3] V.I. Arnold , *The Theory of Singularities and Its Applications*, Accademia Nazionale dei Lincei, Italy 1991.
- [4] G. Aubert and L. Vese, "A variational method in image recovery," *SIAM J. Numerical Analysis*, vol. 34, no. 5, pp. 1948-1979, 1997.
- [5] P.N. Belhumeur, D.J. Kriegman, and A.L. Yuille, "The bas-relief ambiguity," *International Journal of Computer Vision*, 35(1), pp. 33-44, 1999.
- [6] A. Ben Hamza and H. Krim, "A Variational approach to maximum a posteriori estimation for image denoising," *Lecture Notes in Computer Science*, vol. 2134, pp. 19-34, September 2001.
- [7] A. Ben Hamza and H. Krim, "Towards a unified view of estimation: variational vs. statistical," *Proc. IEEE International Conference on Image Processing*, October 2001.
- [8] A. Ben Hamza, H. Krim, and G.B. Unal, "Unifying probabilistic and variational estimation," *IEEE Signal Processing Magazine*, vol. 19, no. 5, pp. 37-47, September 2002.
- [9] A. Ben Hamza, H. Krim, and J. Zerubia, "A nonlinear entropic variational model for image filtering," *EURASIP Journal on Applied Signal Processing*, under review 2003.

- [10] A. Ben Hamza and H. Krim, "Geodesic object representation and recognition," *Lecture Notes in Computer Science*, 2003.
- [11] A. Ben Hamza and H. Krim, "A topological skeleton of illuminated manifolds," *Proc. IEEE International Conference on Image Processing*, September 2003.
- [12] Y. He, A. Ben Hamza, and H. Krim, "A generalized divergence measure for robust image registration," *IEEE Trans. Signal Processing*, vol. 51, no. 5, pp. 1211-1220, May 2003.
- [13] A. Ben Hamza and H. Krim, "Jensen-Renyi divergence measure: theoretical and computational perspectives," *Proc. IEEE International Symposium on Information Theory*, Japan, 2003.
- [14] A. Ben Hamza and H. Krim, "Image registration and segmentation by maximizing Jensen-Renyi divergence," *Lecture Notes in Computer Science*, vol. 2683, pp. 147-163, 2003.
- [15] A. Ben Hamza and H. Krim, "Robust environmental image denoising," *ISI International Conference on Environmental Statistics and Health*, 2003.
- [16] A. Ben Hamza and H. Krim, "A topological variational model for image singularities," *Proc. IEEE International Conference on Image Processing*, September 2002.
- [17] A. Ben Hamza and H. Krim, "Image denoising: a nonlinear robust statistical approach," *IEEE Trans. Signal Processing*, vol. 49, no. 12, pp. 3045-3054, December 2001.
- [18] A. Ben Hamza and H. Krim, "Robust influence functionals for image filtering," *Proc. IEEE International Conference on Image Processing*, September 2003.
- [19] S. Amari, *Differential-Geometrical Methods of Statistics*, Lecture Notes in Statistics. Berlin, Germany: Springer, vol. 25, 1985.
- [20] M.J. Black, G. Sapiro, D.H. Marimont, and D. Heeger, "Robust anisotropic diffusion," *IEEE Trans. Image Processing*, vol. 7, no. 3, pp. 421-432, March 1998.
- [21] J.W. Bruce and P.J. Giblin, *Curves and singularities*, Cambridge University Press, second edition, 1992.

- [22] D.P.L. Castriano and S.A. Hayes, *Catastrophe theory*, Addison-Wesley Publishing Company, 1993.
- [23] T.F. Chan and C.K. Wong, "Total variation blind deconvolution", *IEEE Trans. Image Processing*, vol. 7, no. 3, pp. 370-375, March 1998.
- [24] T.F. Chan and P. Mulet, "On the convergence of the lagged diffusivity fixed point method in image restoration," *SIAM J. Numerical Analysis*, vol. 36, no. 2, pp. 354-367, 1999.
- [25] T.F. Chan, S. Osher, and J. Shen, "The digital TV filter and nonlinear denoising," *IEEE Trans. Image Processing*, vol. 10, no. 2, pp. 231-241, 2001.
- [26] P. Charbonnier, L. Blanc-Féraud, G. Aubert, and M. Barlaud, "Deterministic edge-preserving regularization in computed imaging," *IEEE Trans. Image Processing*, vol. 6, no. 2, pp. 298-311, February 1997.
- [27] M. Cetin, and W.C. Karl, "Feature-enhanced synthetic aperture radar image formation based on nonquadratic regularization," *IEEE Trans. Image Processing*, vol 10, no. 4, pp. 623-631, April 2001.
- [28] T.F. Cox and M.A. Cox, *Multidimensional scaling*, second edition, Monographs on Statistics and Applied Probability, vol. 88, 2001.
- [29] M. do Carmo, *Differential geometry of curves and surfaces*, Prentice-Hall, New Jersey, 1976.
- [30] R. Deriche and O. Faugeras, "Les EDP en traitement des images et vision par ordinateur," *Traitement du Signal*, vol. 13, no. 6, 1996.
- [31] A.T. Fomenko and T.L. Kunii, *Topological modeling for visualization*, Springer-Verlag Tokyo, 1997.
- [32] G. Gallager, *Information theory and reliable communications*, John Wiley Sons, 1968.
- [33] S. Geman and D. Geman, "Stochastic relaxation, Gibbs distributions and the Bayesian restoration of images," *IEEE Trans. Pattern Analysis and Machine intelligence*, vol. 6, no. 7, pp. 721-741, July 1984.

- [34] M. Ghomi, "Shadows and convexity of surfaces," *Annals of Mathematics*, vol. 155, pp. 281-293, 2002.
- [35] M. Ghomi, "Solution to the shadow problem in 3-space," *Minimal Surfaces, Geometric Analysis and Symplectic Geometry*, Adv. Studies in Pure Math., 2000
- [36] M. Giaquinta and S. Hildebrandt, *Calculus of variations I: the Lagrangian formalism*, Springer-Verlag, 1996.
- [37] J.F. Gomez, J. Martinez, A.M. Robles, and R. Roman, "An analysis of edge detection by using the Jensen-Shannon divergence," *J. Mathematical Imaging and Vision*, vol. 13, no. 1, pp. 35-56, August 2000.
- [38] V. Guillemin and A. Pollack, *Differential topology*, Prentice-Hall, Inc., Englewood Cliffs, NJ 1974.
- [39] A.O. Hero, B. Ma, O. Michel and J. Gorman, "Applications of entropic spanning graphs," *IEEE Signal Processing Magazine*, vol. 19, pp. 85-95, September 2002.
- [40] M. Hilaga, Y. Shinagawa, T. Komura, and T.L. Kunii, "Topology matching for fully automatic similarity estimation of 3D shapes," *Proc. SIGGRAPH*, pp. 203-212, August 2001.
- [41] B.K.P. Horn and M.J. Brooks, *Shape from shading*, MIT Press, 1989.
- [42] P. Huber, *Robust statistics*. John Wiley & Sons, New York, 1981.
- [43] K. Ito and K. Kunisch, "Restoration of edge-flat-grey scale images," *Inverse Problems*, vol. 16, no.4, pp. 909-928, August 2000.
- [44] H.T. Jongen, P. Jonker, and F. Twilt, *Nonlinear optimization in finite dimensions*, kluwer Academic Publishers, 2000.
- [45] R. Kimmel and J.A. Sethian, "Computing geodesic paths on manifolds," *Proc. Natl. Acad. sci.*, vol. 95, pp. 8431-8435, July 1998.
- [46] L.C. Kinsey, *Topology of surfaces*, Springer-Verlag, 1993.

- [47] P. Kornprobst, R. Deriche, and G. Aubert, "Image sequence analysis via partial differential equations," *J. Mathematical Imaging and Vision*, vol. 11, no. 1, pp. 5-26, September 1999.
- [48] H. Krim, "On the distributions of optimized multiscale representations," *ICASSP-97*, vol. 5, pp. 3673-3676, 1997.
- [49] H. Krim and I.C. Schick, "Minimax description length for signal denoising and optimized representation," *IEEE Trans. Information Theory*, vol. 45, no. 3, pp. 898-908, April 1999.
- [50] S. Kullback and R. Liebler, "On information and sufficiency," *Ann. Math. Statist.*, vol. 22, pp. 79-86, 1951.
- [51] J. Lin, "Divergence measures based on the Shannon entropy," *IEEE Trans. Information Theory*, vol. 37, no. 1, pp. 145-151, 1991.
- [52] C. Lu, Y. Cao, and D. Mumford, "Surface evolution under curvature flows," *Journal of Visual Communication and Image Representation*, vol. 13, no. 1/2, pp. 65-81, 2002.
- [53] J.J. Koenderink, *Solid Shape*, MIT Press, Cambridge, Massachusetts, 1990.
- [54] J. MacQueen, "Some methods for classification and analysis of multivariate observations," *Proc. 5th Berkeley Symp. Math. Stat. and Prob.*, pp. 281-297, 1967.
- [55] J. Milnor, *Morse theory*, Princeton University Press, Princeton, NJ 1963.
- [56] J. Morel and S. Solemini, *Variational Methods in Image Segmentation*, Birkhauser, 1995.
- [57] D. Mumford and J. Shah, "Optimal approximations by piecewise smooth functions and associated variational problems," *Commun. Pure Appl. Math.*, vol. 42, pp. 577-684, 1989.
- [58] M.K. Murray and J.W. Rice, *Differential geometry and statistics*, Monographs on Statistics and Applied Probability, vol. 48, 1993.
- [59] R. Osada, T. Funkhouser, B. Chazelle, and D. Dobkin, "Shape distributions," *ACM Transactions on Graphics*, vol. 21, no. 4, pp. 807-832, October 2002.

- [60] R.S. Palais and C. Terng, *Critical point theory and submanifold geometry*, Lecture Notes in Mathematics, vol. 1353, 1988.
- [61] P. Perona and J. Malik, "Scale space and edge detection using anisotropic diffusion," *IEEE Trans. Pattern Analysis and Machine intelligence*, vol. 12, no. 7, pp. 629-639, July 1990.
- [62] I. Pollak, A.S. Willsky, and H. Krim, "Image segmentation and edge enhancement with stabilized inverse diffusion equations," *IEEE Trans. Image Processing*, vol. 9, no. 2, pp. 256-266, February 2000.
- [63] C. R. Rao, "Information and accuracy attainable in the estimation of statistical parameters," *Bull. Calcutta. Math. Soc.*, vol. 37, pp. 8191, 1945.
- [64] R. Roman, P. Bernaola, and J.L. Oliver, "Sequence compositional complexity of DNA through an entropic segmentation method," *Physical Review Letters*, vol. 80, no. 6, pp. 1344-1347, February 1998.
- [65] L. Rudin, S. Osher, and E. Fatemi, "Nonlinear total variation based noise removal algorithms," *Physica D*, vol. 60, pp. 259-268, 1992.
- [66] C. Samson, L. Blanc-Feraud, G. Aubert, and J. Zerubia, "A variational model for image classification and restoration," *IEEE Trans. Pattern Analysis and Machine intelligence*, vol. 22, no. 5, pp. 460-472, May 2000.
- [67] Y. Shinagawa, T.L. Kunii, and Y.L. Kergosien, "Surface coding based on Morse theory," *IEEE Comp. Graph. and Appl.*, vol. 11 no. 5 , pp. 66-78, 1991.
- [68] Y. Shinagawa and T.L. Kunii, "Constructing a Reeb graph automatically from cross sections," *IEEE Comp. Graph. and Appl.*, vol. 11 no. 6 , pp. 44-51, 1991.
- [69] R. Stoica, J. Zerubia, and J.M. Francos, "Image retrieval and indexing: A hierarchical approach in computing the distance between textured images," *IEEE Int. Conf. on Image Processing*, Chicago, 1998.

- [70] S. Takahashia, T. Ikeda, Y. Shinagawa, T.L. Kunii, and M. Ueda, "Algorithms for extracting correct critical points and constructing topological graphs from discrete geographical elevation data," *Eurographics*, vol. 14, no. 3, 1995.
- [71] J.B. Tenenbaum, V. de Silva, and J.C. Langford, "A global geometric framework for nonlinear dimensionality reduction," *Science*, vol. 290, pp. 2319-2323, December 2000.
- [72] A.H. Wallace, *Differential topology: first steps*, W.A. Benjamin, Inc., 1968.
- [73] M.P. Wand and M.C. Jones, *Kernel Smoothing*, Chapman and Hall, London, 1995.
- [74] J. Weickert, *Anisotropic diffusion in image processing*, Stuttgart, Germany: Teubner-Verlab, 1998.
- [75] R.E. White, *Computational Mathematics: Models, Methods and Analysis with MATLAB and MPI*, Chapman and Hall/CRC, 2003.
- [76] A. Yezzi, "Modified curvature motion for image smoothing and enhancement," *IEEE Trans. Image Processing*, vol. 7, no. 3, pp. 345-352, 1998.
- [77] Y.L. You, W. Xu, A. Tannenbaum, and M. Kaveh, "Behavioral Analysis of anisotropic diffusion in image processing," *IEEE Trans. Image Processing*, vol. 5, no. 11, pp. 1539-1553, 1996.

Appendix A

The first variation of the functional $\mathcal{F}(u) = \int_{\Omega} F(|\nabla u|) dx$ in the direction of v is given by

$$\delta\mathcal{F}(u; v) = \left. \frac{d}{d\epsilon} \mathcal{F}(u + \epsilon v) \right|_{\epsilon=0} = \int_{\Omega} \left(\frac{F'(|\nabla u|)}{|\nabla u|} \nabla u \cdot \nabla v \right) dx.$$

The following identity

$$\operatorname{div}(v \nabla u) = \operatorname{div}(\nabla u) v + \nabla u \cdot \nabla v,$$

yields

$$\int_{\Omega} \frac{F'(|\nabla u|)}{|\nabla u|} \nabla u \cdot \nabla v dx = - \int_{\Omega} \operatorname{div} \left(\frac{F'(|\nabla u|)}{|\nabla u|} \nabla u \right) v dx + \int_{\Omega} \operatorname{div} \left(v \frac{F'(|\nabla u|)}{|\nabla u|} \nabla u \right) dx$$

Using the divergence theorem for a vector field \mathbf{w}

$$\int_{\Omega} \operatorname{div}(\mathbf{w}) dx = \int_{\partial\Omega} \mathbf{w} \cdot \boldsymbol{\nu} ds$$

where $\boldsymbol{\nu}$ is the outward unit normal vector (field) on $\partial\Omega$ (the boundary of Ω) and ds is an area element. Therefore

$$\int_{\Omega} \operatorname{div} \left(v \frac{F'(|\nabla u|)}{|\nabla u|} \nabla u \right) dx = \int_{\partial\Omega} v \frac{F'(|\nabla u|)}{|\nabla u|} \nabla u \cdot \boldsymbol{\nu} ds.$$

If we assume homogenous Neumann boundary conditions

$$\nabla u \cdot \boldsymbol{\nu} = u_{\boldsymbol{\nu}} = \frac{\partial u}{\partial \boldsymbol{\nu}} = 0,$$

then the first variation of \mathcal{F} is reduced to

$$\delta\mathcal{F}(u; v) = - \int_{\Omega} \operatorname{div} \left(\frac{F'(|\nabla u|)}{|\nabla u|} \nabla u \right) v dx, \quad \forall v \in X$$

which concludes the proof.

APPENDIX B

Appendix B

A numerical implementation of the partial differential equation given by Eq. 13 is performed using an explicit scheme in time and location as follows. Let $u_{i,j}^n$ be the approximation of $u(x, y, t)$ on a grid $(i\Delta x, j\Delta y, n\Delta t)$. For simplicity we assume that $\Delta x = \Delta y = h$. Denote by

$$D_{\pm}^x u = \pm \frac{u_{i\pm 1,j}^n - u_{i,j}^n}{h} \quad \text{and} \quad D_{\pm}^y u = \pm \frac{u_{i,j\pm 1}^n - u_{i,j}^n}{h}$$

the matrices of column differences and row differences respectively (i.e. backward and forward differences).

Similarly, the central differences are given by

$$D_c^x u = \frac{u_{i+1,j}^n - u_{i-1,j}^n}{2h} \quad \text{and} \quad D_c^y u = \frac{u_{i,j+1}^n - u_{i,j-1}^n}{2h}.$$

The operator $\text{div}(g(|\nabla u|)\nabla u)$ on the right hand side of Eq. 13 is discretized using an upwind scheme as follows

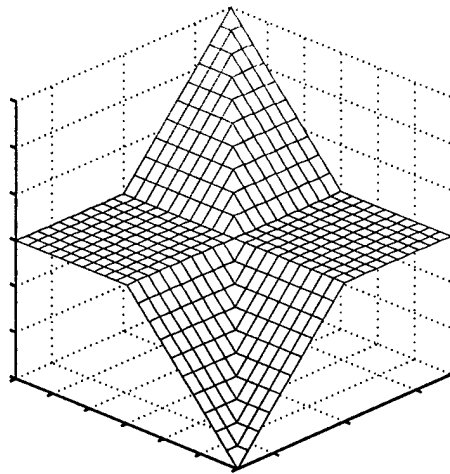
$$\begin{aligned} \text{div}(g(|\nabla u|)\nabla u) &= \frac{1}{h} \left\{ D_-^x \left(g \left[\left(\left(\frac{D_+^x u}{h} \right)^2 + \left(\min\text{mod} \left(\frac{D_+^y u}{h}, \frac{D_-^y u}{h} \right) \right)^2 \right]^{1/2} \right) \left(\frac{D_+^x u}{h} \right) \right) \right\} \\ &\quad + \frac{1}{h} \left\{ D_-^y \left(g \left[\left(\left(\frac{D_+^y u}{h} \right)^2 + \left(\min\text{mod} \left(\frac{D_+^x u}{h}, \frac{D_-^x u}{h} \right) \right)^2 \right]^{1/2} \right) \left(\frac{D_+^y u}{h} \right) \right) \right\}, \end{aligned}$$

where $\min\text{mod}$ is a function that returns the argument with smallest absolute value when all the arguments are of the same sign and zero otherwise. The $\min\text{mod}$ function is a limiter whose goal is to prevent oscillations while maintaining the order of accuracy of the method, and it is defined

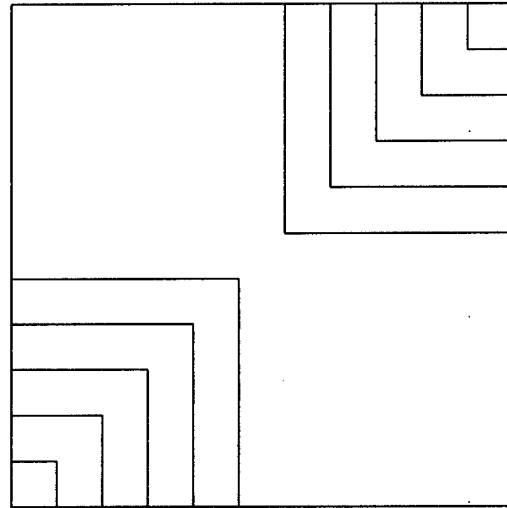
as

$$\begin{aligned}
 \text{minmod}(a, b) &= \left(\frac{\text{sign}(a) + \text{sign}(b)}{2} \right) \min(|a|, |b|) \\
 &= \min(\max(a, 0), \max(b, 0)) + \max(\min(a, 0), \min(b, 0)) \\
 &= \begin{cases} 0 & \text{if } ab \leq 0 \\ a & \text{if } |a| \leq |b| \text{ and } ab > 0 \\ b & \text{if } |a| > |b| \text{ and } ab > 0. \end{cases}
 \end{aligned}$$

Figure (a) below depicts the gradient vector field of the minmod function (the background color indicates the value of the minmod function), and Figure (b) illustrates its contours.



(a) 3D plot of the minmod function



(b) level curves

Appendix C

Surface Curvatures

Let $\mathbf{p} \in \mathbb{M}$. Let $\mathbf{v} \in T_{\mathbf{p}}\mathbb{M} = \text{span}\{\mathbf{r}_x, \mathbf{r}_y\}$ (we assume \mathbf{v} a unit vector). By definition $\mathbf{v} \in T_{\mathbf{p}}\mathbb{M}$ if there exists a curve $c : (-\epsilon, \epsilon) \rightarrow \mathbb{M}$ for some $\epsilon > 0$ such that $c(0) = \mathbf{p}$ and $c'(0) = \mathbf{v}$. In other words, the tangent space is the set of vectors orthogonal to the surface normal. Thus, the tangent plane at \mathbf{p}_0 is the set of points \mathbf{p} such that $\mathbf{N}(\mathbf{p}) \cdot (\mathbf{p} - \mathbf{p}_0) = 0$. Hence for the Monge patch, the equation of the tangent plane at a point $(x_0, y_0, u(x_0, y_0))$ is given by $z = u(x_0, y_0) + \nabla u(x_0, y_0) \cdot (x - x_0, y - y_0)$.

Let $f : \mathbb{M} \rightarrow \mathbb{R}$ be a smooth function. The directional derivative of f at \mathbf{p} in the direction of \mathbf{v} is given by $\nabla_{\mathbf{v}} f = (f \circ c)'(0)$, where $c : (-\epsilon, \epsilon) \rightarrow \mathbb{M}$ for some $\epsilon > 0$ is a curve such that $c(0) = \mathbf{p}$ and $c'(0) = \mathbf{v}$.

If $f : \mathbb{M} \rightarrow \mathbb{R}^3$, then the differential of f at \mathbf{p} is the map $df : T_{\mathbf{p}}\mathbb{M} \rightarrow \mathbb{R}^3$ such that $df(\mathbf{v}) = \nabla_{\mathbf{v}} f$ for all $\mathbf{v} \in T_{\mathbf{p}}\mathbb{M}$.

If $f : \mathbb{M} \rightarrow \tilde{\mathbb{M}}$ is a smooth function between two manifolds, then the differential of f at \mathbf{p} is the linear map $df : T_{\mathbf{p}}\mathbb{M} \rightarrow T_{f(\mathbf{p})}\tilde{\mathbb{M}}$. In particular, let $\mathbf{v} \in T_{\mathbf{p}}\mathbb{M}$. Then $\nabla_{\mathbf{v}} \mathbf{N} \in T_{\mathbf{p}}\mathbb{M}$. Indeed, since $\langle \mathbf{N}, \mathbf{N} \rangle = 1$, it follows that $0 = \nabla_{\mathbf{v}} \langle \mathbf{N}, \mathbf{N} \rangle = 2 \langle \nabla_{\mathbf{v}} \mathbf{N}, \mathbf{N} \rangle$. Thus, $\nabla_{\mathbf{v}} \mathbf{N}$ is orthogonal to \mathbf{N} .

The first fundamental form $I : T_{\mathbf{p}}\mathbb{M} \times T_{\mathbf{p}}\mathbb{M} \rightarrow \mathbb{R}$ is a bilinear form such that $I(\mathbf{v}, \mathbf{w}) = \langle \mathbf{v}, \mathbf{w} \rangle$, and its matrix with respect to the orthogonal basis $\{\mathbf{r}_x, \mathbf{r}_y\} \in T_{\mathbf{p}}\mathbb{M}$ is given by

$$I = \begin{pmatrix} I(\mathbf{r}_x, \mathbf{r}_x) & I(\mathbf{r}_x, \mathbf{r}_y) \\ I(\mathbf{r}_y, \mathbf{r}_x) & I(\mathbf{r}_y, \mathbf{r}_y) \end{pmatrix} = \begin{pmatrix} \mathbf{r}_x \cdot \mathbf{r}_x & \mathbf{r}_x \cdot \mathbf{r}_y \\ \mathbf{r}_y \cdot \mathbf{r}_x & \mathbf{r}_y \cdot \mathbf{r}_y \end{pmatrix}.$$

The matrix I is also called the metric or metric tensor, and it is the analogous of the speed in the case of space curves. This matrix determines all the intrinsic properties of the surface. These properties depend on the surface and do not depend on its embedding in space. Furthermore, the matrix I is invariant to rotation of the surface in space because it is defined in terms of inner products that are rotation invariant.

The Weingarten map (also called the shape operator) is a linear map $W : T_p\mathbb{M} \rightarrow T_p\mathbb{M}$ such that $W(v) = -\nabla_v N$. In terms of the basis $\{r_x, r_y\} \in T_p\mathbb{M}$, we have $W(r_x) = -N_x$ and $W(r_y) = -N_y$. These equations are called Weingarten equations and they express the derivatives of the normal to a surface using derivatives of the position vector.

The second fundamental form $II : T_p\mathbb{M} \times T_p\mathbb{M} \rightarrow \mathbb{R}$ is a bilinear form such that $II(v, w) = W(v) \cdot w = -\langle \nabla_v N, w \rangle$, and its matrix with respect to the orthogonal basis $\{r_x, r_y\} \in T_p\mathbb{M}$ is given by

$$II = \begin{pmatrix} II(r_x, r_x) & II(r_x, r_y) \\ II(r_y, r_x) & II(r_y, r_y) \end{pmatrix} = \begin{pmatrix} -N_x \cdot r_x & -N_x \cdot r_y \\ -N_y \cdot r_x & -N_y \cdot r_y \end{pmatrix}$$

The matrix II is also invariant under rotation of the surface.

The third fundamental form $III : T_p\mathbb{M} \times T_p\mathbb{M} \rightarrow \mathbb{R}$ is a bilinear form such that $III(v, w) = W(v) \cdot W(w) = \langle \nabla_v N, \nabla_w N \rangle$, and its matrix with respect to the orthogonal basis $\{r_x, r_y\} \in T_p\mathbb{M}$ is given by

$$III = \begin{pmatrix} III(r_x, r_x) & III(r_x, r_y) \\ III(r_y, r_x) & III(r_y, r_y) \end{pmatrix}$$

The third fundamental form is given in terms of the first and second forms by $III - 2HII + KI = 0$, where H and K are the mean and Gaussian curvatures respectively.

The Gaussian curvature is given by the determinant of W . The normal curvature of \mathbb{M} in the direction $v \in T_p\mathbb{M}$ is $\kappa(v) = W(v) \cdot v$. Since $v \in T_p\mathbb{M} = \text{span}\{r_x, r_y\}$, it follows that $v = ar_x + br_y$. Therefore the normal curvature in the direction v can be expressed as

$$\kappa(v) = W(v) \cdot v = \frac{\ell a^2 + 2mab + nb^2}{ea^2 + 2fab + gb^2},$$

where e, f and g are the coefficients of the first fundamental form, and ℓ, m and n are the coefficients of the second fundamental form. The maximum and minimum values of the normal curvature at a

point on a regular surface are called the principal curvatures κ_1 and κ_2 .

Rodrigues curvature formula is given by $d\mathbf{N} + \kappa_i d\mathbf{r} = 0$, where κ_i are the principal curvatures.

The harmonic curvature of the principal curvatures is defined as

$$R = \frac{1}{2} \left(\frac{1}{\kappa_1} + \frac{1}{\kappa_2} \right).$$

The extended Gaussian image is the reciprocal of the Gaussian curvature, that is

$$G(\mathbf{p}) = \frac{1}{\kappa_1 \kappa_2}.$$

Implicit surface curvatures

Let $U : \Omega \subset \mathbb{R}^3 \rightarrow \mathbb{R}$ be a smooth function. An implicit surface is defined as a level set of the function U , i.e. $U(x, y, z) = 0$ (for instance). The principal curvatures and the principal directions of the level surface satisfy the following equation

$$-\left(I_3 - (\nabla U)(\nabla U)^T\right) \frac{\nabla^2 U}{\|\nabla U\|} \mathbf{e} = \kappa \mathbf{e},$$

where I_3 is a 3×3 identity matrix.

Offset surface

Let $\mathbb{M} \subset \mathbb{R}^3$ be a regular surface. The surface parallel to \mathbb{M} at a distance $t > 0$ is the set $\tilde{\mathbb{M}} = \{\mathbf{q} : d(\mathbf{q}, \mathbb{M}) = t\}$

The offset surface patch $\tilde{\mathbf{r}}$ at distance t to a surface \mathbb{M} parametrized by \mathbf{r} is defined as

$$\tilde{\mathbf{r}}(x, y) = \mathbf{r}(x, y) + t \mathbf{N}(x, y), \quad (1)$$

where t is the distance of the parallel surface from the original one, and \mathbf{N} is the unit surface normal of \mathbf{r} .